On the properties of discs around accreting brown dwarfs

Nathan J. Mayne⋆ and Tim J. Harries
School of Physics, University of Exeter, Stocker Road, Exeter, EX4 4QL.

ABSTRACT
To Do

(i)Read new papers and put in any relevant stuff.
(ii)Sort structure paragraph at end of intro.
(iii)Sort out headings of sections.
(iv)Sort clearpage problem, perhaps change to includegraphics.
(v)Sort out the webpage stuff.

Key words: stars:evolution – stars:formation – stars: pre-main-sequence – techniques: photometric – catalogues – (stars) Hertzsprung-Russell H-R diagram

1 INTRODUCTION

There is now strong evidence that as brown dwarfs (BDs) form they pass through a Classical T Tauri star (CTTS) phase, during which they possess a flared, dusty circumstellar disc from which they are actively accreting material (Jayawardhana et al. 2003; Mohanty et al. 2004). The accretion is thought to proceed via a magnetically-controlled funnel flow mechanism in which material from a truncated inner disc boundary falls onto the surface of the star along magnetic field lines (Camenzind 1990; Koenigl 1991; Mohanty & Shu 2008).

The truncated inner-edge of the circumstellar disc receives direct photospheric radiation and is strongly heated. This leads to an increased scaleheight, or 'puffing up' of the inner disc rim, and subsequent shadowing of the region immediately beyond it (Dullemond et al. 2001). The density-dependent nature of the dust sublimation temperature (Pollack et al. 1994) may also play a role in shaping the inner rim (Isella & Natta 2005; Tannirkulam et al. 2007).

As an aside, although we recognise that the inner hole in protostellar discs may be the result of giant planet formation or photoevaporation (Dahm & Carpenter 2009; Najita et al. 2007), these two mechanisms should result in a negligible mass-accretion rate (Dahm & Carpenter 2009) and therefore would represent a distinct evolutionary state of brown dwarf disc (BDD) sytems to that of the CTTS-like phase we are considering here.

The interpretation of the spectral energy distributions (SEDs) of pre-main-sequence (PMS) stars involves trying to distinguish the various contributions to the continuum from the hot spots at the base of the accretion flow, the photospheric flux, and the near-IR flux from the dusty inner disc. The complexity of the interplay between these contributions is excerbated by other, geometrical, effects such as the inclination (which changes the projected area of the inner disc wall visible to the observer) and the outer disc structure (which may obsure the inner disc for high inclincations) (Walker et al. 2004; Tannirkulam et al. 2007).

In surveys, particularly those attempting to discern the PMS disc fraction , this disentangling usually takes place using broad-band photometric measures and cuts in colour-colour or colour-magnitude space (Luhman et al. 2005, 2008; Gutermuth et al. 2008). The important quantity here is the separation in wavelength between the emission peaks for the stellar and thermal disc components, as it is these components which must be separated. For BDD systems it is likely that difficulties detecting the disc will be exacerbated by the lower temperatures of the photosphere and therefore the smaller separation in wavelength from the thermal disc emission component, compared to CTTS systems. Therefore, to derive disc fractions for BD populations we require detailed comparison models with which to guide disc candidate selection.

Comparison of accretion rates across the pre-main-sequence (PMS) mass spectrum has indicated that the accretion rate is strongly correlated with PMS mass, (Muzerolle et al. 2003; Natta et al. 2004, 2006), with an approximate form $\dot{M}_{\rm acc} \propto M_*{}^2$. Since in the canonical picture the accretion rate is driven by the disc viscosity, and should be indepedent of the mass of the central object, this correlation is somewhat surprising. There is some danger that the correlation is the result of, or at least strengthened by, the presence of observational biases (Clarke & Pringle 2006): At the high-mass (CTTS) end of the mass spectrum the lowest accretion-rates cannot be measured via continuum methods

⋆ E-mail: nathan@astro.ex.ac.uk (NJM)

since the excess is too small in contrast with the photospheric emission. The emission lines will also be weak, and indeed the Hα equivalent width (EW) may be less than the 10Å that traditionally demarcates classical from weak-lined T Tauri stars. Such objects should show doppler-broadened profiles, but the line wings will be weak, and the presence of underlying Hα absorption may become dominant. Thus there may be a population of low-accretion-rate CTTS which are current missing from the surveys.

There are also risks of observational biases at the low-mass end of the correlation. Radiative-transfer modelling of Hα emission from accreting BDs requires high temperatures ($>$ 10 kK) in the accretion funnels in order to recover the level of emission that is observed. (Cooling rate arguments can be invoked to explain the presence of such high temperatures). Recently some continuum measurements of accreting BDs have been conducted, and these broadly support the Hα rates (Muzerolle et al. 2003; Natta et al. 2004, 2006). Nonetheless it is worth considering the observed effect that mass accretion at typical CTTS rates onto a BD might have. Parity between the BD photospheric luminosity and the accretion luminosity occurs at relatively low accretion rates (Clarke & Pringle 2006). Such objects may not be detected as BDs at all in photometric surveys. Even before such an extreme case is reached, the additional luminosity provided by the accretion should have measurable effect on the BD colours. Furthermore the additional flux will be reprocessed by the disc, altering its scaleheight and possibly the shape of its inner edge.

Here we present a grid of models of BDD systems, including a self-consistent treatment of the photospheric and accretion luminosity sources and the interaction of that flux with the circumstellar disc. We investigate the impact of the luminosity of the central source on location and shape of the disc inner rim, as well as the large-scale structure and flaring of the outer disc. We construct synthetic colour-colour and colour-magnitude diagrams in order to examine the efficacy of the photometric selections used to isolate brown dwarfs and measure disc fractions (Luhman et al. 2005, 2008; Gutermuth et al. 2008).

The complete model grid, with derived photometry and isochrones, is available online through our browsing tool [1] which is described in Appendix B.

2   MODEL

In this Section we detail the physical model adopted and assumptions made (Section 2.1), then explain key elements of the radiative transfer code (Section 2.2). Then we discuss the derived values, such as broadband photometric magnitudes and colours (in Section 2.3). Some internal consistency checks are given in Appendix A.

2.1   Physical model and assumptions

2.1.1   Photospheric flux

In order to model an accreting BDD system we must first model the underlying photospheric flux. We have adopted

a BD stellar interior and atmospheric model grid and have then constructed the total photospheric flux for any input value of stellar age and mass by interpolating for surface gravity ($\log g$), effective temperature ($T_{\rm eff}$), radius ($R_*/R_\odot$) and luminosity ($L_*/L_\odot$). These values were then used to interpolate atmospheric spectra for flux (ergs s^{-1}cm^{-2}Å^{-1}) from 1200 to 2×10^7 Å. The spectra were subsequently resampled onto 200 logarithmically spaced points. Careful inspection ensured that no spectral features were removed during resampling. The stellar interior models used for this study are the 'DUSTY00' models of Chabrier et al. (2000) combined with the 'AMES-Dusty', atmospheric models of Chabrier et al. (2000), which are all available online [2]. For our $T_{\rm eff}$ range of $\approx$3000 K$<$ $T_{\rm eff}$ $<$1600 K the AMES-Dusty atmospheres are the most applicable (2700 K$>$ $T_{\rm eff}$ $>$1700 K). We did try including dynamic application of atmospheres based on the derived $T_{\rm eff}$, i.e. using AMES-Cond for $T_{\rm eff}$ $<$1700 K, but this resulted in large discontinuities between the model atmospheres and resulting spectra. Since this only affects stars at the very edge of our temperature range, i.e. for the oldest and lowest mass objects (for the AMES-Cond case), we have adopted the AMES-Dusty models throughout.

2.1.2   Accretion flux

We assumed blackbody emission for the accretion flux. The selected accretion rate was used to derive an accretion luminosity ($L_{\rm acc}$), where the material was modelled as free-falling from the disc inner edge onto the surface of the star. $L_{\rm acc}$ is calculated according to 1,

$$L_{\rm acc} = \frac{GM_*\dot{M}}{R_*}\left(1 - \frac{R_*}{R_{\rm inner}}\right), \qquad (1)$$

where M_* is the stellar mass, $\dot{M}$ the mass accretion rate, R_* the stellar radius and $R_{\rm inner}$ the radius of the disc inner boundary.

The initial inner disc radius was set to be the co-rotation radius (this is discussed in more detail in Section 2.1.3). During the radiative transfer simulations of the disc the final inner dust-disc radius may be beyond the co-rotation radius due to dust sublimation effects (see Sections 2.2.2 and 4.1.2 for an explanation). Once the accretion luminosity was derived, an adopted areal coverage (A), over the stellar surface, was used to calculate an effective temperature ($T_{\rm acc}$), for the accretion 'hot' spot, where

$$T_{\rm acc} = \left(\frac{L_{\rm acc}}{4\pi R_*^2 \sigma A}\right)^{\frac{1}{4}}. \qquad (2)$$

Finally, a blackbody flux distribution is generated at $T_{\rm acc}$ and added onto the intrinsic stellar photospheric flux. In general one would expect this to be an overestimate of the accretion flux, as for pre-MS BDs large convective zones are expected on the stellar surface, and some of the accretion energy may act to further drive these convective currents, meaning flux is lost. It is worth noting however that observationally UV excesses are often used to recreate and then subtract an assumed accretion flux using a blackbody flux curve, which is essentially the reverse of this method.

---

[1] http://www.astro.ex.ac.uk/research/bd_disc

[2] http://perso.ens-lyon.fr/france.allard/

2.1.3 Disc parameters

In this study we assume that accretion from the central star occurs along magnetically channelled columns from the inner disc boundary. For CTTS stars, Bouvier et al. (2007) show that the magnetic truncation radius (R_{mag}) is less than the co-rotation radius (R_{co}), where the angular Keplerian velocity of the disc is equal to the surface angular velocity of the central star. Calculations of the magnetic truncation radius depend on derivations of the surface magnetic field (Koenigl 1991). This is currently unavailable for BD stars, due to increased molecular species obscuring the Zeeman splitting signatures, that are normally used to derive stellar surface magnetic fields. Therefore, for our model grid we have adopted an initial inner disc radius as the co-rotation radius,

$$R_{\mathrm{inner}} = \left(\frac{GM_*\tau^2}{4\pi^2} \right)^{\frac{1}{3}}, \qquad (3)$$

where τ is the stellar rotation period and R_{inner} is the inner radius. This is effectively adopting a disc-locking mechanism (without associated angular momentum loss), as for disc-locked stars, $R_{\mathrm{mag}} \approx R_{\mathrm{co}}$, (Koenigl 1991; Shu et al. 1994). Therefore, for our model simulations, this inner edge radius is dependent on, and derived from, the adopted value of the rotational period for the central star, as well as being weakly dependent on the stellar mass. As discussed in Section 1, the inner disc can be cleared through a number of mechanisms, including binarity or Giant planet formation, photoevaporation or photoionisation of the disc and dust grain growth or settling. For BDD systems where a disc is modeled a treatment of dust sublimation is included (discussed in Section 2.2.2). However, the effects of binarity or Giant planet formation are neglected. Further to the stellar mass and period required prior to calculation of the inner disc radius, we require a disc mass (in stellar masses).

Although we solve for the vertical disc structure, the radial structure of the disc is a free parameter. We assume that the surface density varies as $\Sigma(r) \propto r^{-1}$.

For this work the disc outer edge was set at 300 AU, this was chosen as a maximum size of the circumstellar disc. Bouy et al. (2008) have shown that the disc outer radius has little effect on the resulting SED. However, in our subsequent paper we will include models for outer radii of 100 AU and plan to extend this parameter range further to smaller values of the outer radius in the future.

2.1.4 Naked and disc systems

The combined (accretion plus photosphere) SED is then used as a boundary condition for the TORUS radiative transfer code and as a benchmark set of SEDs to model 'naked' BD systems. The set of 'naked' photospheres (plus accretion) are diluted by the factor $(R_*/\mathrm{distance})^2$ to a distance of 10 pc. The 'negligibly' accreting, 'naked' stars can be used to produce absolute magnitude (and intrinsic colour) isochrones for comparison. The remainder are used to model systems showing active accretion where no disc is detected. For instance, Kennedy & Kenyon (2009) find 43 stars within their sample are actively accreting whilst no disc is detected (out of a total sample of 1253).

In summary the key required input variables to setup

the model grid are as follows: Stellar age and mass (which are used to derive the stellar flux) and accretion rate, areal coverage and rotation period (which are used to determine the the accretion flux and temperature). The disc parameters are set by a disc mass (expressed as a fraction of the BD mass), and a power-law distribution for the disc surface density.

2.2 Radiative transfer code: TORUS

In this section we briefly explain the key elements of the radiative transfer code used to model the BDD systems.
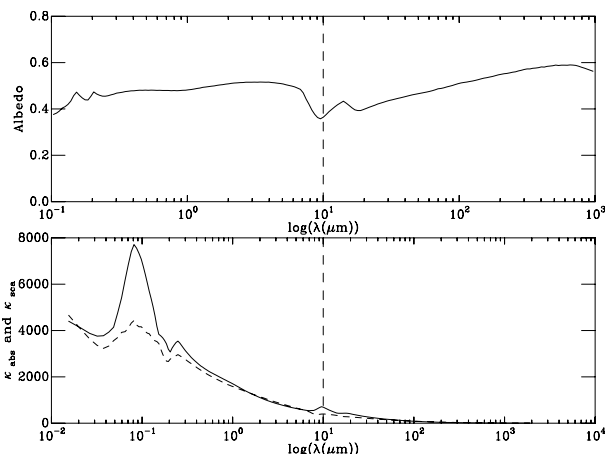
We have used the TORUS radiative transfer code which is described in Harries (2000), including the subsequent refinements i.e. addition of Adaptive-Mesh-Refinement (AMR) introduced in Harries et al. (2004). TORUS uses the method of Lucy (1999) solve radiative equilibrium. The simulation also self-consistently solves the equation of *vertical hydrostatic equilibrium* and dust sublimation for the disc (described in Tannirkulam et al. (2007)).

2.2.1 Dust Size distribution

We have adopted a similar dust model to Wood et al. (2002) with the size distribution of dust particle given by,

$$n(a)da = C_i a^{-q} \times exp^{[-(a/a_c)^p]} da \qquad (4)$$

. Where $n(a)da$ is the number of particles of size a (within the increment da), a_{c} is the characteristic particle size, with p and q simply used to control the shape of the distribution. C_i controls the relative abundance of each constituent species (i) in the dust. Wood et al. (2002) found that simulated SEDs fit observed SEDs better using this adjusted size distribution for the dust particles, as opposed to a simple power law. The best fitting values found in Wood et al. (2002) were q =3.0, p =0.6 with a_{c} =50 μm, also with an associated maximum and minimum grain size of a_{min} =5 nm and a_{max} =1mm. A slightly steeper power law dependence, with q =3.5 (corresponding to the canonical MRN distribution) is more widely adopted (Bouy et al. 2008; Morrow et al. 2008; Pascucci et al. 2008). Here we have adopted the values of Wood et al. (2002) except for the parameter q where we have used q =3.5. Wood et al. (2002) calculated the C_i values for amorphous carbon and silicon by requiring the dust to deplete a solar abundance of either component completely (using abundances from Anders & Grevesse 1989; Noels & Grevesse 1993). We have set C_i =1 and adjusted the species using a grain fractional abundance (an equivalent process to that of Wood et al. 2002), however we have adjusted these grain fractions using the updated solar abundances of Asplund et al. (2006). The resulting difference in opacity between grain fractions matching the work of Wood et al. (2002) and the new grain fractions is only a slight enhancement of the silicate feature (due to the relative abundance of Silicon increasing) which has little effect on the resulting SEDs. Figure 1 shows the resulting albedo, and scattering and absorption opacities, for our dust population, with a the vertical dashed line showing 10 μm.

Figure 1. Figures of the albedo (*top panel*), and scattering (dashed line) and absorption (solid line) opacities (*bottom panel*) against $\log(\lambda)$ (in μm) for our adopted dust population. For *both panels* the vertical dashed line is plotted at $10\,\mu$m to highlight the silicate features.

2.2.2   Dust sublimation and the inner disc edge

As our models assume magnetic-truncation at the co-rotation radius, we have implicitly generated an inner hole. This also means that the disc will have an inner wall at this radius. Evidence for inner walls in circumstellar discs is apparent from the SEDs of disc systems, where a peak in emission is found between 2 and $3\,\mu$m. The temperatures reached by such inner walls are expected to generate thermal flux contributions within this wavelength range (Dullemond et al. 2001).

For low-luminosity systems the dust sublimation radius (R_{sub}) will be coincident with the co-rotation radius. However should the combined photospheric and accretion luminosities be sufficient the inner disc will be heated sufficiently that the dust close to the co-rotation radius will be sublimated, and we must account for this in our models. Furthermore, since the dust sublimation temperature has a density dependence (Pollack et al. 1994), it is both the location and *shape* of the inner wall that can change (Isella ref; Tannirkulam ref).

Our treatment of dust sublimation is similar to that detailed in Tannirkulam et al. (2007), but with some enhancements to ensure a swift convergence of the sublimated rim. The dust sublimation proceeds as follows: An initial temperature distribution is found for the optically-thin limit by setting the global dust-to-gas ratio to a tiny value. Subsequent radiative equilibrium iterations are performed using the adopted dust-to-gas ratio of 0.01, but limiting the maximum optical depth across a given cell to τ_{max}. Cells whose temperature exceeds the local dust sublimation temperature have their dust-to-gas ratio set to zero. Radiative equilibrium iterations and sublimation sweeps are performed at $\tau_{\mathrm{max}} =$0.1, 1, and 10, with a final iteration of $\tau_{\mathrm{max}} = \infty$. Adequately solving the radiative-equilibrium necessiates resolving the disc's effective photosphere, and adaptive mesh refinement is used to split the grid at the optically-thin/optically-thick boundary in order that the maximum cell size at this boundary is < 1 at a wavelength of 5500 Å. Once a self-consistent sublimated rim has been determined the equation of hydro-

static equilibrium is solved throughout the disc, and the sublimation iterations are restarted (the change in the density structure from the hydrostatical equilibrium step naturally feeds back into the shape of the inner rim). Five hydrostatic equilibrium steps are performed to ensure convergence, although a stable disc structure is normally found after three such iterations.

For our model grid we have adopted a gas-to-dust ratio, ϵ, of 100, and the gas population is assumed essentially static with a zero optical depth.

2.2.3   SEDs

Once the radiative transfer code was completed simulated SEDs were generated. These SEDs can be generated for any distance and for any system-observer inclination. For our models we have set the distance, to 10 pc to create absolute flux SEDs and selected ten inclinations equi-spaced in $\cos i$ (0, 27, 39, 48, 56, 64, 71, 77, 84 and 90°). A further useful feature of the TORUS code is that the emitted photon packets which make up the SED are tagged on their way to the observer. These tags separate the packets into four groups. Firstly, packets are separated by source into thermal (disc) or stellar groups. These groups are then subdivided into those which reach the observer either directly or after scattering (for example see Figure 12). The resulting SEDs are discussed in Section 2.2.3.

2.3   Photometric systems and derived quantities

Many observational studies use non-spectroscopic data to derive the pertinent parameters. Therefore in order to examine the practical effects in the 'observational plane' we have used the SEDs to produce broadband photometric magnitudes, and subsequently colours. Broadband magnitudes were also derived in a large range of other filter sets not used explicitly in the analysis within this paper. These magnitudes are available online [3] and are briefly discussed in Appendix B. In addition, monochromatic fluxes have been derived for all filters, and again are available online and discussed in Appendix B.

In order to derive broadband photometric magnitudes and colours the SEDs of either the disc or naked systems were folded through the filter responses of the required photometric system. As the fluxes in all cases are absolute, derived for an observer to object distance of 10 pc, no conversion is required to derive absolute magnitudes and therefore intrinsic colours.

We have integrated using photon-counting and calibrated using a Vega spectrum for magnitudes in the optical and near-IR regimes. The filter bandpasses selected are, the optical system of Bessell et al. (1998) for *UBVRI* and the *CIT* system of Elias et al. (1982); Stephens & Leggett (2004) for *JHK*, with the required shift of $-0.015\,\mu$m as prescribed by Stephens & Leggett (2004).

We have also derived magnitudes in the mid-IR range using the IRAC and MIPS systems of the *Spitzer* space telescope. These magnitudes were derived using a conversion of flux to Data Number (DN) and calibrated using zero

---

[3] http://www.astro.ex.ac.uk/research/bd_disc

points derived from the zero magnitude fluxes published in the IRAC handbook [4] and the MIPS instrument calibration website [5].

These specific filter sets have been chosen due to their ubiquitous use and suitability for the derivation of the key stellar parameters of age, mass and, for populations, disc fractions. Therefore, by studying the changes of magnitudes (and colours) in these photometric systems we can test the predicted effects on these derived parameters caused by changes in the input parameters of our model grid. The optical magnitudes *VI* are used to explore age related effects of varying the parameter space. Flux in the *VI* bands is only minimally affected by accretion flux (Gullbring et al. 1998) and disc thermal flux (Hartmann 1998) and, additionally, in a *V, V-I* CMD, the reddening vector lies parallel to the pre-MS, minimising any age effect of extinction uncertainty, (for a full discussion see Mayne & Naylor 2008; Mayne et al. 2007). The near-IR passbands of *JHK* are most often used to derive stellar masses as for pre-MS objects the reddening vector, in for instance, a *J, J-K* CMD, is almost perpendicular to the isochrones, minimising the mass effect of extinction uncertainties (the *CIT* systems was chosen to match Chabrier et al. 2000). Finally, as is now well documented the *Spitzer* IRAC passbands provide the best data with which to unambiguously separate naked and star-disc systems (Luhman et al. 2005). In addition, at longer wavelengths, the MIPS instrument provides sensitivity to disc systems at much larger radii (or debris discs).

Once the model grid was completed several checks were performed to verify the consistency of our results. For each individual model these checks were passed to our satisfaction before publication. Some problems remain, and these are explained in Appendix A.

3 PARAMETER SPACE

This section details the range of each of the input parameters we have varied and, where possible, gives justification for the selected ranges from published observations. The simulations in this paper cover variations in the stellar mass, stellar age, stellar rotation rate, accretion rate, the areal coverage of the accretion stream, disc mass fraction and the system inclination. A summary of the values adopted for each input variable is shown in Table 1.

3.1 Mass

Representative masses within the BD regime were chosen as follows: 0.01, 0.02, 0.03, 0.04, 0.05, 0.06, 0.07 & 0.08 $M_\odot$.

3.2 Age

Typical disc lifetimes for solar type stars are of order 10 Myrs (Haisch et al. 2001). Therefore, we have adopted input ages of 1 and 10 Myrs for our model grid, to span the approximate range of ages over which the discs influence will be important.

3.3 Rotation rate

Data for rotation rates, from periodic variability surveys, are widely available for a range of different age clusters of TTS. However, fewer studies exist on the rotation rates of BD mass objects. Rotation period data for σ Ori, at an age of ≈ 3 Myrs (Mayne & Naylor 2008), is studied in Scholz & Eislöffel (2004), where periods are found over the range $5.78-74.4$ hours ($\approx 0.24-3.1$ days) for BD mass objects. Scholz & Eislöffel (2005) study rotation period data for stars in the vicinity of ϵ Ori, with an assumed age of ≈ 3 Myrs (Zapatero Osorio et al. 2002) and the ONC at an age of ≈ 2 Myrs (Mayne & Naylor 2008). Rotation periods, from photometric variability, in the range $4.7-87.6$ hours ($\approx 0.2-3.65$ days) for BD mass stars are found. Joergens et al. (2003) study the rotational periods of BD (and very low mass stars) in the Chameleon I region. This region is $\leqslant 1$ Myrs old, and the authors find rotation periods of 2.19, 3.376 and 3.21 days for their BD mass counterparts.

In some cases the periodic variability is irregular and assumed to come from active accretion hot spots on the BD surface (see Bouvier et al. 1995; Herbst et al. 2007, for discussion of variability causes), indicative of active accretion. All the studies mentioned infer a disc locking mechanism. Furthermore, Scholz & Eislöffel (2004) and Scholz & Eislöffel (2005) find evidence for a *mass* $\propto$ *period* relationship extending into the BD regime. Additionally, Joergens et al. (2003) propose a shorter lifetime of ≈ 5 Myrs for BD discs, inferred from a shorter derived disc locking timescale. However, as discussed in the previous studies, an imperfect disc locking mechanisms is also hypothesised as responsible for the less significant loss in angular momentum out to ages of 10 Myrs, for BD discs. The data on BD rotation rates, disc presence and disc locking are summarised and discussed in Herbst et al. (2007).

Therefore, to create a set of useful models to help contextualise the observational constraints, for study of disc locking mechanisms, we must adopt a realistic, and bounding range of rotation rates. For our model grid, and associated age range (<10 Myrs), we have selected 0.5 and 5 days. With the limits set at at the approximate median of faster rotators and the edge of the slower rotators.

3.4 Areal Coverage

As discussed in Section 3.3 evidence for irregular periodic variability has been found in BD stars with detections of associated stellar discs. This is construed as evidence for accretion hot spots formed as magnetically channeled material hits the stellar surface (see discussion in Bouvier et al. 1995; Herbst et al. 2007). The irregularity is thought to be caused by changes in the magnetospheric structure and accretion rate (Bouvier et al. 1995). For our model we have assumed that disc material is disrupted at the co-rotation radius and channeled onto the star in the form of accretion hot spots with a characteristic temperature. Therefore, to calculate the characteristic temperature and the resulting blackbody accretion flux we must adopt an accretion rate and areal coverage of the accretion stream.

Little observational evidence can be found for approximate sizes of accretion hot spots due to their more transient nature and often smaller coverages, when compared to cooler

or 'plage' spots (Herbst et al. 2007). Bouvier et al. (1995) modeled the size of the cool spots on solar-type stars for a selection of periodically variable candidates. They found projections of cooler spots, onto the stellar disc, of a few to 60%. Bouvier et al. (1995) also found projected sizes, onto the stellar disc, of typically a few % to around 10% for hot spots. Bertout et al. (1996) used observations of YY Orionis monitoring flux amplitude variations as a function of wavelength to derive a probable hot spot area of around 10%. The spot temperature was also modeled for YY Orionis in Bertout et al. (1996), resulting in a best fitting areal coverage of 11%. Therefore, to bound the probable areal coverage range of the accretion hot spots we have adopted areal coverages of 1 and 10%.

3.5 Accretion Rate

XXXX TJH check this now

Accretion rates derived for pre-MS stars are of order $\log \dot{M} = -6$ to -11 (Natta et al. 2006). With the largest accretion rates found in so-called FU Orionis type objects (after the object where they were first observed). For the more typical accretion rates ($\dot{M} = 10^{-11}$ to $10^{-8.9} M_\odot yr^{-1}$, for TTS, Dahm & Carpenter 2009), several studies have now suggested that the accretion rate is strongly correlated with the mass of the central star. This relationship was perhaps first suggested by Muzerolle et al. (2003) using various accretion diagnostics. Later, (Muzerolle et al. 2005) derived a relationship of approximately $\dot{M} \propto M_*^2$. Further evidence was put forward by Natta et al. (2004), where accretion rates as low as $5 \times 10^{-12} M_\odot yr^{-1}$ were found for BD stars. More recently, even lower accretion rates of $\approx 10^{-13} M_\odot yr^{-1}$, have been derived for BDs by Herczeg et al. (2009). Further support for a dependence of accretion rate on stellar mass was apparent in the significantly more homogeneous dataset of Natta et al. (2006). Natta et al. (2006) analysed a set of accretion rates and masses derived for pre-MS stars in ρ Ophiuchi and compared these results to stars in Taurus. They found that the accretion rate scales with central object mass, into the BD regime.

For any $\dot{M} \propto M_*$ relationship to be ratified, clearly, the associated mass derivations must be shown to be accurate. For the BD mass regime it has been demonstrated that classification, either spectroscopic or photometric, and therefore accurate mass derivation is exceedingly difficult for BDD systems (Walker et al. 2004). The inclusion of significant levels of accretion flux will act to exacerbate this problem. Essentially, as BD mass objects have relatively cool photospheres, compared to the temperature of the accretion hotspots, meaning that for lower accretion rates, than for their CTTS counterparsts, the accretion flux dominates the small wavelength regime of the SED.

Therefore, to strengthen, or reject, any stellar mass to accretion rate relationship, the limits of observational classification (and mass derivation) of accreting BDD systems must be understood. To provide a benchmark model grid of such systems, with which to aid interpretation of the observational data, we must select a range of accretion rates including and exceeding those detected for systems previously classified as BDs.

As the relationship $\dot{M} \propto M_*^2$ predicts lower accretion rates for BD mass objects it is essential that we model systems at higher accretion rates, which may have been missed in current observational studies. Therefore, we have adopted accretion rates of $\log \dot{M} = -6, -7, -8, -9, -10, -11$ & -12.

3.6 Disc Mass

Previously studies modeling BD discs have adopted a range of disc mass fractions, for instance (Walker et al. 2004) use 0.1, 0.01 and 0.001M_*. Wood et al. (2002) fit observed spectra with modeled SEDs to derive a disc mass of 0.003M_*, for HH 30 IRS. Subsequent derivations of disc masses have converged to within an order of magnitude, with the following specific results: 0.03M_* (ρ Ophiuchi, Natta et al. 2002), 0.055M_* (GM Aurigae, Rice et al. 2003), 0.03M_* (GY 5, GY 11, and GY 310, Mohanty et al. 2004) and 0.022M_* (2MASS J04442713+2512164, Bouy et al. 2008). As the derived disc masses all have a similar order of magnitude we have adopted $M_{\rm disc} \approx 0.01 M_*$. As changes in disc masses are expected to change the resulting SED less than perhaps, accretion rate for example, we have not varied the disc mass for this study. The results of simulations varying this parameter will be published in a future paper.

3.7 Inclination

Discs around BD stars exhibit increased flaring, due to the reduced surface gravity in the disc (Walker et al. 2004). This increased flaring, and therefore larger scaleheight of the disc results in a smaller opening angle, when compared to higher mass stars and their circumstellar discs. As has been shown in Walker et al. (2004) effects caused by variations in the system inclination angle are much more significant for BDD systems, again compared to their higher mass analogues. Therefore, we have simulated ten observer to system inclination angles spaced evenly in $\cos i$ space, namely, 0, 27, 39, 48, 56, 64, 71, 77, 84 and 90°.

A final list of all varied parameters and their values can be seen in Table 1.

4 RESULT AND ANALYSIS

In this Section we first discuss the physical structure, both density and temperature, of the BDD disc systems (Section 4.1) across our parameter space. Then we discuss the resulting simulated SEDs for these BDD systems (Section 4.2). Finally, we produce simulated photometric observations (Section 4.3). These simulated observations allows us to show that recovery of the input masses and ages for our accreting BDD systems is unreliable. We show that despite an intrinsic relationship between rotation rate and initial inner edge position we do not recover a rotation rate correlation with IR excess. In addition, despite not intrinsically including a dependence of accretion rate on stellar mass in our grid. We show that current observational techniques and theoretical models applied to the grid would result in a relationship of this type being derived.

4.1 Disc Structure

The initial density structure has the the disc surface density conserved, $\Sigma^{\beta-\alpha}$. The initial scaleheight, $h \propto r^\beta$, where r is

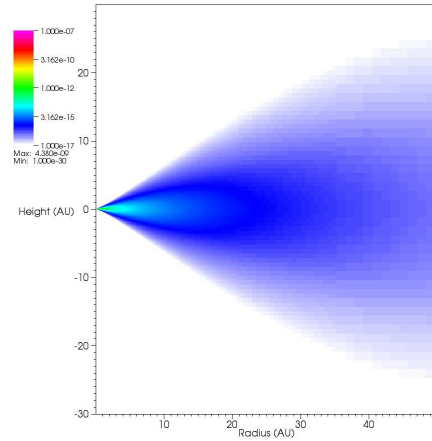| Input parameter	Values (# values)
Mass ($M_\odot$)	0.01, 0.02, 0.03, 0.04, 0.05, 0.06, 0.07 & 0.08 (8)
Age (Myr)	1 & 10 (2)
Rotation period (days)	0.5 & 5 (2)
Areal coverage (of $\dot{M}$, %)	1 & 10 (2)
Accretion rate ($\log(\frac{\dot{M}}{M_\odot}yr^{-1})$)	$-6, -7, -8, -9, -10, -11$ & -12 (7)
Disc mass (M_*)	0.01 (1)
Inclination ($^\circ$)	0, 27, 39, 48, 56, 64, 71, 77, 84 & 90 (10)

Table 1. List of all varied input parameters. Resulting in a total number of models of 448 (plus 40 models without radiative transfer simulations for the naked BDs) and 4480 SEDs (plus 40 for naked BDs).

the radial distance from the star, and the density, $\rho \propto r^{-\alpha}$. The initial values of α and β were 2.1 and 1.1 respectively. The values for α and β were chosen to optimise resolution of the vertically evolving disc, but minor variations are largely inconsequential as the systems evolves from this state. In our models we have, however, placed at the inner disc edge at the co-rotation radius, as opposed to the dust destruction radius used in Walker et al. (2004). The initial disc scaleheight at 100 AU, $h(100)$, was set to 25 AU. As the simulation used vertical hydrostatic equilibrium and dust sublimation, both the disc scaleheight and inner edge location then evolved in the systems dependent on the input parameters. In this section we discuss the structure of the discs in terms of these two generated characteristics, i.e the disc scaleheight and inner edge location.
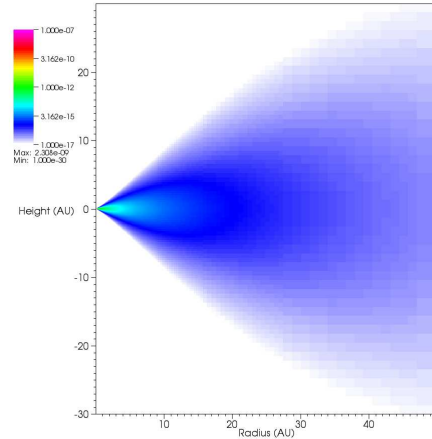
4.1.1 Disc Flaring

As discussed in Walker et al. (2004) discs around CTTS stars have scaleheights at 100 AU of between $h(100)$=7 to 20 AU, whereas for BDD systems, $h(100)$=20 to 60 AU (for 0.08 and 0.01 $M_\odot$ respectively). Our models adopt the same formalism for solving hydrostatic equilibrium and therefore, at negligible accretion rates, our disc scaleheights are comparable. As the accretion rate increases the flux levels of the central star increase and lead to heating of the disc which in turn leads to vertical expansion. For our models we found that levels of vertical flaring increased marginally with accretion rate. Significant differences, more than >5 AU increase in $h(50)$, in the vertical structure were not apparent until the high accretion rates of $\log\dot{M}= -7$ and -6. Figures 2 and 3 show the density structure ($log(\rho)$) in the disc from radial distances of 0 to 50 AU for example systems ($M_* = 0.04M_\odot$, Age=1 Myrs, τ=5 and areal coverage=10%), with accretion rates of $\log\dot{M}= -12$ and -7, respectively.

Figure 2 shows that for a typical BDD system the resulting disc is highly flared and therefore, the opening angle for stellar radiation is small. As discussed the flaring for BDD systems was found to be larger than CTTS systems by Walker et al. (2004). Walker et al. (2004), state that the degree of disc flaring depends on the disc temperature structure and the mass of the central star, with the disc scaleheight $h \propto \frac{T_{\mathrm{disc}}}{M_*}^{1/2}$ (Shakura & Syunyaev 1973). Recently, Ercolano et al. (2009) suggest the inverse relation of flaring with stellar mass, i.e. $h \propto M_*$. This suggestion was based on evidence from Allers et al. (2006), where SEDs for 17 systems in the mass range $6M_{\mathrm{Jup}} < M_* < 350M_{\mathrm{Jup}}$ were fit with flared or flat disc models. In general, Allers et al. (2006) find that lower mass objects achieve better fits with

Figure 2. Figure showing the density structure ($log(\rho)$) of the BDD system with $M_* = 0.04M_\odot$, Age=1 Myrs, τ=5, areal coverage=10% and accretion rate of $\log\dot{M}$=−12.

Figure 3. Figure showing the density structure ($log(\rho)$) of the BDD system with $M_* = 0.04M_\odot$, Age=1 Myrs, τ=5, areal coverage=10% and accretion rate of $\log\dot{M}$=−7.

the flat disc models and higher mass objects with the flared discs.

The results of Allers et al. (2006) show that above a mass of $50M_{\mathrm{Jup}}$ all objects (6/17) are better fit with flared discs. Whilst at masses below $50M_{\mathrm{Jup}}$ only one object is better fit by the flared disc model, with the remaining objects (10/17) better fit with flat models. Whether, this result is statistically significant enough to assert a $h \propto M_*$ is doubt-

ful as the fitting process contains, presumably two fixed scaleheight distributions. Therefore, for our study we continue to assume that our flared BDD systems will have larger characteristic scaleheights than typical CTTS systems.

A quick comparison of Figures 2 and 3 show an increase in the scaleheight at 50 AU of >5 AU, as the accretion rate moves from $\log \dot{M} = -12$ to -7. However, despite this small change with high levels of accretion our grid shows scaleheights comparable to the work of Walker et al. (2004) and as such result in similar consequences for the SEDs and photometric magnitudes. The effects of this flaring and the increase in flaring for very high accretion levels on SEDs and photometric magnitudes are discussed in Sections 4.2 and 4.3, respectively.

4.1.2   Inner edge

Our models include a sophisticated treatment of dust sublimation (described in Section 2.2.2). In contrast to the models of Walker et al. (2004), who apply a dust destruction radius, we set the initial inner radius of the disc at the co-rotation radius of the system. However, as our models then sublimate dust during the temperature convergence routine this inner edge location may change. As the flux levels of the central star increase with increasing accretion rates the flux incident on the inner edge increases and leads to increasing erosion of the inner edge of the dust disc.

As the inner edge moves its temperature is expected to change, this has been predicted to lead to a correlation of inner edge position and IR excess (Meyer et al. 1997). This may act to bias surveys correlating rotation rates with IR excess to search for evidence of disc-locking. However, the flux from the inner edge will usually peak between 2 and $3\,\mu$m (Dullemond et al. 2001), given that the dust sublimation temperature peaks at $\approx 1400\,$K for canonical densities. This means that for models where dust is sublimated the inner edge will have maximum temperatures of $\approx 1400\,$K and this correlation of disc position and temperature will be lost.

Equation 3 shows that as the rotation period, of the star, increases the co-rotation radius decreases. This will result in, initially, shorter period systems having closer and hotter inner edges than their longer period counterparts. In addition, if the accretion rate is increased in these systems the incident flux on the inner wall will increase leading to a rise in the temperature of the inner edge. At some point, in both cases the dust sublimation temperature may be reached, leading to a change in radial position of the wall. In addition, the temperature of the inner edge will then tend to a maximum temperature, of the dust sublimation temperature. Figure 4 shows the total stellar luminosity (accretion luminosity plus the intrinsic stellar luminosity), in $\log(L_*/L_\odot)$ against the change in inner disc location, $R_{\rm co} - R_{\rm inner}$ in units of AU (*top panel*) and R_* *bottom panel*. This change in inner edge location is from the initially set co-rotation radius to the final radius after dust sublimation, if applicable.

The *top panel* of Figure 4 shows that as the luminosity increases the total change in the inner radius increases as more of the disc is sublimated. The total change for lower luminosities at lower than $0.2 \log(L_*/L_\odot)$ is small (less than 0.02 AU). As the luminosities increases to larger, and extreme values, due to increasing accretion, the dust subli-
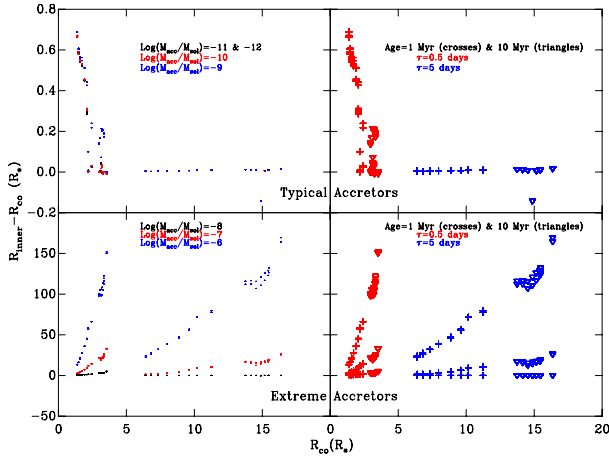

Figure 4. Figure showing the combined stellar luminosity (accretion plus intrinsic stellar luminosity) in units of $\log(L_*/L_\odot)$ against the change in inner edge location shown in units of AU (*top panel*) and R_* (*bottom panel*).

mation increases. In the *bottom panel* the change in inner radius tends towards around $120\,R_*$. Increases in accretion rate, for extreme accretors, dominates the increase in stellar luminosity. As pre-MS stars age they contract. Therefore, for lower accretion rates, younger, and therefore larger stars will have greater luminosities than the equivalent older stars. Therefore, the major contributors to the X-axis of Figure 4 are controlled by the input parameters of accretion rate and age. The initial inner wall radius was set as the magnetic co-rotation radius (see Section 2.1). This distance is a strong function of rotational period, with $R_{\rm inner} \propto \tau^{2/3}$ (see Equation 3) which is in turn a function of stellar radius. The stellar radius itself is then a function of the stellar age. Therefore, the initial inner wall edge position will change as a function of the input variables of rotational period and age. The initial position of the inner edge will control the amount of the stellar flux intercepted by the inner edge wall. Therefore the amount that the disc will be sublimated will also be a function of the initial position of the inner edge.

Figure 5 shows the initial inner edge position, or the co-rotation radius (R_*) against the change in inner edge location ($R_{\rm inner} - R_{\rm co}$, R_*). The *panels* of Figure 5 then shows these data for two accretion levels and at the two ages and rotation periods. These input variables for our model grid are the underlying variables controlling, as discussed, the dust sublimation process. The *top panels* are for models with accretion rates of -9, -10, -11 and -12 $\log(\frac{\dot{M}}{M_\odot}yr-1)$, classed as typical accretors here and throughout the rest of this work. The typical accretors are then separated further into three groups in the *top left panel* specifically, -9, -10 and -11 & -12 $\log(\frac{\dot{M}}{M_\odot}yr^{-1})$ (blue, red and black dots respectively). The *bottom panels* show the data for models with accretion rates of $\log \dot{M} = -6$, -7 and -8 (blue, red and black dots respectively), which we have classed as extreme accretors. The *right panels* show the data separated by age, with 1 and 10 Myrs (as crosses and triangles respectively), and rotation period, with 0.5 and 5 days (as red and blue symbols respectively).

The classification of models into typical and extreme accretors is based on observations (see discussion in 3.5) and

Figure 5. Figure showing data for the co-rotation radius (R_{co}) against the change in inner edge location ($R_{inner} - R_{co}$) both in units of R_*. The typical accretors are shown in the *top panels* and the extreme accretors in the *bottom panels* (see text for explanation). The accretion rates are then further subdivided. The *top left panel* shows accretion rates of log $\dot{M} = -9$, -10, -11 & -12 as blue, red and black dots respectively. In the *bottom left panel* accretion rates of log $\dot{M} = -6$, -7 and -8 are shown as blue, red, and black dots. In addition the *left panels* separates the systems by age and period. The systems with ages of 1 and 10 Myrs are shown as crosses and triangles respectively. The systems with rotation rates of 0.5 and 5 days are then shown as red or blue symbols respectively.

also evidence from the simulations themselves. Figure 5, *left panels*, shows that dust sublimation does not become significant until accretion rates of around log $\dot{M} = -9$ and increases dramatically with increasing accretion rate thereafter. This accretion rate is also, unsurprisingly the accretion rate at which the underlying photospheric emission is overwhelmed by the accretion flux, and the photospheric features are lost (see Section 4.2). The *right panels* of Figure 5 show that dust sublimation occurs only for rotation periods of 0.5 days for typical accretors. For the extreme accretors the systems with both rotation periods undergo sublimation but the effect is more significant in the systems with shorter rotation periods. The *right panels* also show that for extreme accretors the older systems undergo more dust sublimation, whereas for the typical accretors the older systems undergo little or no dust sublimation.

The density of material in the disc falls with increasing radius from the star ($\rho \propto R_*^{\alpha}$). The dust sublimation temperature is also density dependent (Pollack et al. 1994). Therefore, for systems where the inner edge has been eroded significantly from the co-rotation radius the temperature of the inner edge will fall as the final radius increases. In this case a correlation of inner edge temperature and inner edge radius is expected with a resulting slope determined, at least in part, by the radial density distribution of the disc. In this case the the final inner edge radius and therefore temperature is no longer strongly correlated with the rotation rate. Figure 6 shows the final inner edge location (R_{inner}, R_*) against the temperature of the inner wall (T_{inner}, K). The *left panel* shows the systems designated as typical accretors and the *right panel* those with extreme accretion rates. For *both panels* the systems with rotation periods of 0.5 and 5

days are plotted in red and blue respectively. Those systems where the change in inner radius was greater than $1 R_*$, and therefore classes as significantly sublimated, are plotted as crosses. These systems are only present for the extreme accretors, as shown in Figure 5. Furthermore, for the typical accretors Figure 5 shows that only the shorter period objects, in general, experience any disc erosion at the inner edge.

Figure 6 shows that for those systems where significant disc erosion ($\Delta R_{inner} > 1.0 R_*$) has occurred the resulting temperature of the inner edge is weakly correlated with the inner edge radius, but, critically, not correlated with rotation rate. The inner edge temperatures of the remaining systems for the extreme accretors are slightly anti-correlated with the radius to the inner edge. For the systems with typical acccretion rates, and longer periods, Figure 6 shows there is again a weak correlation between the radius to, and the temperature of the inner edge. For the shorter period models with typical accretion rates there is no clear correlation between the temperature at the inner edge and radius to this edge. The *left panel* of Figure 6 shows that, taken as a whole, our models with typical accretion rates show a clear correlation between the temperature at the inner edge and the radius to this boundary. This agrees with the work of Meyer et al. (1997) where this correlation is found for there $R_{inner} = 1 - 12 R_*$ and $\dot{M}_{acc} = 10^{-9}$ to $10^{-5} M_\odot yr^{-1}$, for flat disc models. Meyer et al. (1997) use this correlation, and the derivation of IR magnitudes, to predict a relationship between IR excess and radius to the inner wall. Our data indicate that this correlation, for typically accreting systems will translate into a correlation between rotation rate and IR excess. This could have important implications for studies of disc-locking where disc presence is examined as a function of rotation rates, provide an intrinsic bias. In practice however, this correlation is weak, an unobservable, in our data due to inner disc wall shape, inclination and flaring effects. This is discussed in more detail in Section 4.3.

For simulations without dust sublimation, and analytic density distributions, the inner disc edge is characterised solely by the initial disc density prescription. If one includes vertical hydrostatic equilibrium the scaleheight of the disc inner edge can change but the radial distribution of dust will not. Dust sublimation physics will alter the vertical structure, but crucially will also alter the radial distribution of dust. This means that dust sublimation effects will control the shape of the inner disc wall and possibly change this from a vertical wall. Evidence that real inner disc boundaries (for CTTS) are not vertical walls comes from a lack of dependence of the derived IR excess on system inclination (Tannirkulam et al. 2007). As discussed in Section 2.2.2 the disc inner hole can be created by several mechanisms, however, for this study we have only included a treatment of magnetic truncation (initially) and subsequent dust sublimation. The effects of dust sublimation have been shown to produce curved inner walls due to the temperature and density dependence of the dust sublimation temperature (Isella & Natta 2005). The curved boundary in this case is convex, as density increases towards the midplane of the disc, the dust sublimation temperature increases, meaning the destruction radius moves closer to the star. A curved inner boundary is also found to result from dust sublimation in Tannirkulam et al. (2007). In Tannirkulam et al. (2007)

Figure 6. Figure showing data for the inner edge location (R_{inner}, R_*). The typical accretors are shown in the *left panel* and the extreme accretors in the *right panel* (see text for explanation). In *both panels* separate the systems by period, with those systems with rotation periods of 0.5 and 5 days shown as red and blue symbols respectively. In addition systems where the total change in the inner radius is greater than $1R_*$ are marked as crosses (this is only achieved by some systems classed as extreme accretors).

two populations of dust grains where included with different scaleheight distributions. This is essentially a simple model of grain growth and subsequent midplane settling. Tannirkulam et al. (2007), found a concave inner disc boundary, this is due to the larger grains cooling more efficiently. These larger grains dominate the dust towards smaller vertical distances from the midplane, and therefore the increased cooling means that the dust sublimation temperature is reached at closer radii. The implications of the inner edge shape for the simulated SEDs and photometry are discussed in Section 4.2 and 4.3.

For systems where dust sublimation does not occur, or is minimal the inner edge of the system will remain as a vertical wall, as prescribed by our initial density distribution. However, as one increases the flux levels of a given system, by increasing the accretion rates (or moving to younger ages) the inner edge will increase in temperature. As the flux levels increase, in a given model, the dust at the inner edge will sublimate. The dust in the regions of lowest density or maximum flux interception will be preferentially destroyed. This will lead to a reduction in the scaleheight and a slight concave cavity at the inner wall. The inner edge will then move towards a convex boundary as the inner edge is forced radially outward towards regions of lower density with in-

creasing flux levels. This outward movement will result in the outer, vertical, regions of the dust disc eroding. Increasing the flux still further will lead to significant dust sublimation and an outward migration. This subsequent migration will move the inner edge into regions of lower density and greater scaleheight.

The transition in shape and position of the inner edge for a given model as the accretion rate, and therefore flux levels, are increased is shown in Figures 7 to 11. The model chosen for illustrative purposes has the following parameters, M_*=0.04$M_\odot$, Age=1 Myrs and areal coverage=10%. The model shown in Figure 7 has τ=5 days and accretion rate log $\dot{M}$= −12 (model shown in Figure 2), with Figures 8 to 11 showing models with τ=0.5 days and accretion rates log $\dot{M}$=−12, −9, −7 and −6. The *right panels* of Figures 7 to 11 show the temperature structure of the final converged disc structure. The *left panels* of Figures 7 to 11 show the final log(ρ) distribution for regions where dust is present, scaled to a different minimum density (log(ρ_{min})= 1^{-13}) compared to Figures 2 and 3. The lower (log) density threshold is used in this case to better trace the inner edge and denser regions of the disc, whereas Figure 2 and 3 show the outer diffuse regions of the disc, or disc limits. Additionally, for Figures 8 to 11 (the sublimated systems), the *left panels* also show

the initial density, in the same units as the final density, this is shown as a background grey scale (with the same maximum and minimum as for the final density) to illustrate the effects of sublimation.

Figure 7 shows the inner disc edge as a vertical wall with no dust sublimation, the inner wall has not changed location from the initial disc description. The *right panel* of Figure 7 shows that the corresponding temperature structure is smooth and interpolation at the inner edge yields a temperature of 900 K. For the shorter period model the inner edge has undergone some dust sublimation. The *left panel* of Figure 8 shows that the inner edge has lost dust slightly, preferentially, along the midplane. Again for Figure 8 the change in inner edge location is small, 0.45R_* (1.0×10^{-3} AU), at the sublimation (and inner wall) temperature is 1450 K, for a density of 2.5×10^{-8} (g/cm^3) (*right panel* of Figure 8).The *left panel* of Figure 8 shows that for even for a negligible accretion rate of log $\dot{M}=-12$, sublimation has begun to erode the inner edge, for the younger and faster rotating systems. Here the final density distribution has moved radially outward as can be seen by comparing the grey and colour scales in the *left panel* of Figure 8. Additionally, the inner edge has become slightly concave. As the flux levels of the central star increase the temperature of the inner edge surpasses the sublimation temperature at an increasing radius, destroying more of the disc and pushing the inner edge radially outwards. The *left panel* of Figure 9 shows that for an accretion rate of log $\dot{M} = -9$, increased sublimation has pushed the inner wall slightly farther from the star (when compared to Figure 8), here, ΔR 0.52R_* (1.1×10^{-3} AU), and T_{inner} 1450. Again the final density distribution has moved radially outward as can be seen by comparing the grey and colour scales in the *left panel* of Figure 9. The *right panel* of Figure 9 shows that the gas interior to the inner edge extending down to the co-rotation radius, which is not sublimated, will reach temperatures in excess, or equal to, the inner edge, which in this model is 1400 K. Such hot gas inner discs interior to the dust disc have been postulated through SED fitting (Eisner et al. 2005; Tannirkulam et al. 2008). Again, the shape of the inner wall has changed in Figure 9, the top and bottom sections of the disc have eroded and the inner wall is convex. The model in Figure 9 has an accretion rate of log $\dot{M}=-9$, which is the transition point between our two groups of accretors, typical and extreme. Figure 9 shows that for typical accretion rates, and faster rotation periods (and younger ages) significant dust sublimation is expected to occur at the inner edge, resulting in a curved inner wall at around 1400 K. Increasing the accretion rate, and therefore flux levels still further leads to significant erosion of the inner disc. For the extreme accretors the dust sublimation at the inner edge now changes the inner wall position by many multiples of the stellar radius. Figures 10 and 11 are for systems with accretion rates typical in outburst or episodic accretion systems, log $\dot{M}= -7$ and -6 respectively. The inner edges for these systems are eroded radially by 7.1 and 36.1 (R_*) respectively (0.016 and 0.080 AU, respectively), visible by comparing the grey and colour scales of Figure 10 and 11. As this occurs the disc inner edge moves far enough that the density drop (with radius) occurring in the disc causing the sublimation temperature to fall. Consequently the disc inner edge becomes cooler as it can not sustain temperatures above the
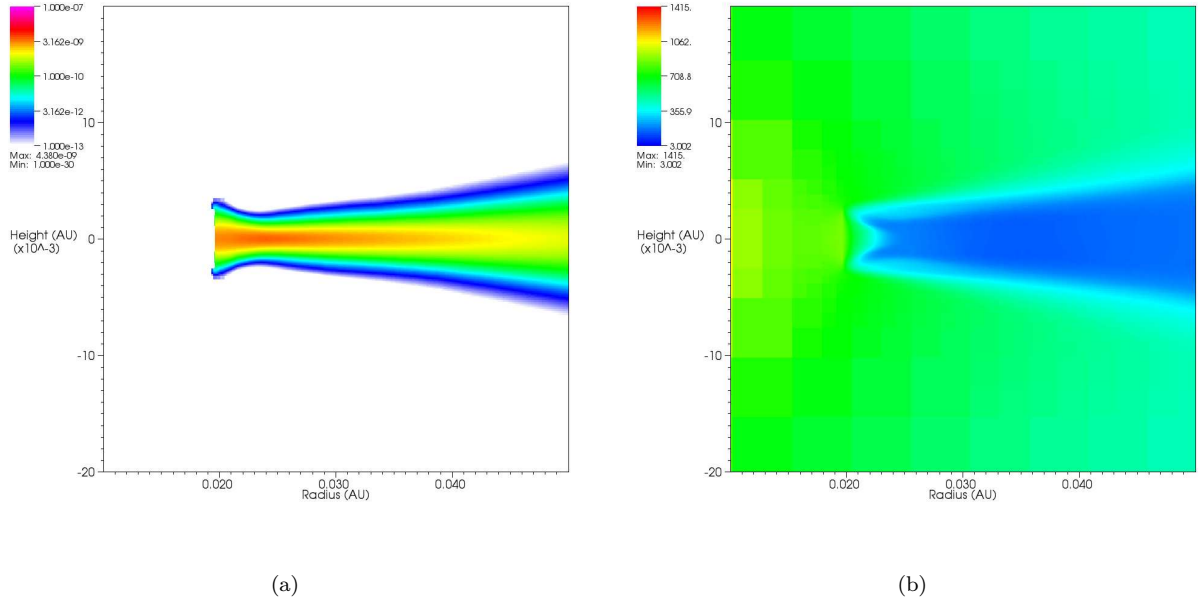
sublimation temperature. This is shown in the *right panels* of Figures 10 and 11, with approximate temperatures at the inner edge of 1370 and 1260 K. In addition, the inner edge has become concave and, again due to changes in the underlying disc density distribution, much larger in scaleheight.

A similar sequence is apparent across the grid for set masses. However, the balance of the rotation period, and therefore inner edge location, and age and areal coverage, therefore flux levels, leads to changes in the accretion rate at which the dust sublimation starts. However, in almost all cases the dust sublimation does not become significant until at least log $\dot{M}=-9$ (as discussed above).
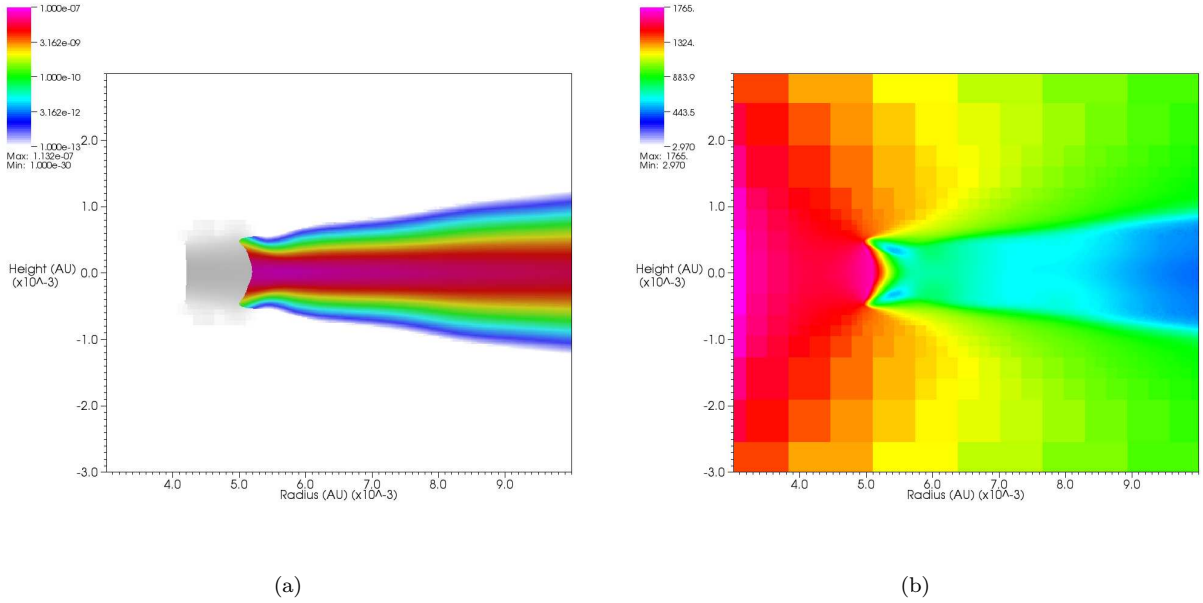
4.2 SEDs

The resulting converged disc structures, as discussed in Section 2.2.3 are then used to create simulated SEDs. In this section we explore features in these derived SEDs and link them back to the physical structures within the disc discussed in Section 4.1. For analysis purposes our SEDs will comprise contributions from four main luminosity sources. Firstly, the accretion luminosity (L_{acc}) and the intrinsic stellar luminosity (L_*), will effectively be combined and provide flux at the shorter wavelength section of the SED. For our parameter space the temperature of the photospheres has a range of 3000 K$< T_{eff} <$1600 K, this will comprise flux contributions peaking in the range, 0.97 to 1.8 μm ($\lambda_{peak} \propto \frac{1}{T_{acc}}$). The accretion spot temperatures, for typical accretors, will range from 340$> T_{acc} >$9400 K, emitting in the range 0.3 to 8.5 μm. For the extreme accretors temperatures which can reach as high as 53 000 K, provide flux to 0.05 μm. The second pair of luminosity sources are from constituent parts of the circumstellar disc. The inner edge, (L_{wall}), at temperatures of 370 to 1500 K, or flux contributions from 1.85 to 7.7 μm (nominally 2 to 3 μm Dullemond et al. 2001), and the outer disc (L_{disc}), at temperatures of 300 K or less contributing flux longward of 10 μm. As discussed in Section 2.2.3 the TORUS radiative transfer code tags the photons before they reach the simulated observer in one of four ways, stellar and thermal, either direct or scattered. These components allow us to analyse the contributions from the main flux contributors discussed, i.e. L_{acc} and L_* equals stellar scattered or direct, with thermal emission comprising L_{wall} and L_{disc}. Figure 12 shows a typically accreting BDD system with the component photon contributions highlighted, with $M_* = 0.04 M_\odot$ at 1 Myr with an areal coverage of 10%, accretion rate of log $\dot{M}=-10$ and rotation period of 0.5 days. The solid black line is the total simulated SED, with the stellar photons shown as blue lines and the thermal as red. The scattered and direct contributions are then shown as dashed and solid lines respectively. The horizontal and vertical dotted lines then show the approximate ranges of the flux contributions from the (from left to right), L_{acc} (blue), L_* (black), L_{wall} (red) and L_{disc} (black). The vertical dashed lines at the bottom of Figure 12 show the approximate ranges of the V, I, J, and K photometric bands we have adopted.

Figure 12 shows that the photosphere and accretion luminosities dominate the SED at wavelengths shortward of 1 μm. After this, for this model, the SED is dominated by contributions from the disc, at shorter wavelengths, the inner edge and then at larger wavelengths the outer disc. As
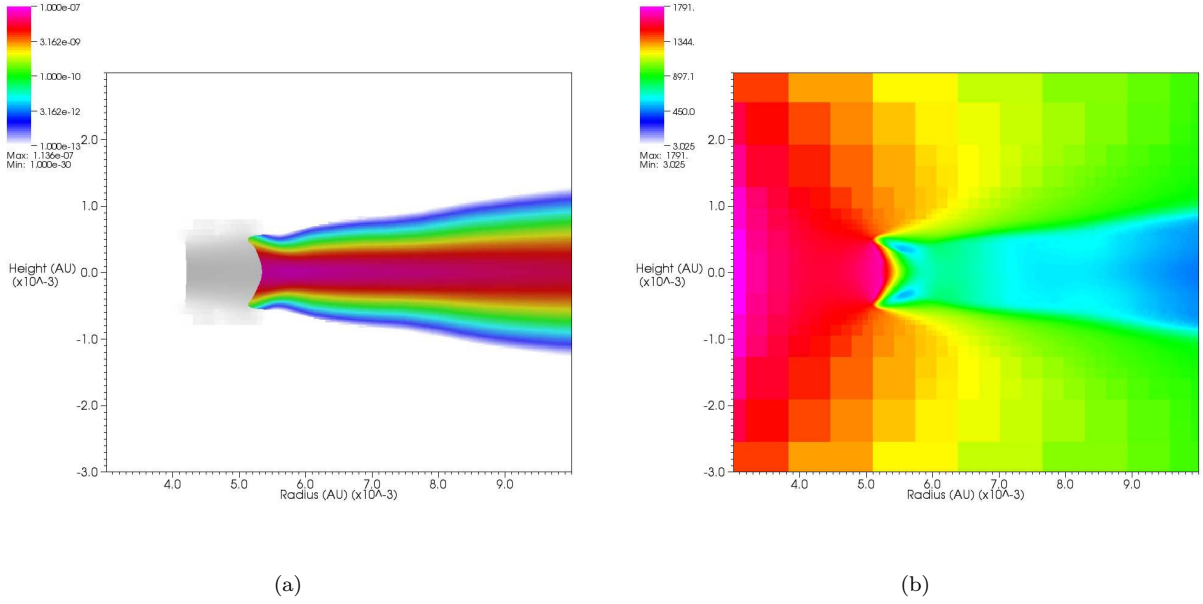
(a)   (b)

Figure 7. Figure showing final density $(\log(\rho))$ where dust is present (colour scale) as the *left panel* and temperature, *right panel*, for a system with no dust sublimation. System parameters are: $M_*=0.04M_\odot$, Age=1 Myrs and areal coverage=10%, τ=5 days and accretion rate $\log \dot{M}= -12$.
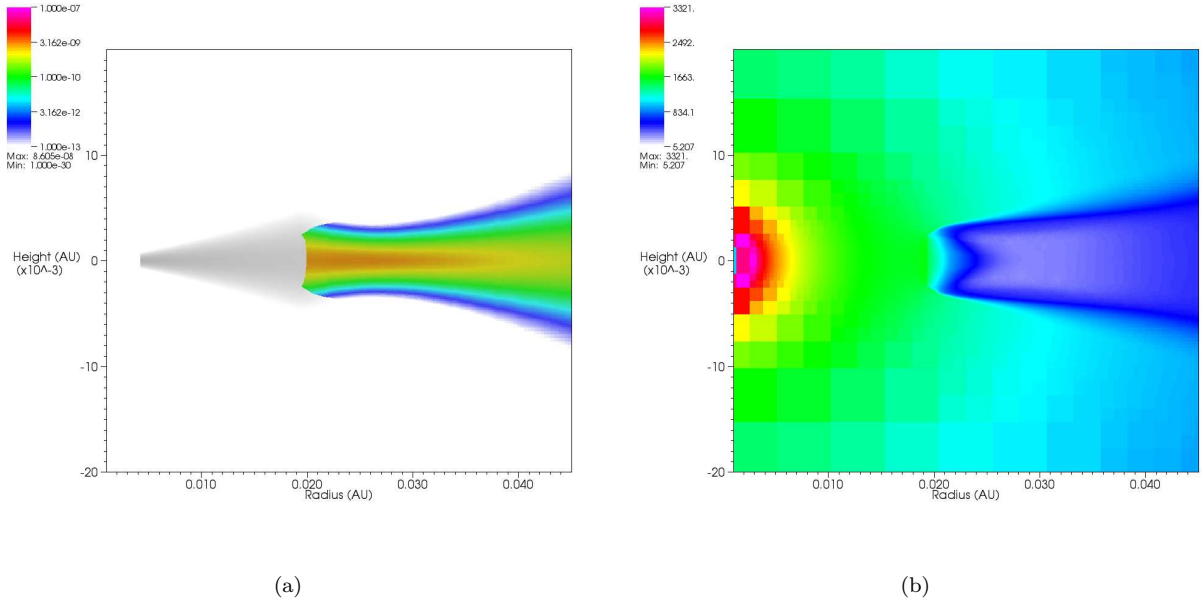

(a)   (b)

Figure 8. Figure showing both the initial (grey scale) and final density $(\log(\rho))$ where dust is present (colour scale) as the *left panel* and temperature, *right panel*, for a system with no dust sublimation. System parameters are: $M_*=0.04M_\odot$, Age=1 Myrs and areal coverage=10%, τ=0.5 days and accretion rate $\log \dot{M}=-12$.

shown in Figure 12 the intrinsic stellar photosphere and accretion luminosities overlap, in terms of peak wavelength of emission. This overlap essentially means that the combined stellar flux $(L_* + L_{\rm acc})$ will eventually become dominated by the accretion flux, as one increases the accretion rate. With the features of the intrinsic stellar photosphere or at-

mosphere eventually lost or swamped by the accretion flux. This will lead to difficulties in using spectral features to identify BDD systems for wavelengths shorter than 1 μm, and, of course, for wavelengths longer than this the SED becomes dominated by disc emission. Therefore, once the SED of a BDD system, at shorter wavelengths, becomes dominated
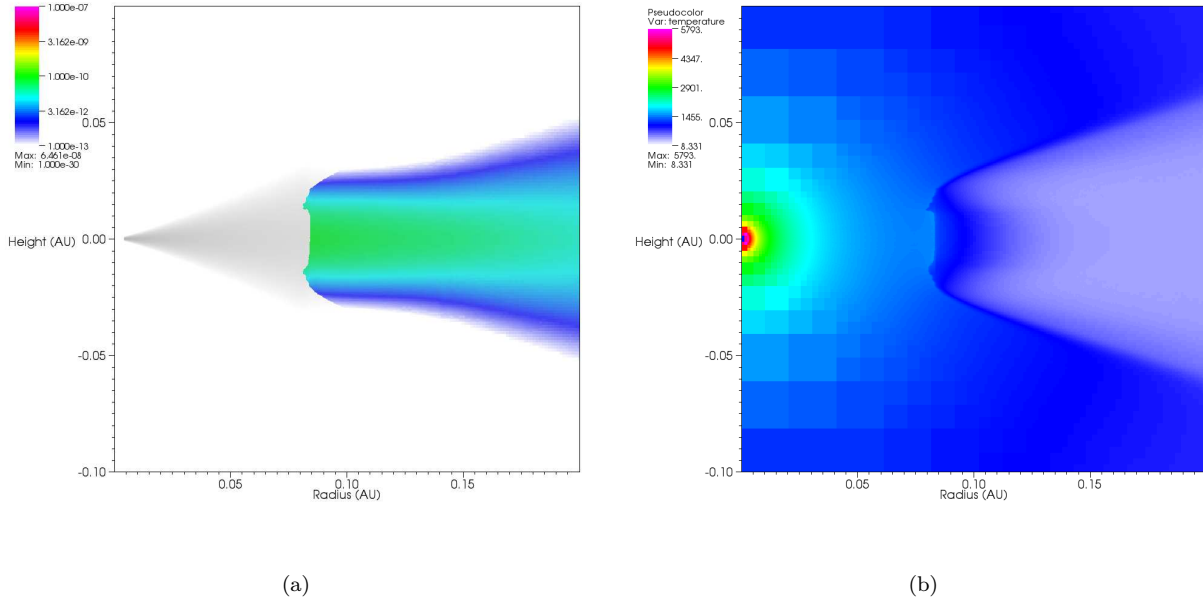
(a)

(b)

Figure 9. Figure showing both the initial (grey scale) and final density ($\log(\rho)$) where dust is present (colour scale) as the *left panel* and temperature, *right panel*, for a system with no dust sublimation. System parameters are: M_*=0.04$M_\odot$, Age=1 Myrs and areal coverage=10%, τ=0.5 days and accretion rate $\log \dot{M}= -9$.

(a)

(b)

Figure 10. Figure showing both the initial (grey scale) and final density ($\log(\rho)$) where dust is present (colour scale) as the *left panel* and temperature, *right panel*, for a system with no dust sublimation. System parameters are: M_*=0.04$M_\odot$, Age=1 Myrs and areal coverage=10%, τ=0.5 days and accretion rate $\log \dot{M}= -7$.

by accretion luminosity spectral classification of these systems (or at least their central stars) will become unreliable. As discussed in Section 4.1.2 observations of the inner edge location separate the BDD systems into two groups, the typical accretors ($\dot{M} \leqslant$-9 $\log(\frac{\dot{M}}{M_\odot} yr^{-1})$) and extreme accretors ($\dot{M} > -9$). This division between typical and extreme ac-

cretors is based on observational results (see Section 3.5) as well as consequence of sublimation. The typical accretors show limited sublimation at the disc inner edge leading to a weak correlation in inner edge temperature with edge radius. Whereas, for the extreme accretors the inner edge is significantly eroded and the dust sublimation tempera-

(a)

(b)

Figure 11. Figure showing both the initial (grey scale) and final density ($\log(\rho)$) where dust is present (colour scale) as the *left panel* and temperature, *right panel*, for a system with no dust sublimation. System parameters are: M_*=0.04$M_\odot$, Age=1 Myrs and areal coverage=10%, τ=0.5 days and accretion rate $\log \dot{M}= -6$.

ture reached, which can not be exceeded. This effectively means that the inner edge temperature is weakly correlated with temperature (with a different characteristic slope to the typical accretors), as the dust sublimation temperature is density dependent, which is in turn dependent on radial position (see Figures 5 and 6).

4.2.1 Accretion dominance

Figure 13 shows the affect of increasing the accretion blackbody flux (for increasing accretion rates) for a BD star, M =0.04$M_\odot$, at 1 Myr. Whilst the photons originating from the star (both from L_* and $L_{\rm acc}$) will be tagged as stellar by TORUS we can separate these flux contributions simply by observing the naked star system. The panels in Figure 13 show the flux from a naked system, with no treatment of the disc. This enables us to view the effect of increasing accretion rate on the photospheric flux in isolation. The accretion rates included in all panels are $\log \dot{M}= -8$, -9 and -12 (blue, black and red lines respectively). The *bottom panels* show the systems with a rotation period of 5 days and *top panels* for those with a rotation period of 0.5 days. Given our assumption that accretion occurs from the co-rotation radius, decreasing the rotational period moves this accretion radius closer to the star, $R_{\rm inner} \propto \tau^{2/3}$ (see Equation 3). As the accretion radius moves father from the star the potential energy released by the accreted material is reduced. This effect can be seen when comparing the *top* and *bottom panels*, although the effect is marginal for all but the highest displayed accretion rates. The *left panels* show accretion streams with an areal coverage of 10% and the *left panels* 1%. As the areal coverage reduces the effective temperature of the accretion hot spot increases, resulting in an increase in accretion flux, and resulting shift to bluer wave-
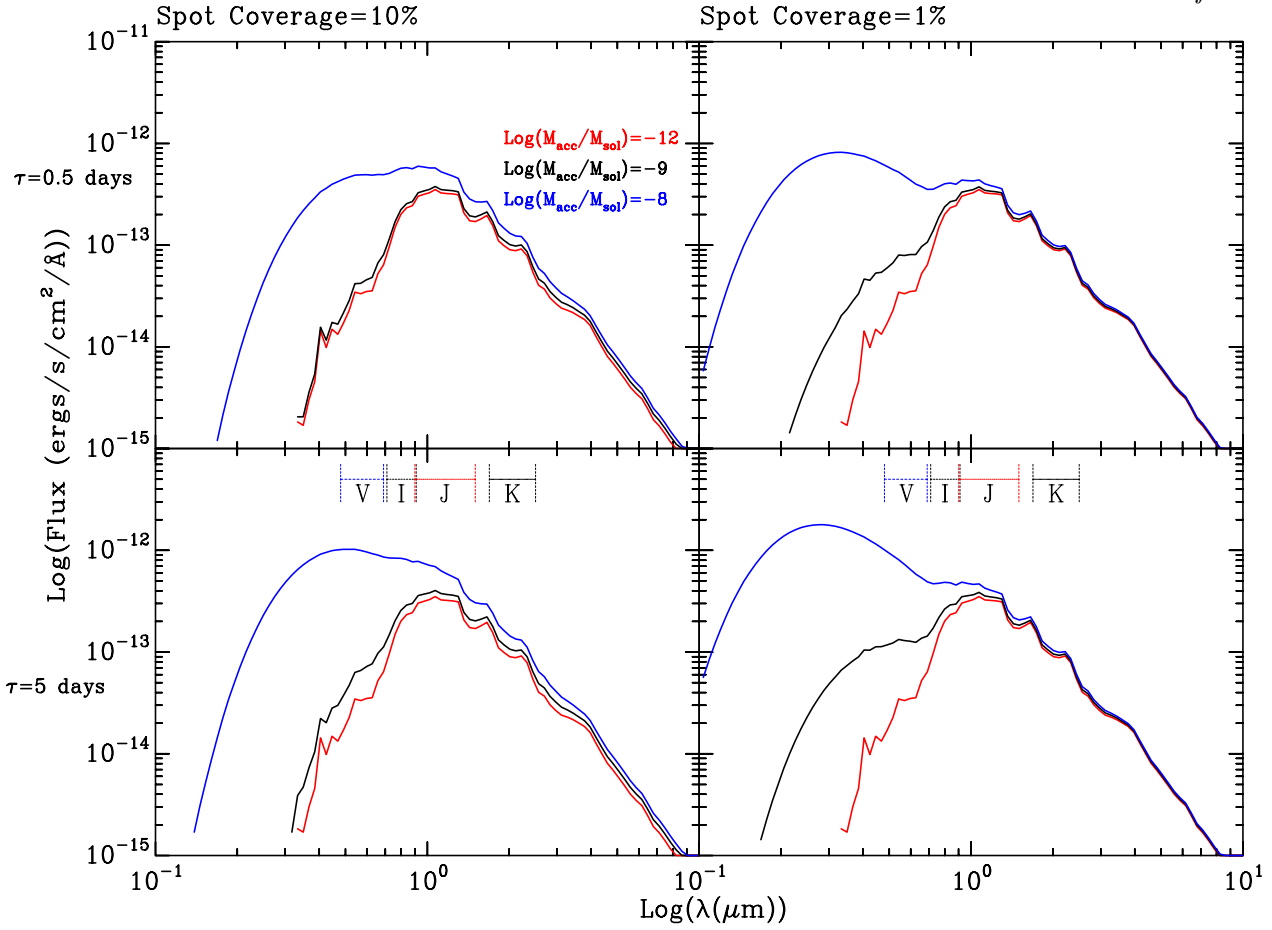
lengths of the peak flux. This can be seen clearly by comparing the *left* and *right panels* of Figure 13. Perhaps the most important, albeit qualitative, result shown is Figure 13 is an insight into the accretion rate at which the accretion blackbody flux dominates over the photospheric flux. Figure 13 shows that as the accretion rate raises above $\log \dot{M}= -9$ for systems with 1 or 10% areal coverage, the accretion flux dominates the emergent SED at both periods. Therefore for reasonable coverages (1-10%) and rotational periods (0.5-5 days) the photospheric flux is effectively swamped by accretion flux for accretion rates $\log \dot{M}> -9$. This suggests that accreting BD systems with accretion rates as low as $\log \dot{M}= -9$ could be difficult to identify from SEDs as BD stars, and may well be classified as higher mass stars.

As is well known the shorter wavelength component of the SED for extreme accretors is dominated by the accretion luminosity. For the typical accretors the intrinsic photospheric emission is important and the flux levels of this component are dependent on the stellar parameters of mass and age, through evolution of the stellar radius and temperature, as is well understood. In general, the bluer (short wavelength) components of the SEDs are therefore controlled by the stellar input parameters (mass and age) and the accretion input parameters (accretion rate and areal coverage, and to a lesser extent rotation rate).

4.2.2 Flaring and obscuration

As shown in Figures 2 and 3 and discussed in Section 4.1.1 BDD systems under vertical hydrostatic equilibrium have highly flared discs. As discussed in Walker et al. (2004) this increased flaring (when compared to CTTS stars) leads to occulltation at the star at lower inclination angles and, therefore, significant changes to the SED. Increases in the
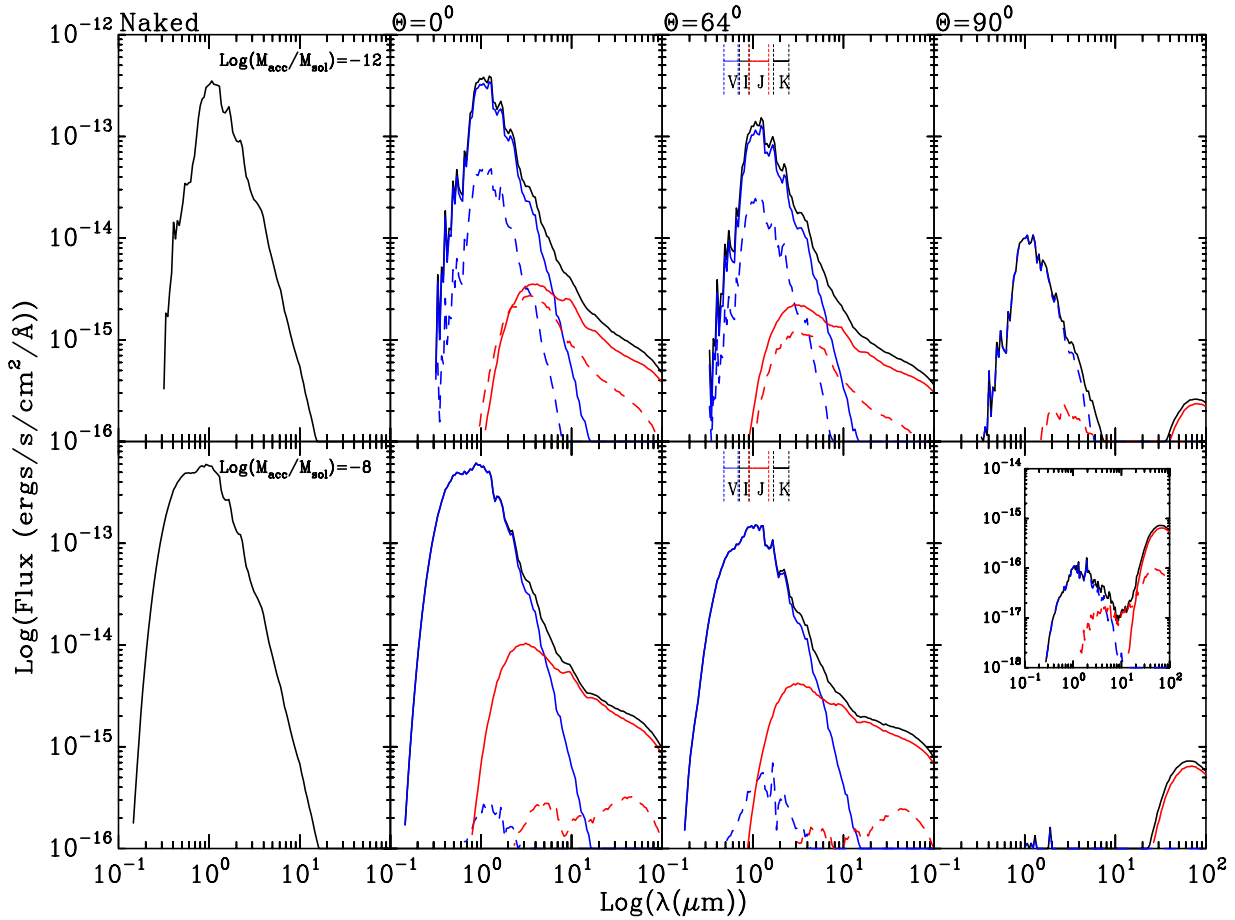
Figure 13. Figure showing the photospheric flux ($\log(\text{ergs}/s/cm^2/\text{Å})$) against λ ($\log(\mu m)$) of a Brown Dwarf with $M = 0.04 M_{\odot}$, at 1 Myr. No disc is included, but blackbody fluxes from an accretion stream at the rates of $\log \dot{M} = -8$, -9 and -12 are shown as blue, black and red lines respectively. The *bottom panels* show accretion for a star rotating at 5 days, with the *top panels* showing that of 0.5 days. The *left panels* systems with an areal coverage of 10% and the *right panels* has 1%. The vertical and horizontal dashed lines (in the *lower panels*) denote the approximate sensitivity ranges of our chosen V, I, J and K filters.
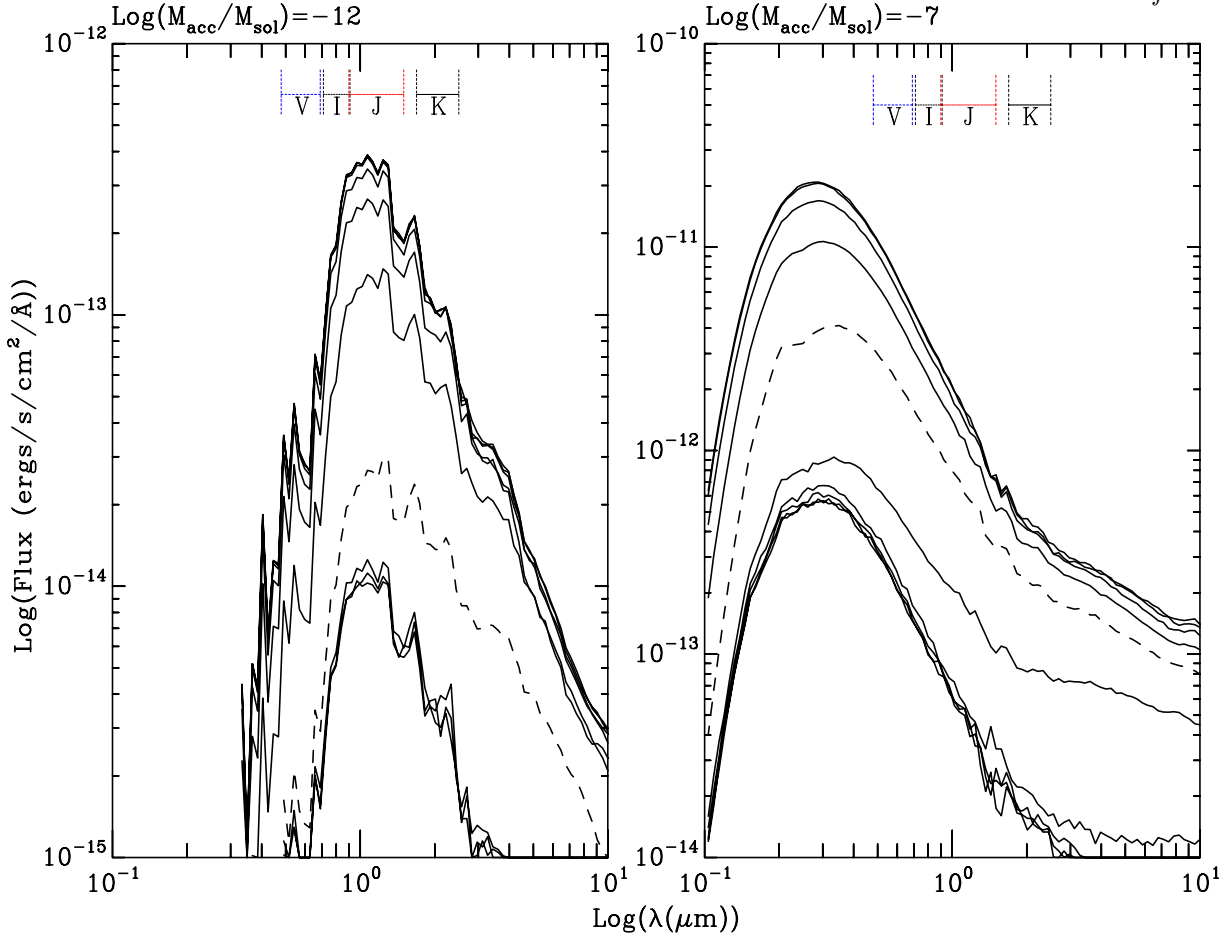
inclination angle, for these systems, quickly lead a significant proportion of the stellar flux being intercepted, and reprocessed, by the highly flared disc. This reprocessing will lead to a change in the flux levels at the shorter, bluer, wavelengths as more stellar flux is reprocessed and intercepted by the disc. It will also lead to significant changes in the flux reaching the observer from the inner and outer regions of the disc.

Figure 14 shows the SEDs for a range of inclinations for BDD systems with two accretion rates. The BDD system has a central stellar mass of $0.04 M_{\odot}$, an age of 1Myr, a rotation period of 0.5 days and an areal coverage of the accretion stream of 10%. The *top panels* show the SEDs for a star with an accretion rate of $\log \dot{M} = -12$ (the lowest in our typical accretion range). The *bottom panels* then show SEDs for systems with an accretion rate of $\log \dot{M} = -8$ (classed as an extreme accretor). From left to right the *panels* then show the naked stellar flux then the fluxes from BDD systems seen at inclination angles of $0°$, $64°$ and $90°$, or face-on, the approximate expectation value of inclination and edge-on. For each of the *second* to the *fourth panels* the flux components are then shown as in Figure 12, i.e. the total SED shown as a black line, then stellar light shown in blue

and thermal in red, with direct shown as bold and scattered as dashed lines. The inset graph in the *bottom right* panel of Figure 14 simply shows a lower flux scale, as the flux levels have fallen to the lowest shown division in the main Figure.

Figure 14 shows, by comparing the *top panels* that as a disc is added to the system and the inclination of the BDD system is increased more stellar (and accretion flux) is reprocessed by the disc, for a negligibly accreting system. As one moves from inclinations of 0 to $64°$ the stellar flux has reduced as has the thermal component. At edge-on inclinations the system is only visible through scattered light, and some (slight) thermal emission from the outer disc at wavelengths $\lambda > 30\,\mu m$ (indicative of temperatures of ~100 K. Increasing the accretion rate from -12 to -8 $\log(\frac{\dot{M}}{M_{\odot}}yr^{-1})$ leads to a significant increase in the naked stellar flux (compare *top left* and *bottom left panels*). As we add a disc and increase the viewing inclination for the extreme accreting system (*bottom panels*), we also lose stellar flux. In the extreme accretor case however the fall in flux contribution to the total SED from the photosphere (and accretion) is much more significant. Indeed, at edge-on inclinations the system becomes only visible in the thermal (~100 K) disc regime, with the scattered light significantly reduced.

Figure 14. Figure showing SEDs of a system with a central stellar mass of $0.04 M_\odot$, an age of 1Myr, a rotation period of 0.5 days and an areal coverage of the accretion stream of 10%. The *panels*, both *top* and *bottom*, (from left to right) show the naked stellar flux (*first panel*), then constituent fluxes for SEDs at inclination angles of $0°$, $64°$ and $90°$. The *second* to *fourth panels* on each line then show the total flux as a black line, with the component fluxes presented as explained Figure 12. The *top panels* are for systems with an accretion rate of -12 $\log(\frac{\dot{M}}{M_\odot} yr^{-1})$ and the *lower panels* are for an accretion rate of -8 $\log(\frac{\dot{M}}{M_\odot} yr^{-1})$. The *bottom right panel* inset Figure shows an enlargement of the lower flux levels of this SED. The vertical and horizontal dashed lines (in the *third panels* across) denote the approximate sensitivity ranges of our chosen V, I, J and K filters.

As shown in Section 4.1, and more specifically, Figures 2 and 3 as one increases the accretion rate for BDD systems, in general, the outer disc structure increases in vertical height. Effectively, the greater flux levels increase the temperature of the outer disc and the condition of vertical hydrostatic equilibrium leads to a vertical expansion. This vertical expansion leads to a significant change in the angle at which photons emitted from the stellar photosphere are intercepted by the outer disc. This is an extension of the effected found in Walker et al. (2004), where it was found that this effect alone can shift the SED, and therefore colours and magnitudes, of inclined BDD systems to those indicative of higher mass CTTS. The actual changes in flux are complicated by dust sublimation and shape changes of the inner edge (discussed later). As the inclination of the BDD system is increased we see the total flux drop significantly once we exceed the opening angle of the BDD system. This opening angle will decrease with vertical scaleheight of the outer disc. Figure 15 shows the total SEDs for the BDD system of Figures 2 and 3, with the corresponding accretion rates as *left* and *right panels* respectively. The solid lines of *both panels* of

Figure 15 show the total SED for each of our ten simulated inclinations, namely, 0, 27, 39, 48, 56, 64, 71, 77, 84 and 90° (with the flux decreasing with increasing inclination). The dashed line then highlights the inclination at which the flux observed drops significantly, at 71 and 56° for the accretion rates of -12 and -7 (or *left* and *right panels*), respectively. Whilst this effect is probably artificially enhanced for such extreme accretion rates it is illustrative of the general trend, notwithstanding complications from inner edge shape.

4.2.3 Inner Edge Shape

As discussed in Section 4.1 the addition of dust sublimation leads to a change in the shape of the inner edge, where the temperature is sufficient. Figures 7 to 11 show a range in inner edge shapes, from flat walls through concave to convex curves, caused by the radial density profile of the disc and the dependence of the sublimation temperature on density. This change in shape, as noted by Tannirkulam et al. (2007), will lead to changes in the characteristics of the SED, or derived IR excess, with inclination angle (Tannirkulam et al.

Figure 15. Figure of total SED flux reaching the observer for viewing angles of 0, 27, 39, 48, 56, 64, 71, 77, 84 & 90°. SEDs shown are for systems shown in Figures 2 and 3, as the *left* and *right panels* respectively. In both panels the dashed line highlights the angle at which a significant fall in flux reaching the observer occurs. The values of inclination at which the fall in flux occurs are 71° and 56° for the accretion rates of -12 and -7 $\log(\frac{\dot{M}}{M_\odot}yr^{-1})$, *left* and *right panels* respectively. The vertical and horizontal dashed lines denote the approximate sensitivity ranges of our chosen V, I, J and K filters.

2007). For concave and vertical walls the inner edge is visible over a smaller range of viewing angles than for a convex inner edge.

Figures 16 and 17 show the thermal direct radiation, originating from the disc, as a function of inclination for the two groups of accretors, typical and extreme respectively. The models included in Figure 16 as the *left* and *right panels* are those shown in Figures 8 and 9 respectively. Whereas, the models included in Figure 17 as the *left* and *right panels* are those shown in Figures 10 and 11 respectively. For each *panel* of Figures 16 and 17 the thermal direct flux is plotted as a solid black line at each modeled inclination, namely, 0, 27, 39, 48, 56, 64, 71, 77, 84 & 90°. The dashed line in each case shows where a significant fall in the flux reaching the observer from direct thermal emission from the disc is apparent.

For typically accreting systems, where little or no dust sublimation has occurred the inner edge remains either a vertical or slightly concave wall, as shown in Figures 8 and 9. For these systems flux reaching an observer from direct thermal emission, i.e. from, in the main, the disc inner edge, falls rapidly with increasing viewing angle, after the maximum opening angle is achieved. This is shown in Figure

16 where at the viewing angle of 77° the flux shown falls significantly, for both accretion rates. This opening angle is larger than found for the slower rotating, counter parts, as shown by Figure 15, where a transition in occultation occurs at 71°. For the case shown in Figure 16 the system has the shorter rotation period, leading to a larger opening angle, as the flux from the central star does not reach the outer disc, and subsequently flare it. Figure 16 shows that after an angle of 77° the flux from the inner edge falls to zero. The systems displayed in Figure 16 have inner edge temperatures of 1400 K, meaning their flux emission peaks at a wavelength of 2 μm. The flux observed at the expected peak wavelength falls to zero at inclinations of 77°, indicative of a vertical wall being obscured by the outer disc, before the limit of the opening angle is reached.

Figure 18 shows the full SEDs and the components (as tagged by TORUS), for the models displayed in Figures 8 and 10 and the *left panels* of Figures 16 and 17. The *top panels* show the SEDs for an accretion rate of -12 $\log(\frac{\dot{M}}{M_\odot}yr^{-1})$ (model from Figure 8) for inclinations of 64, 71 and 77°, moving from the *leftmost* to *far right panel*. The same inclinations are shown in the *bottom panels*, which show the SEDs, and components, for the model with an accretion rate
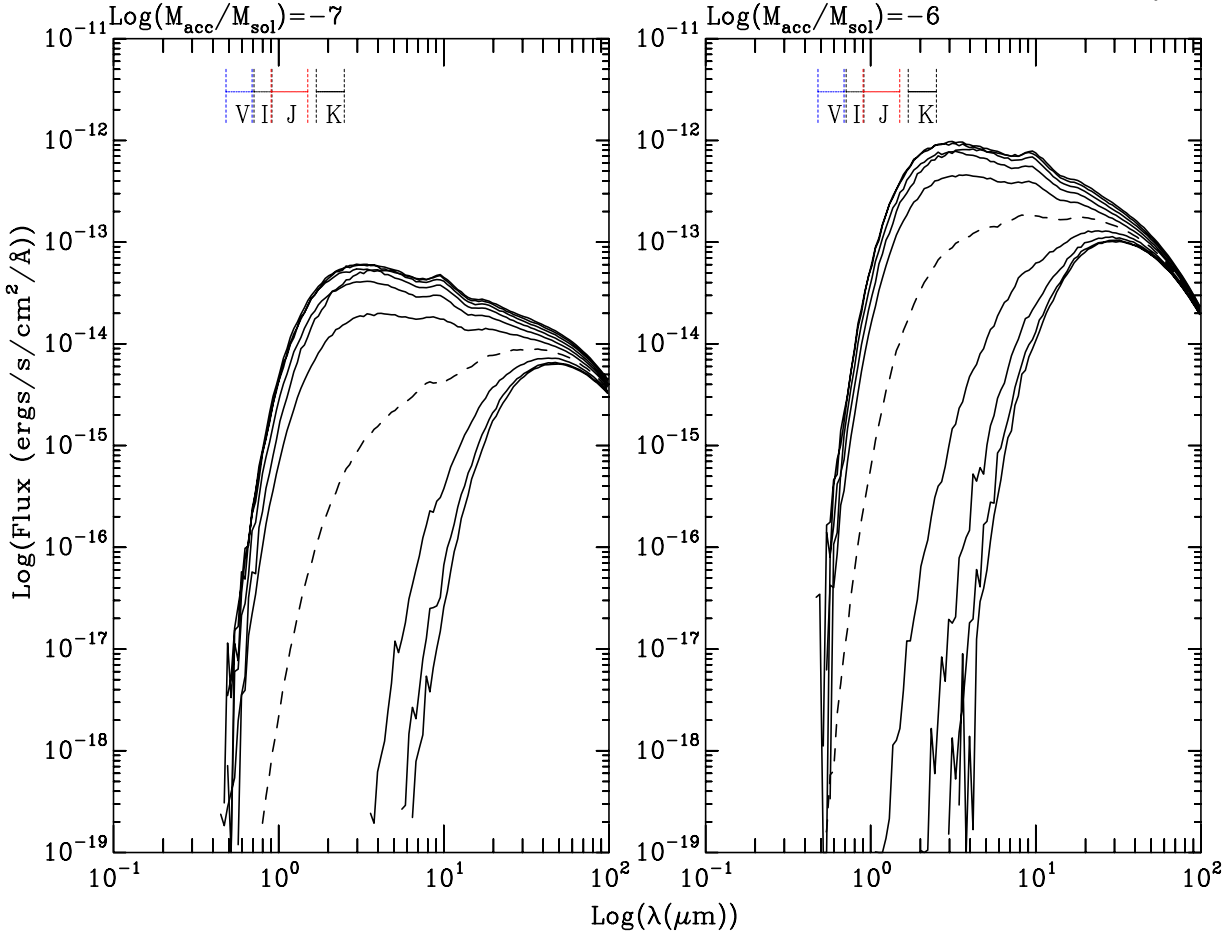
Figure 16. Figure showing thermal direct flux reaching the observer at inclination angles of 0, 27, 39, 48, 56, 64, 71, 77, 84 & 90°, for typical accretors. The *left panel* shows the flux from the model shown in Section 4.1, Figure 8. The *right panel* shows the flux from the model shown as Figure 9 in Section 4.1. In both panels the dashed line highlights the angle at which a significant fall in flux from direct thermal emission is observed. The values of inclination at which the fall in flux occurs are 77° for *both panels* and therefore accretion rates. The vertical and horizontal dashed lines denote the approximate sensitivity ranges of our chosen V, I, J and K filters.

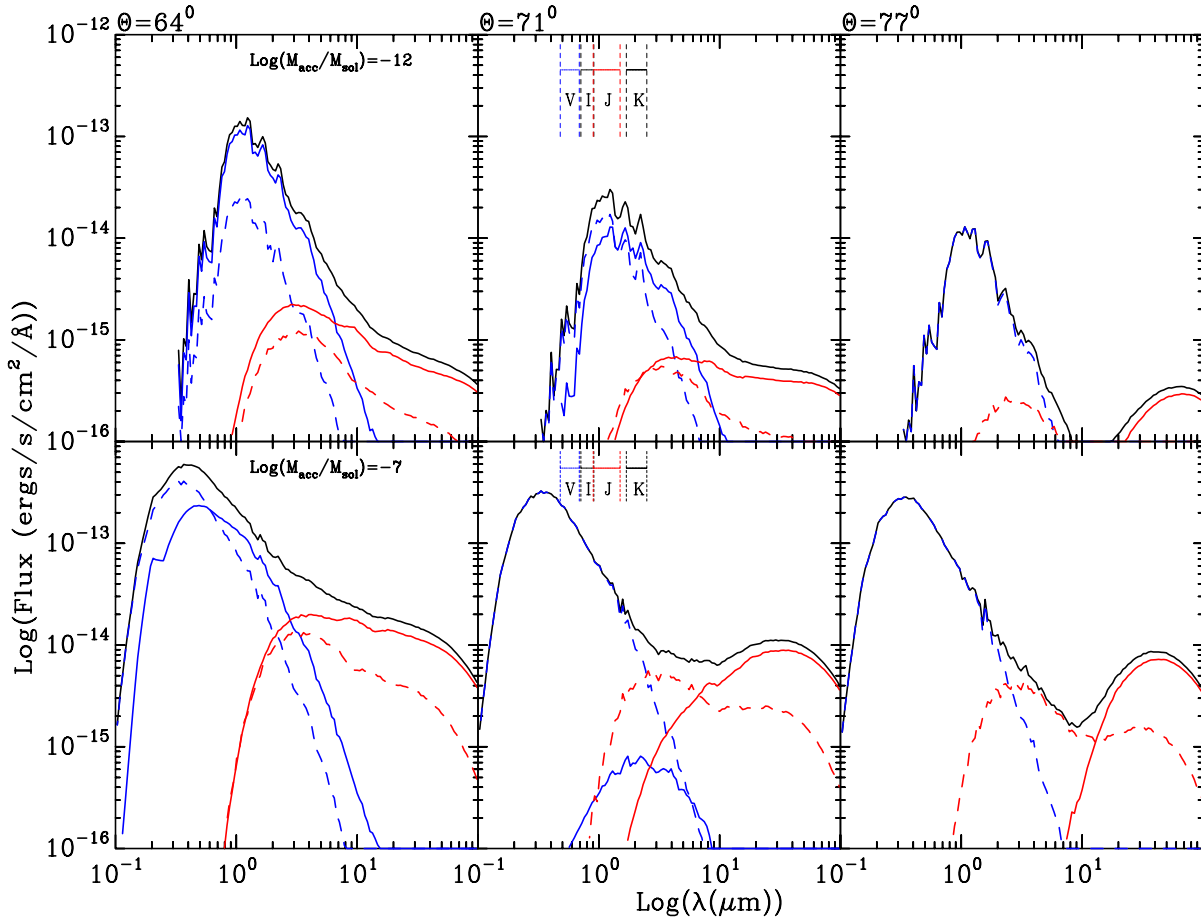of -7 $\log(\frac{\dot{M}}{M_{\odot}} yr^{-1})$, displayed in Figure 10. As discussed in Section 4.1, the model with the higher accretion rate has a a much larger, in scaleheight, and convex inner boundary. The lower accretion rate model has a vertical inner wall, close to the star. The analysis of Figures 16 and 17 show that the flux from the inner wall should fall dramatically at different limiting inclinations for either accretion rate.

Figure 18 shows that for negligible accretion rates (*top panels*), where the inner edge is a vertical wall, the total flux falls rapidly after exceeding a viewing angle of 71°. After an inclination of 71°, the negligibly accreting system is dominated by scattered light from the central star. The system accreting at -7 $\log(\frac{\dot{M}}{M_{\odot}} yr^{-1})$, however, maintains high flux levels, and thermal contributions to the SED, for inclination angles above 71°, particularly between 1 and 3 μm. Essentially, as shown by comparing Figures 8 and 10, with increasing flux and subsequent dust sublimation the inner edge has grown vertically and become convex. As shown previously by Tannirkulam et al. (2007), a vertical (or concave) inner edge will have strong dependence on inclination angel as the inner edge is obscured at lower inclinations. For the larger convex wall, the SEDs shown in 18 show that the resulting flux is less dependent on inclination angle.

Once accretion rates reach extreme levels the inner edge is sublimated far from the central star. For these systems the resulting inner edge is both larger, in terms of scaleheight, and convex. Figure 17 shows that the flux falls dramatically at an occultation angle of 71 and 64° for accretion rates of -7 and -6 $\log(\frac{\dot{M}}{M_{\odot}} yr^{-1})$, respectively (*left* and *right panels*, respectively). For the accretion rate of -7 $\log(\frac{\dot{M}}{M_{\odot}} yr^{-1})$ this is indicative of a larger opening angle (71°) for the shorter period object, when compared to the more slowly rotating equivalent (56°, from Figure 15, *right panel*). Additionally, Figure 18 shows that the total SED, has a strong thermal component and is only weakly dependent on inclination angle, between 1 and 3 μm . This increase in opening angle with increase in rotation rate is again due to more flux being intercepted by a larger and closer inner wall. This interception of flux by the inner edge leads to a cooler and less vertically extended outer disc in the shorter period objects when compared to the slower rotating systems. Figures 17 and 18 also show that, contrary to the typical accretors, the flux from the inner edge does not fall off as quickly with inclination angle after occultation. The inner edge temperatures are 1300 and 1200 K for the accretion rates of -7 (*left panel*) and -6

Figure 17. Figure showing thermal direct flux reaching the observer at inclination angles of 0, 27, 39, 48, 56, 64, 71, 77, 84 & 90°, for extreme accretors. The *left panel* shows the flux from the model shown in Section 4.1, Figure 10. The *right panel* shows the flux from the model shown as Figure 11 in Section 4.1. In both panels the dashed line highlights the angle at which a significant fall in flux from direct thermal emission is observed. The values of inclination at which the fall in flux occurs are 71° and 64° for the *left* and *right panels* respectively. The vertical and horizontal dashed lines (in the *lower panels*) denote the approximate sensitivity ranges of our chosen V, I, J and K filters.
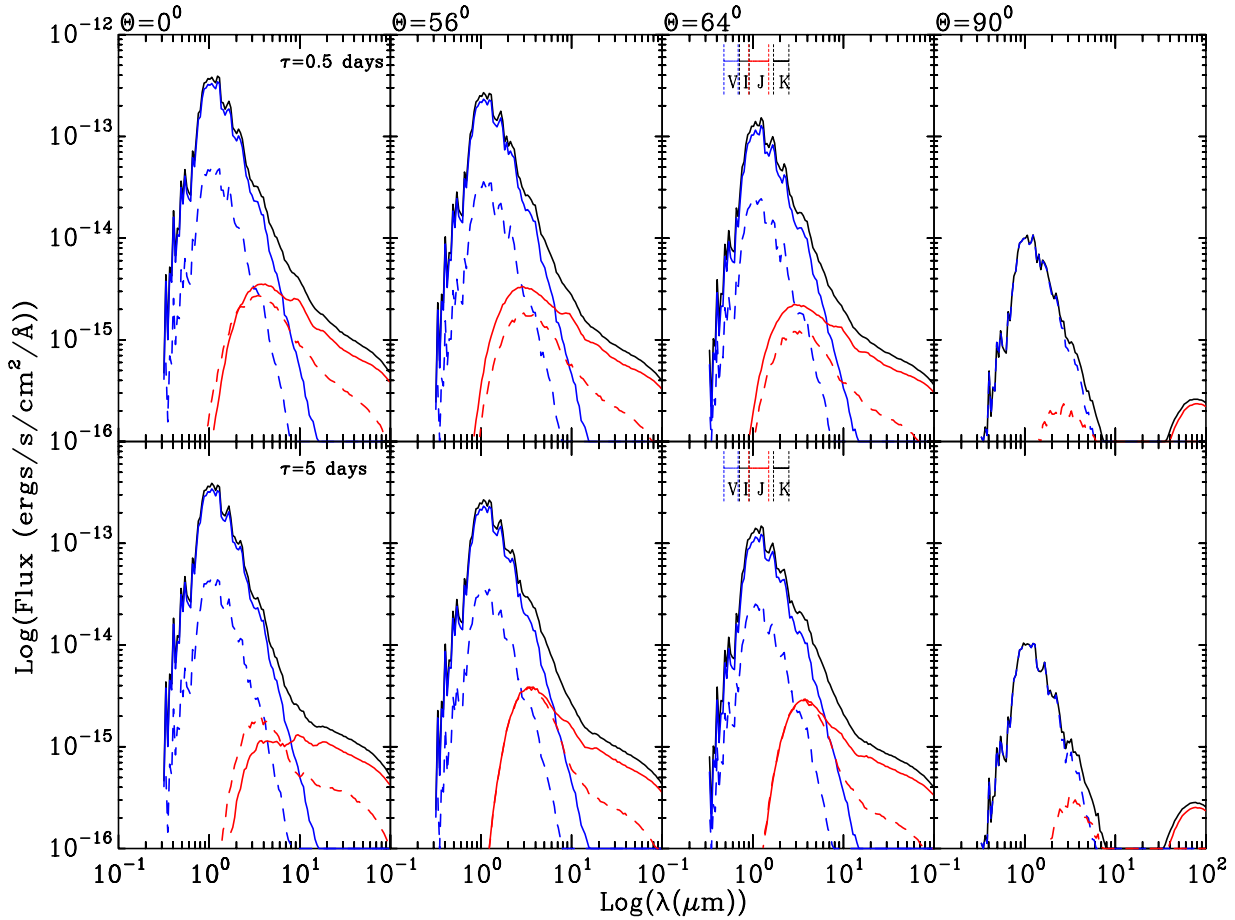
(*right panel*) $\log(\frac{\dot{M}}{M_\odot} yr^{-1})$ respectively. This leads to peak emission at 2.2 to 2.4 μm. Figures 17 and 18 shows that even for inclinations above the occulation or opening angle of the disc flux from the inner edge persists. This is indicative of a large and convex inner edge, as is observed in Figures 10 and 11. Once again these extreme accretion rates probably over accentuate the result but help illuminate the consequences of changes in the disc structure.

Therefore, the longer (in wavelength) component of the final SED is dominated by the disc inner edge (L_{wall}), temperature and shape and the outer disc scaleheight (L_{disc}). The shape and location of the inner disc walls are controlled, primarily, by the stellar rotation rate (and stellar radius) and accretion rate (and stellar flux). Given that the stellar flux and radius decrease as the pre-MS star ages (or decreases in mass) the flux levels and the position of the inner edge are also weakly affected by the age of the central star.

As shown in Figure 6 the location of the inner edge and the corresponding temperature are correlated (differently) for typical and extreme accretors. This correlation is dominated by the dust sublimation temperature for the extreme accretors, and therefore the radial density profile.

However, for the typical accretors the correlation between temperature and inner radius retains some dependence on the co-rotation radius (temperature is correlated with rotation period). This is as the sublimation temperature is not reached for the longer period models. Therefore, one might expect the resulting SEDs for typical accretors to show a correlation in shape, between 2 and 3 μm, caused by the inner wall temperature changes, in turn caused by changes in the rotation period. Figures 19 and 20 show the SEDs (and constituent parts as explained in Figures 12) for a BDD model at the two rotation periods. The model has a mass of 0.04$M_\odot$ and an age of 1 Myr, with accretion rates of -12 and -9 $\log(\frac{\dot{M}}{M_\odot} yr^{-1})$ in Figures 19 and 20 respectively, both at an areal coverage of 10%. The *top panels* show the SEDs for a rotation period of 0.5 days, and the *bottom panels* the SEDs for a rotation period of 5 days. The *first*, *second*, *third* and *fourth panels* then show inclination angles of 0, 56, 64 and 90° respectively.

Figures 19 and 20 show that for these BDD systems with typical accretion rates, the changes in SED with rotation period are small, apart from perhaps the face-on configuration. The systems in the *top* and *bottom panels* of Figures

Figure 18. Figure showing SEDs of a system with a central stellar mass of $0.04 M_\odot$, an age of 1Myr, a rotation period of 0.5 days and an areal coverage of the accretion stream of 10%. The *panels*, both *top* and *bottom*, (from left to right) show the constituent fluxes for SEDs at inclination angles of 64°, 71° and 77°. The total flux is shown as a black line, with the component fluxes presented as explained Figure 12. The *top panels* are for systems with an accretion rate of -12 $\log(\frac{\dot{M}}{M_\odot} yr^{-1})$ and the *lower panels* are for an accretion rate of -7 $\log(\frac{\dot{M}}{M_\odot} yr^{-1})$. The SEDs from the *top* and *bottom panels* are derived from the models presented in Figures 8 and 10, respectively. The vertical and horizontal dashed lines (in the *second panels* across) denote the approximate sensitivity ranges of our chosen V, I, J and K filters.
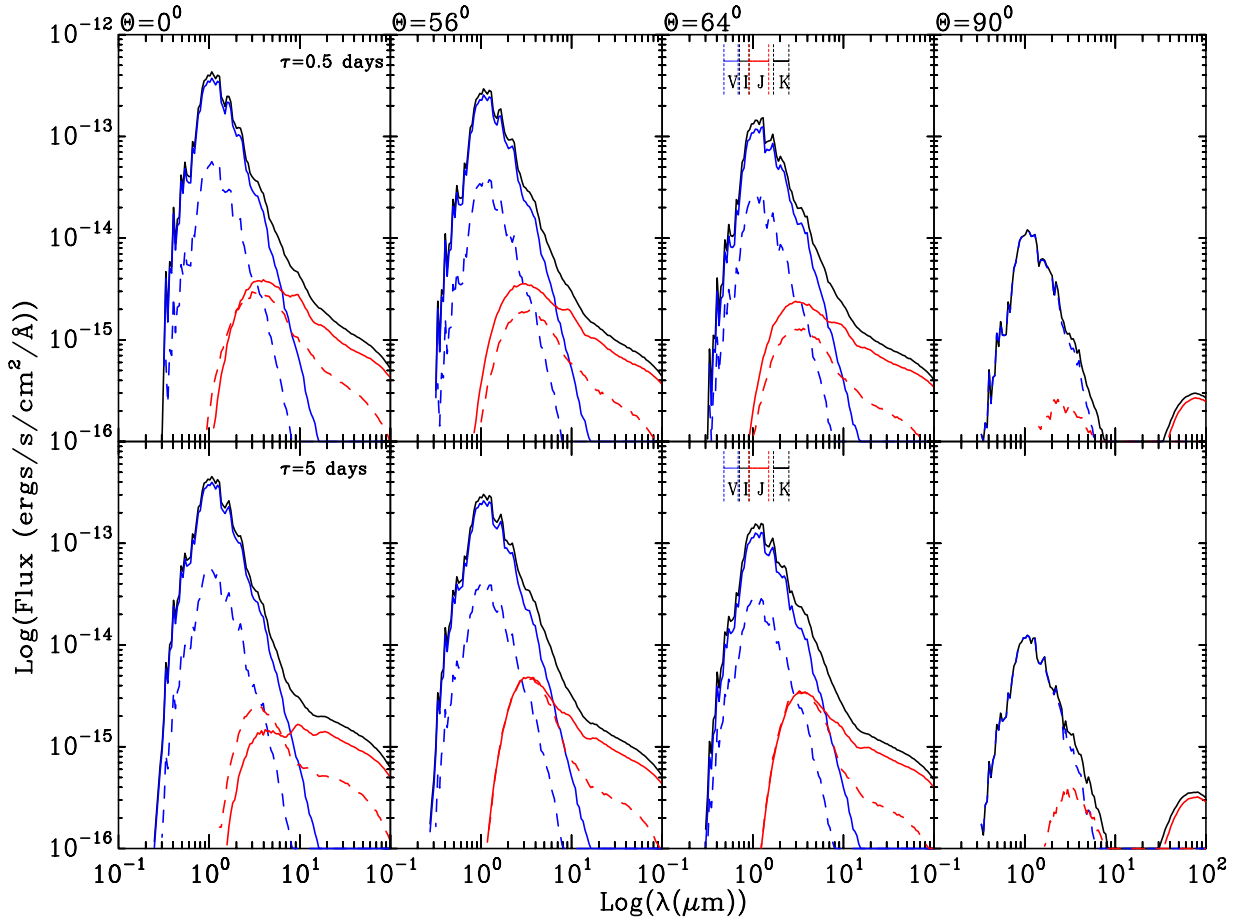
19 and 20 have inner edge temperatures of 1470 & 900 K, and 1460 & 940 K respectively. This leads to different peak emissions for the slower and faster rotating stars, of approximately 2 and 3 μm. However, as is shown by Figures 19 and 20 very little resulting change is apparent in any of the SEDs apart from the face-on configuration. Essentially, any change in the SED shape caused by changing emission at the inner disc edge is smoothed out by the resulting interactions with the rest of the disc structure. As pre-MS stars age they contract and reduce in luminosity, this will lead to changes in the co-rotation radius and inner edge temperature. The models in Figures 19 and 20 are for an age of 1 Myr. Therefore, changes in the SED could also be more apparent for older systems, with lower stellar luminosities. Figures 21 and 22 show the same system as Figures 19 and 20, i.e. with accretion rates of -12 and -9 $\log(\frac{\dot{M}}{M_\odot} yr^{-1})$ respectively, but for ages of 1 and 10 Myrs. In Figures 21 and 22 only the total SED are shown for the shorter period, a solid black line, and the longer period, as a dashed blue line. The *top panels* show the SEDs for 1 Myr systems and the *bottom panels* the 10 Myr systems. The *first*, *second*, *third*

and *fourth panels* again show the viewing angles of 0, 56, 64 and 90° respectively.

Figures 21 and 22 show that for typical accretors the resulting SEDs do not, in general, change significantly with changing rotation rate. For the face-on configuration (*far left panels*) the SED slope over 2 to 3 μm is marginally different only. Essentially, flux redistribution from the highly flared outer regions of the disc and inner edge shape changes lead to a loss of correlations of SED shape (from 2 to 3 μm)with inner edge temperature. This leads to a loss of any correlation between IR excess and inner edge location as predicted for the, flat, discs of Meyer et al. (1997).

4.2.4   SED summary

The shape of the combined SED, $L_* + L_{acc} + L_{wall} + L_{disc}$, is controlled by the combined stellar flux (intrinsic stellar temperature and luminosity, and accretion stream temperature and luminosity), and the disc characteristics (inner edge location and temperature, and outer disc flaring). The stellar flux and temperature both increase with increasing accretion

Figure 19. Figure showing SEDs of a system with a central stellar mass of $0.04M_\odot$, an age of 1Myr an accretion rate of -12 $\log(\frac{\dot{M}}{M_\odot}yr^{-1})$ with an an areal coverage of 10%. The *panels*, both *top* and *bottom*, (from left to right) show the SEDs and constituent fluxes at inclination angles of $0°$, $56°$, $64°$ and $90°$. The component fluxes are presented as explained Figure 12. The *top panels* are for systems with a rotation period of 0.5 days and the *lower panels* are for a rotation period of 5 days. The vertical and horizontal dashed lines (in the *third panels* across) denote the approximate sensitivity ranges of our chosen V, I, J and K filters.

rates and reducing areal coverages. The stellar flux (at constant temperature) also reduces as a pre-MS star contracts with age (or reduces in mass). Furthermore, the inner disc flux increases as the inner wall becomes hotter, larger and more visible with increasing incident flux. The outer disc component also increases as the outer disc flares. The flaring and temperature of the disc are controlled by the stellar flux and the rotation rate. Finally, and most importantly, the shape of the SED will be dominated by the inclination of the system, especially for extremely flared systems. This results in the observable SED being a major function of the input variables, age (and mass), accretion rate (and areal coverage), rotation period and system inclination.

As we have discussed in this Section and Section 4.1 the underlying disc structures are caused by complicated interplays between the sublimation physics, vertical hydrostatic equilibrium and emission of the disc components. However, several underlying trends have been observed in the physical characteristics of the systems. Most notably the correlation, to different strengths, of the disc inner wall location and its resulting temperature, as found in Meyer et al. (1997). However, Meyer et al. (1997) go on to predict a correlation of IR excess with inner edge location. Given that the

initial inner edge location is dependent (chiefly) on the rotation period one might expect a correlation of rotation rate with IR excess. This has been shown to be unlikely due to complications in the inner edge location due to dust sublimation, and obscuration of the inner disc edge at higher inclination angles. In addition, for large groups of stars there is evidence for a correlation in stellar mass with accretion rates. Although we have shown that the observable SEDs of BDD systems at higher accretion rates are difficult to classify as such, most surveys supporting this relationship use photometric data. Therefore, we must examine whether these problems translate into the broadband photometric magnitudes.

4.3 Photometry

Practically, most parameters for young pre-MS stars are derived from surveys of populations, usually open clusters, using broadband photometry and subsequently constructed colour-magnitude and colour-colour diagrams (CMDs and CoCoDs respectively, hereafter). Therefore, in this Section, we demonstrate the prohibitive effects on the broadband photometry of varying our input parameters. In this Sec-

Figure 20. Figure showing SEDs of a system with a central stellar mass of $0.04 M_\odot$, an age of 1Myr an accretion rate of -9 $\log(\frac{\dot{M}}{M_\odot}yr^{-1})$ with an an areal coverage of 10%. The *panels*, both *top* and *bottom*, (from left to right) show the SEDs and constituent fluxes at inclination angles of $0°$, $56°$, $64°$ and $90°$. The component fluxes are presented as explained Figure 12. The *top panels* are for systems with a rotation period of 0.5 days and the *lower panels* are for a rotation period of 5 days. The vertical and horizontal dashed lines (in the *third panels across*) denote the approximate sensitivity ranges of our chosen V, I, J and K filters.

tion we, in particular, relate the discussed features of disc structures (4.1) and the resulting simulated SEDs (4.2) in terms of the derived photometry, in Section 4.4. Furthermore, we explore the consequences of our model grid on the derivation of the primary parameters of age, mass and disc fractions, from populations, in Section 4.5. This in turn leads to highlighting selection effects with, for instance, the mass to accretion rate relation.

4.4   Effects of Disc Presence and Accretion on Photometry

For the derivation of ages optical CMDs, in particular in *V, V-I*, are most often used, and indeed most suitable. Whereas, IR CMDs, such as a *J, J-K* CMD, are most suitable for mass derivation (see references and discussions in Mayne et al. 2007; Mayne & Naylor 2008, and Section 2.3).
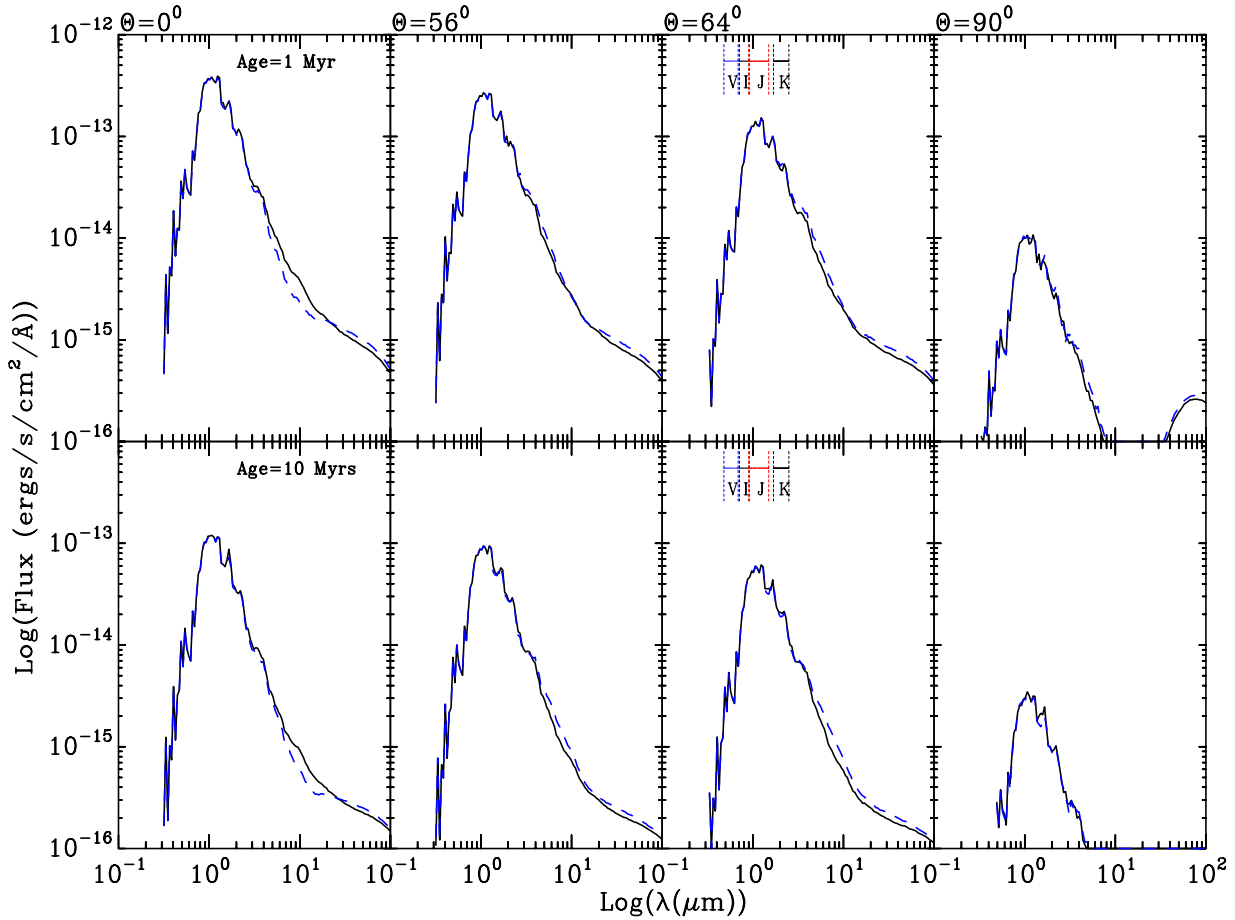
As discussed in Section 4.2 the presence of a circumstellar disc and accretion result in significant changes to the simulated SEDs for our models. Firstly, the photophere of the central star is dominated by the accretion luminosities for accretion rates of $\dot{M} > 10^{-9} M_\odot yr^{-1}$ as shown in Section 4.2.1. Secondly, for increasing accretion rates the outer

disc flaring increases, resulting in occultation of the star at smaller inclination angles, as discussed in Section 4.2.2. Finally, the location of the inner edge and flux intercepted by this edge lead to changes in its shape and subsequent dependence of the observed SED with inclination, as discussed in Section 4.2.3. In this Section we explore the effects of these changes in SED shape on the derived photometry in CMDs used for age and mass derivation for stars. The use of isochrones for the derivation of single star parameters is completely unreliable (see discussion in Mayne & Naylor 2008). However, exploring the changes in the CMDs of single objects will elucidate the causes of scatters from the expected locii in CMDs of populations of BDs.

4.4.1   Accretion Dominance-Photometry

Accretion flux was shown to dominate the underlying, intrinsic, photospheric SED for accretion rates of $\dot{M} > 10^{-9} M_\odot yr^{-1}$ (see Figure 13 in Section 4.2.1). As one would expect this leads to significant changes in the derived photometric magnitudes for bands blueward of a few microns, where the accretion and photospheric flux dominate. This is shown in Figure 23. Figure 23 shows CMDs in
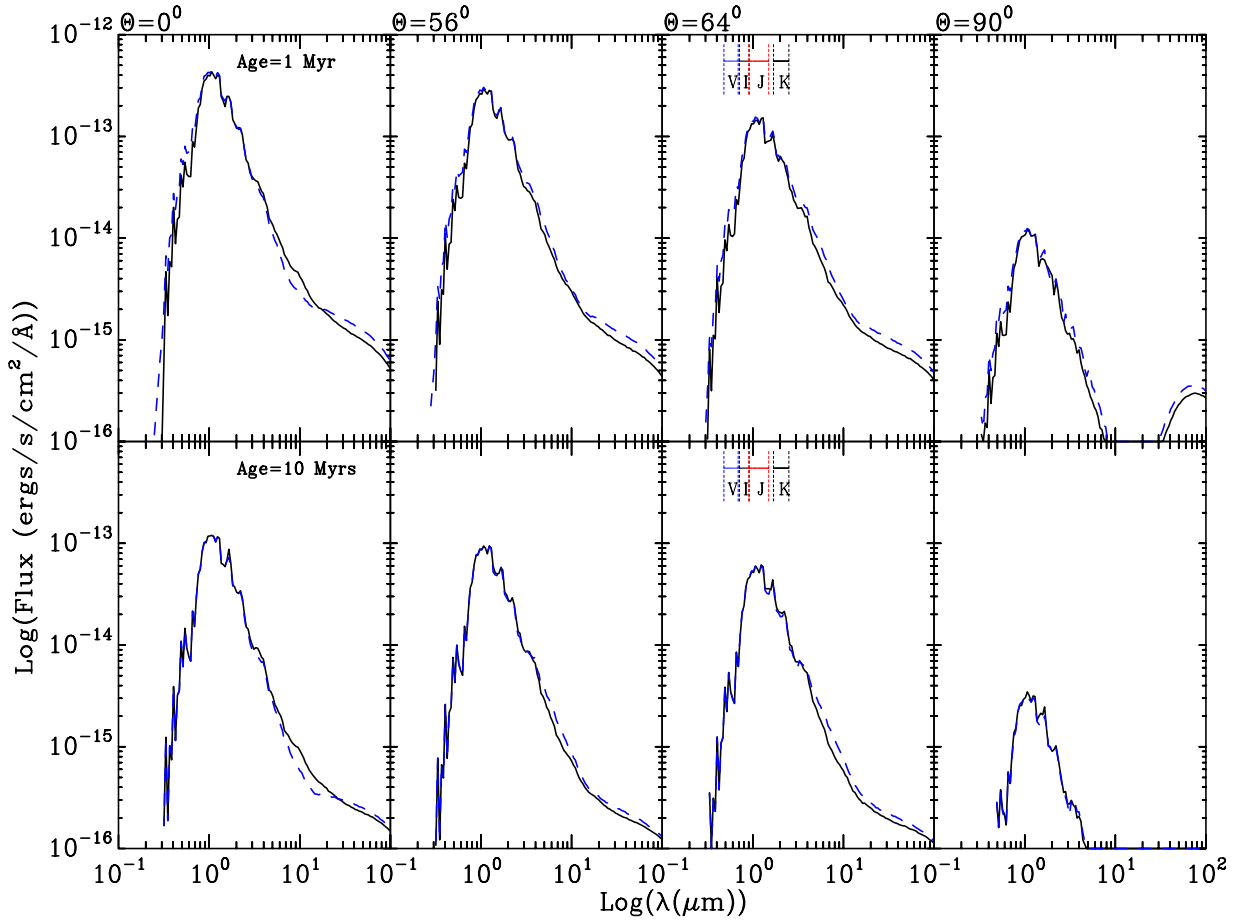
Figure 21. Figure showing SEDs of a system with a central stellar mass of $0.04M_\odot$ and accretion rate of -12 $\log(\frac{\dot{M}}{M_\odot}yr^{-1})$ with an an areal coverage of 10%. The SEDs are shown in *each panel* for a rotation period of 0.5 (solid black line) and 5 (dashed blue line) days. The *panels*, both *top* and *bottom*, (from left to right) show the total SEDs inclination angles of $0°$, $56°$, $64°$ and $90°$. The *top panels* are for systems with an age of 1 Myr and the *lower panels* are for an age of 10 Myrs. The vertical and horizontal dashed lines (in the *third panels across*) denote the approximate sensitivity ranges of our chosen V, I, J and K filters

M_V, $(V - I)_0$ (*left panels*) and M_J, $(J - K)_0$ (*right panels*) of naked stars with accretion rates of -12, -9 and -8 $\log(\frac{\dot{M}}{M_\odot}yr^{-1})$, shown as black, red and blue lines respectively (in *all panels*). The *top panels*, then show the two rotational periods of 5 and 0.5 days, as dashed and solid lines respectively, for a coverage of 10%. The *bottom panels*, then show the two areal spot coverages of 1 and 10%, as dashed and solid lines respectively, for a rotational period of 5 days.

As the rotation rate increases the co-rotation radius also increases, as shown in Equation 3, $R_{inner} \propto \tau^{\frac{2}{3}}$. Therefore, as Equations 1 and 2, show, $L_{acc} \propto 1 - \frac{R_*}{R_{inner}}$ and $T_{acc} \propto (\frac{L_{acc}}{A})^{\frac{1}{4}}$. Therefore, the temperature of the accretion hot spot increases as the coverage lowers and the rotational period increases (the latter is due to the increase in potential energy lost by the mass accreted). This can be seen in Figure 13 with lower areal coverages and longer rotational periods leading to accretion fluxes at peaking at shorter wavelengths. The *left panels* of Figure 23 show that as the accretion rate increases the stars move blueward and to brighter magnitudes in the M_V, $(V - I)_0$ CMD. Furthermore, as the accretion spot temperature is maximised i.e.

moving to longer periods of rotation or smaller areal coverages (solid to dashed lines), the stars also move blueward. For the *right panels*, or M_J, $(J - K)_0$ CMDs the behaviour is less intuitive. Increases in accretion rate lead to a slight brightening and an initial move redward, followed by a move blueward. This is as the lower accretion rates have lower hot spot temperatures, with peak wavelengths between 1 and 3 μm (corresponding to temperatures of ~2800 K to ~900 K, the range of the BD photosphere). This leads to increases in the red flux and changes in the slope from J to K. At the higher accretion rates the accretion flux dominates and cause the blueward shift as the slope becomes larger. For the highest accretion rate, in the *bottom right panel*, a change to a hotter spot (reduction in coverage, from solid to dashed lines) results in a move redward in the CMD. This can be understood by observing the solid blue lines in the *top panels* of Figure 13. Essentially, the reduction in spot temperature moves the accretion flux to much shorter wavelengths, ~0.5 to ~0.3 μm, meaning that the flux in the J and K bands becomes more like the photosphere, and less dominated by accretion. The *top right panel* of Figure 23 then shows that increases in the rotation period (from solid to dashed lines) shows a move blueward in the CMD, resulting in changes

Figure 22. Figure showing SEDs of a system with a central stellar mass of $0.04M_\odot$ and accretion rate of -9 $\log(\frac{\dot{M}}{M_\odot}yr^{-1})$ with an an areal coverage of 10%. The SEDs are shown in *each panel* for a rotation period of 0.5 (solid black line) and 5 (dashed blue line) days. The *panels*, both *top* and *bottom*, (from left to right) show the total SEDs inclination angles of 0°, 56°, 64° and 90°. The *top panels* are for systems with an age of 1 Myr and the *lower panels* are for an age of 10 Myrs. The vertical and horizontal dashed lines (in the *third panels across*) denote the approximate sensitivity ranges of our chosen V, I, J and K filters

of the peak accretion flux emission from 0.58 to 0.5 μm, meaning significant flux from the accretion hot spot will still fall in the J and K bands, and the slope will be increased.

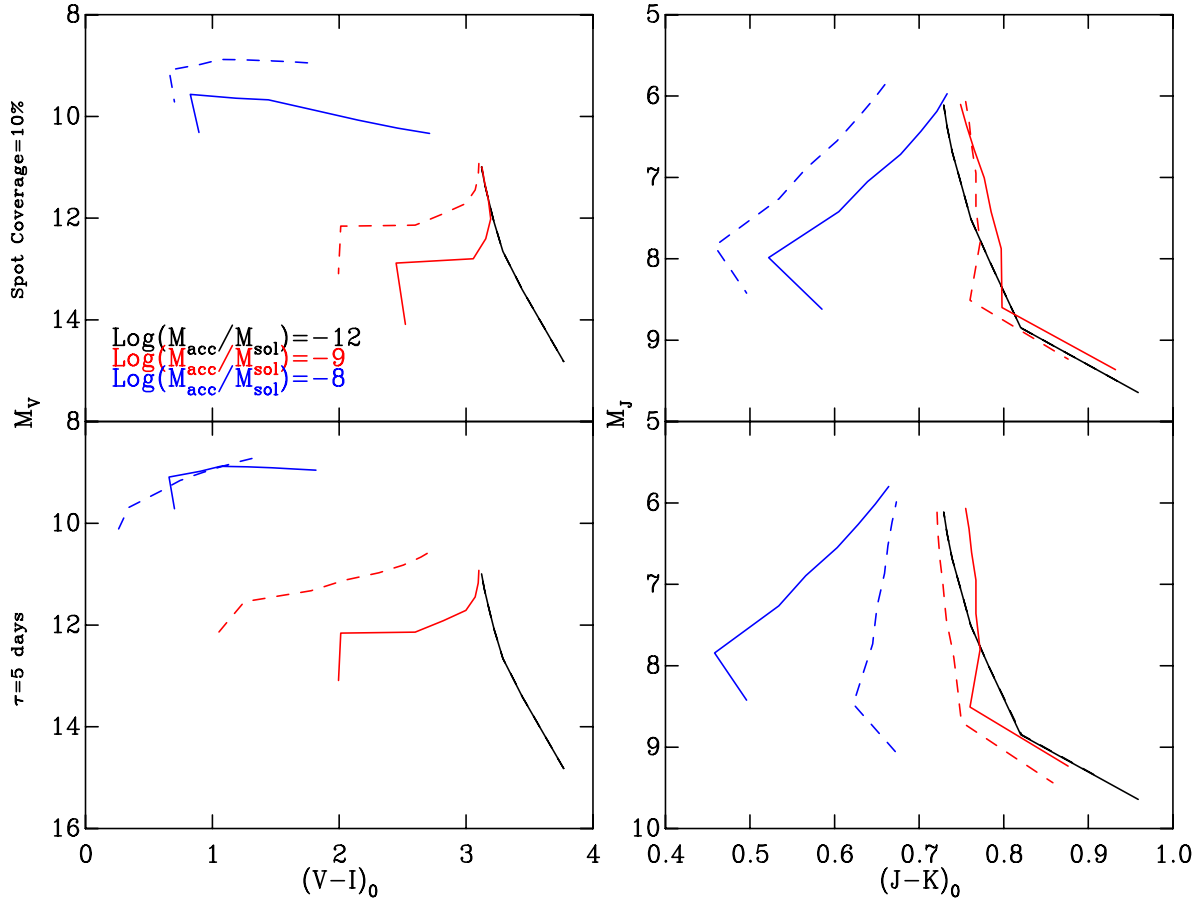### 4.4.2 Effect of Flaring and Obscuration on Photometry

As described by Walker et al. (2004) the increased flaring, in BDD systems when compared to CTTS, leads to more significant changes in the photometric characteristics of the BDD stars with inclination changes. The increased flaring shown in Figures 2 and 3 results in increased obscuration of the central star (and inner edge) at earlier inclinations. This obscuration is shown to occur at lower inclination angles for objects accreting at higher levels, as shown in Figure 15. Figure 15 shows that significant obscuration occurs at inclinations of 71 and 56° for accretion rates of -12 and -7 $\log(\frac{\dot{M}}{M_\odot}yr^{-1})$, respectively. The changes in flux with inclination will clearly lead to a change in the observed magnitude with inclination. Figure 24 shows the M_V and M_J magnitude, in the *top* and *bottom panels* respectively, as a function of inclination with the individual points marked as crosses. The *top* and *bottom panels* show accretion rates of

-12, -9 and -7 $\log(\frac{\dot{M}}{M_\odot}yr^{-1})$ as black, red and blue lines. The solid lines are for objects with rotational periods of 0.5 days and the dashed lines are for periods of 5 days. The *inset panel* within the *bottom panels* shows an enlargement of the section of inclinations from 40 to 80°. For *all panels* the vertical dotted lines show the inclinations for which significant drops in flux are observed (see Figure 15) for -12 and -7 $\log(\frac{\dot{M}}{M_\odot}yr^{-1})$ in black and blue respectively.

Figure 24 shows that the occultation starts earlier for the higher accretion rates, shown by the increase in both magnitudes (*top* and *bottom panels*) with inclination angle at around 56 and 71°, as also shown in Figure 15. The slower rotation rates, for the highest accretion rates, show a generally fainter magnitude, than the faster rotating systems, caused by a larger disc scaleheight. For M_J the fall in magnitude is again earlier and more significant for the larger accretion rates. However, at higher inclinations the systems become brighter again, show in the *inset panel*. This brightening is due to the curved inner wall, as shown in Figures 18 (discussed in more detail in Section 4.4.3).

The change in magnitude, will also lead to a change in colour. As described V, $V - I$ and J, $J - K$ CMDs are

Figure 23. Figure showing the naked systems for accretion rates of -8, -9 and -12 $\log(\frac{\dot{M}}{M_\odot}yr^{-1})$, shown in *all panels* as blue, red and black lines respectively. The model shown for *all panel* has a mass of $0.04M_\odot$ and an age of 1Myr. The *top panels* are models with areal spot coverages of 10%, and the *lower panels* are for models with rotational periods of 5 days. The dashed and solid lines then delineate the rotation periods for the *top panels* and coverages for the *bottom panels*. The dashed lines show the rotational periods of 5 days (*top panels*) and coverages of 1% (*bottom panels*). The solid lines denotes periods of 0.5 days (*top panels*) and coverages of 10% (*bottom panels*). For accretion rates of -12 $\log(\frac{\dot{M}}{M_\odot}yr^{-1})$ (black line, *all panels*), are representative of all models at this rate, as the models are coincident within the CMD.
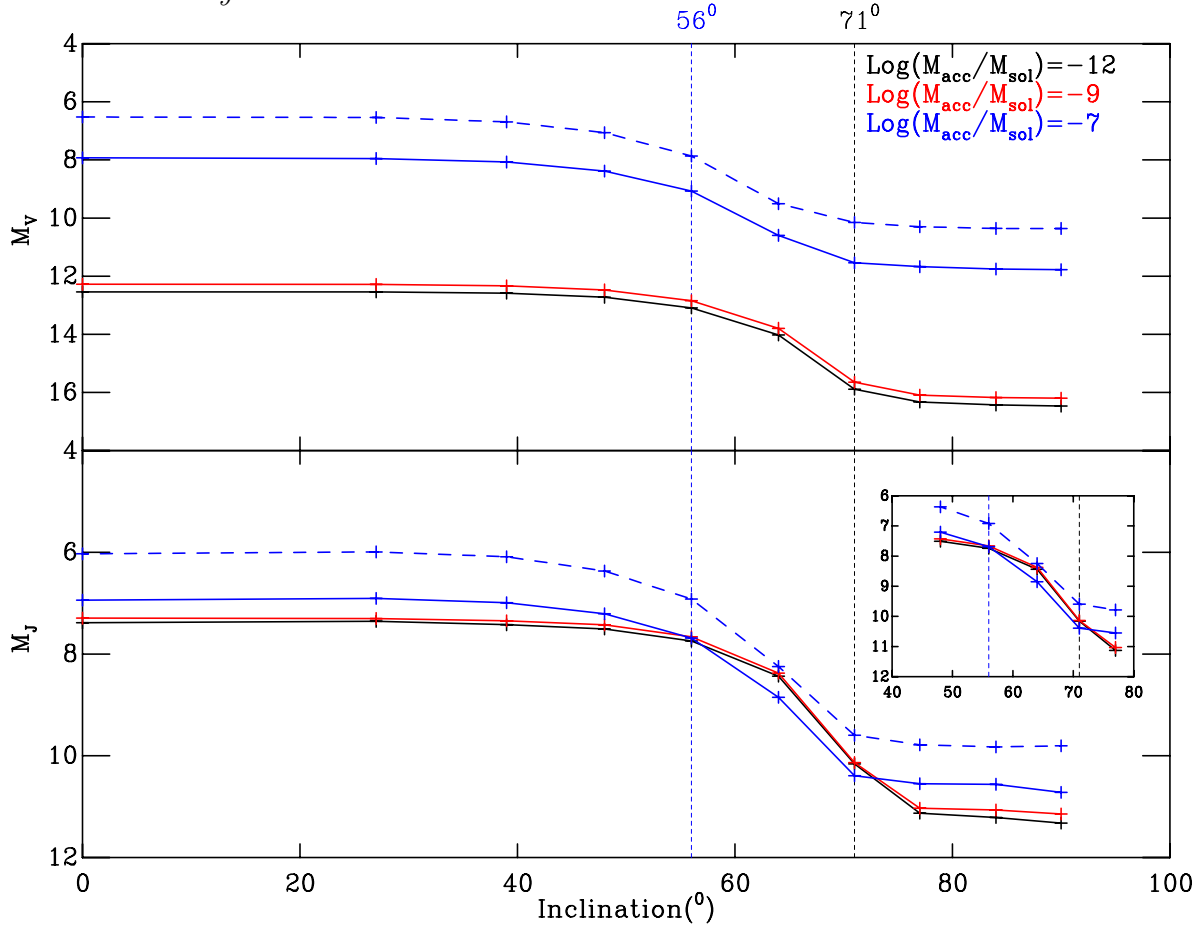
ubiquitously used for derivation of ages and masses. The use of isochrones to derive ages and masses of individual stars is not reliable. However, it is informative to explore the changes in the CMD position of our BDD systems. Figure 25 shows M_V, $(V-I)_o$ CMDs for the accretion rates of -12 and -7 $\log(\frac{\dot{M}}{M_\odot}yr^{-1})$, as the *left* and *right panels* respectively. The systems are those shown in Figure 2 and 3, at all modeled inclinations. For *both panels* the red dashed line, with the data points marked as crosses, shows the changes in CMD position with inclination of the BDD system at different inclinations for a 1 Myr system (with an areal coverage of 10% and a τ of 5 days). The solid blue line is the matching isochrone for naked systems, with the naked $M_* = 0.04M_\odot$ marked as a triangle. Again, for *both panels* the inclinations at which significant drops in flux were found in Figure 15 are noted in red text.

Figure 25 shows that as the system changes in inclination it leads to a significant dimming in both cases. The inclinations from Figure 15 where significant flux is lost are shown and it can be seen that a significant drop in magnitude is apparent just before this inclination (as also shown

in Figure 24). The models in *both panels* get slightly redder as we increase to the obscuration angle, caused by scattered light from the disc this can be observed for the accretion rate of -12 $\log(\frac{\dot{M}}{M_\odot}yr^{-1})$ in Figures 19 and 21.

Figure 26 shows the same data as Figure 25 with the same notation and symbol meanings.

Figure 26 again, as in Figure 25, shows the BDD systems dimming with increasing inclination, with some move towards redder colours. There is an offset between the naked and BDD systems at face on inclinations, caused by the inner disc wall. This is particularly large for the higher accretion rate (*right panel*). This increase in reddening for the higher accretion rates is due to the much larger and curved inner disc edge as shown in Figure 10. This curved inner edge also leads to less dependence of $(J-K)_0$ on inclination angle, as compared to the lower accretion rate.

Figure 24. Figure showing magnitude change with inclination for M_V (*top panel*) and M_J (*bottom panel*) for the models shown in Section 4.1, Figures 7 to 11. The accretion rates of -7, -9 and -12 $\log(\frac{\dot{M}}{M_\odot}yr^{-1})$ are shown as blue, red and black lines respectively. The individual points are shown as crosses for all data. The dashed lines show the systems with rotational periods of 5 days and the solid lines 0.5 days, in *all panels*. A section of the *bottom panel* has been enlarged and is shown as the *inset panel*. Note the models for -12 $\log(\frac{\dot{M}}{M_\odot}yr^{-1})$ are coincident in this Figure. *All panels* show the inclinations are which obscuration occurs for -12 and -7 $\log(\frac{\dot{M}}{M_\odot}yr^{-1})$ as dashed black and blue lines respectively.
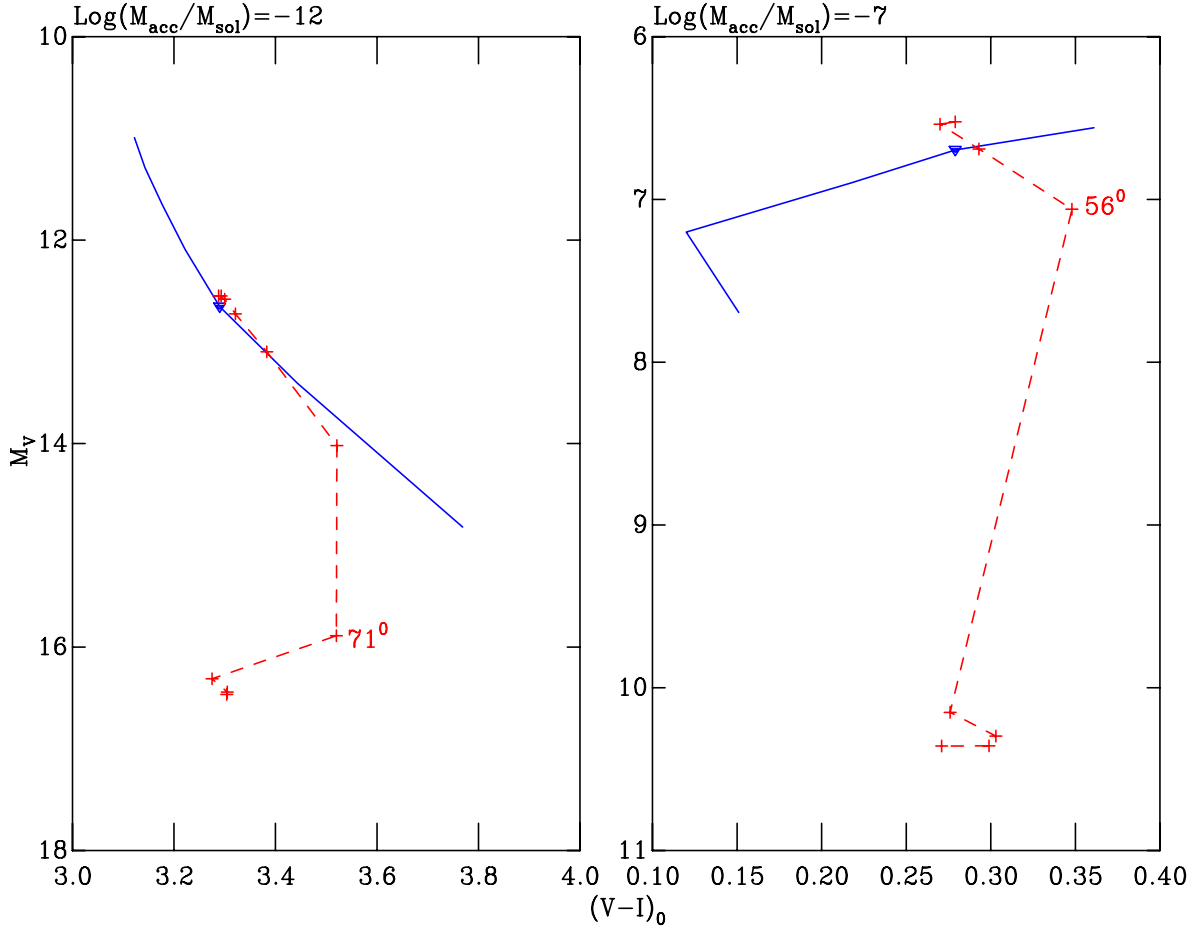
4.4.3   Inner Edge and Photometry

It is clear that the scatter within a CMD, in particular for the M_J, $(J-K)_0$ CMD, is strongly affected by the emission from the inner edge (as shown in Figure 26).

Figure 27 shows the position in a CMD of the models from Figures 8, 9, 10 and 11. The accretion rates shown are -12, -7, -9 and -6 $\log(\frac{\dot{M}}{M_\odot}yr^{-1})$, as the *top left, bottom left, top right* and *bottom right panels*. The solid blue line in *all panels* of Figure 27 show the naked isochrone at 1 Myr (with an areal coverage of 10% and τ of 0.5 days), at the shown accretion rate. The dashed red line shows the BDD system matching the naked isochrone, except with $M_* = 0.04 M_\odot$, at all inclination rates, with the datapoints marked as crosses. The blue triangles are then the naked stars at $M_* = 0.04 M_\odot$. The points at which the thermal direct flux reaching the observer drops significantly are marked in red text for each system, as shown in Figures 16 and 17.

Figure 27 shows for the M_V, $(V-I)_0$, the inclination increase again dims the star for these models and moves it initially redward, until it exceeds the expected obscuration angle, found from Figures 16 and 17. However, as we move

through the accretion rates from -12 $\log(\frac{\dot{M}}{M_\odot}yr^{-1})$ (*top left panel*) to -6 $\log(\frac{\dot{M}}{M_\odot}yr^{-1})$ (*bottom right panel*) the transition from edge-on to face-on system tends to a sharper feature, with the reddest point at the obscuration angle. As would be expected from the SEDs shown in Figure 18. This is caused by maximising the amount of the inner edge which is visible, whilst the stellar photosphere is still visible (which also contributes in these passbands).

Figure 28 shows the same information as Figure 27 but for a M_J, $(J-K)_0$ CMD. Here, the BDD isochrones are initially much redder than their naked counterparts, as expected due to IR excesses caused by the disc inner edges. As the inclination increase for the lower accretion rates (*top left* and *bottom left panels*) the system moves first redward and then sharply blueward as the SED becomes dominated by scattered light only. As can be seen in Figure 18. For the extreme accretion rates the wall is no longer vertical and the change in infrared colours is smoother up until the obscuration angle.

Figure 25. Figure showing the positions within a M_V, $(V-I)_0$ of the models in Figures 2 and 3 (Section 4.1) as the *left* and *right panels* respectively. The solid blue line are the 1Myr naked isochrones at the accretion rates of -12 and -7 $\log(\frac{\dot{M}}{M_\odot}yr^{-1})$ for the *left* and *right panels* respectively (with an areal coverage of 10% and a τ of 5 days). The dashed red line is the BDD system with $M_* = 0.04M_\odot$ at all simulated inclinations. The triangles, in both panels are the $0.04M_\odot$ stars on the naked isochrones and the crosses show this mass over the range of inclinations with an associated disc. Figure 15 predicts an occultation angle of 71 and 56° for the -12 and -7 $\log(\frac{\dot{M}}{M_\odot}yr^{-1})$ models respectively, and these are denoted by the text within the figure.
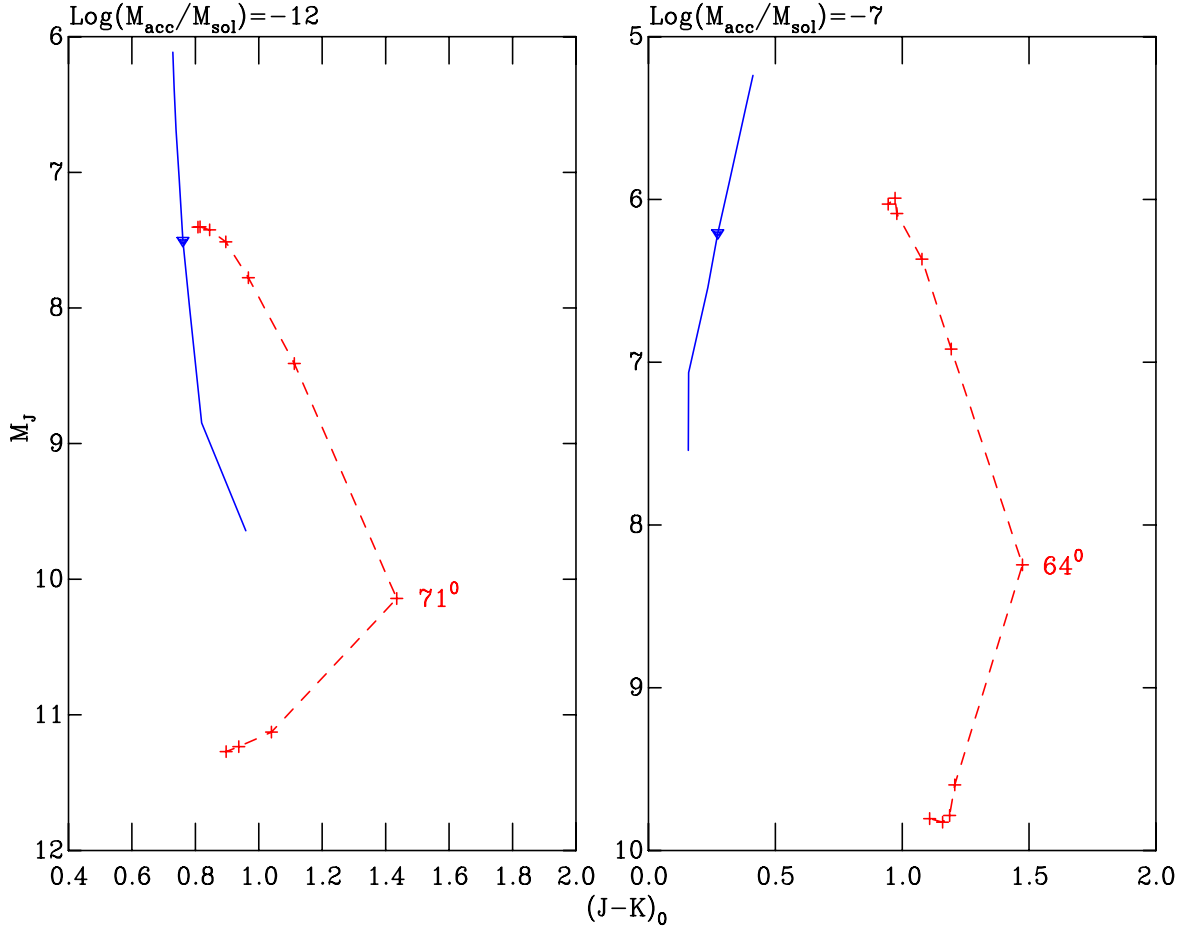
4.5 Populations

Practically, the derivation of parameters for pre-MS populations uses CMDs and isochrones applied to clusters or populations of stars. In this section we explore the scatters of our BDD systems across our grid of input values within typical or commonly used CMDs and CoCoDs for deriving ages, masses and disc fractions.

To delineate the effects of the accretion rate and circumstellar discs we have subdivided the grid into two groups (as discussed in Sections 4.1 and 4.2), those with accretion rates typical for higher mass CTTS objects, defined as $\dot{M} = 10^{-12}M_\odot yr^{-1}$ (negligible) to $\dot{M} = 10^{-9}M_\odot yr^{-1}$ and those with elevated accretion rates, where $\dot{M} > 10^{-9}M_\odot yr^{-1}$. For several of the plots in this section the magnitude and colours for the $M_* = 0.01M_\odot$ systems at high inclinations become extremely faint and red. In some cases these objects appear slightly without the scale of the diagram the axes were limited in this way to be able to show the changes in colour and magnitude for the majority of stars better. The colours and magnitudes for these lowest mass stars are not necessarily unreliable but simply hinder

the aesthetics of the plots, and as they are at the limits of our grid we have decided to omit them from some Figures by trimming the axes. Additionally, stars at the highest inclinations, i.e edge on disc systems, are often omitted from the Figures due to their extremely faint magnitudes, meaning they would not be practically observable.

4.5.1 Age and Mass Derivations

As discussed in Section 4.4 for the derivation of the primary parameters of age and mass the CMDs most suitable and commonly used are M_V, $(V-I)_0$ and M_J, $(J-K)_0$. Furthermore, these CMDs are indicative of the associated CMDs, for instance M_R, $(R-I)_0$ or M_J, $(J-H)_0$ etc. Also as discussed in Mayne & Naylor (2008) the use of isochrones for the derivation of masses and ages for individual pre-MS stars is unreliable at best. Practically, therefore, median ages are derived from populations. Subsequently, derived masses are still unreliable but at least based on a consistent age. This problem is being addressed by Bell et al (in prep), where K band photometry and known eclipsing binaries are being used to refine pre-MS isochrones. In this section we
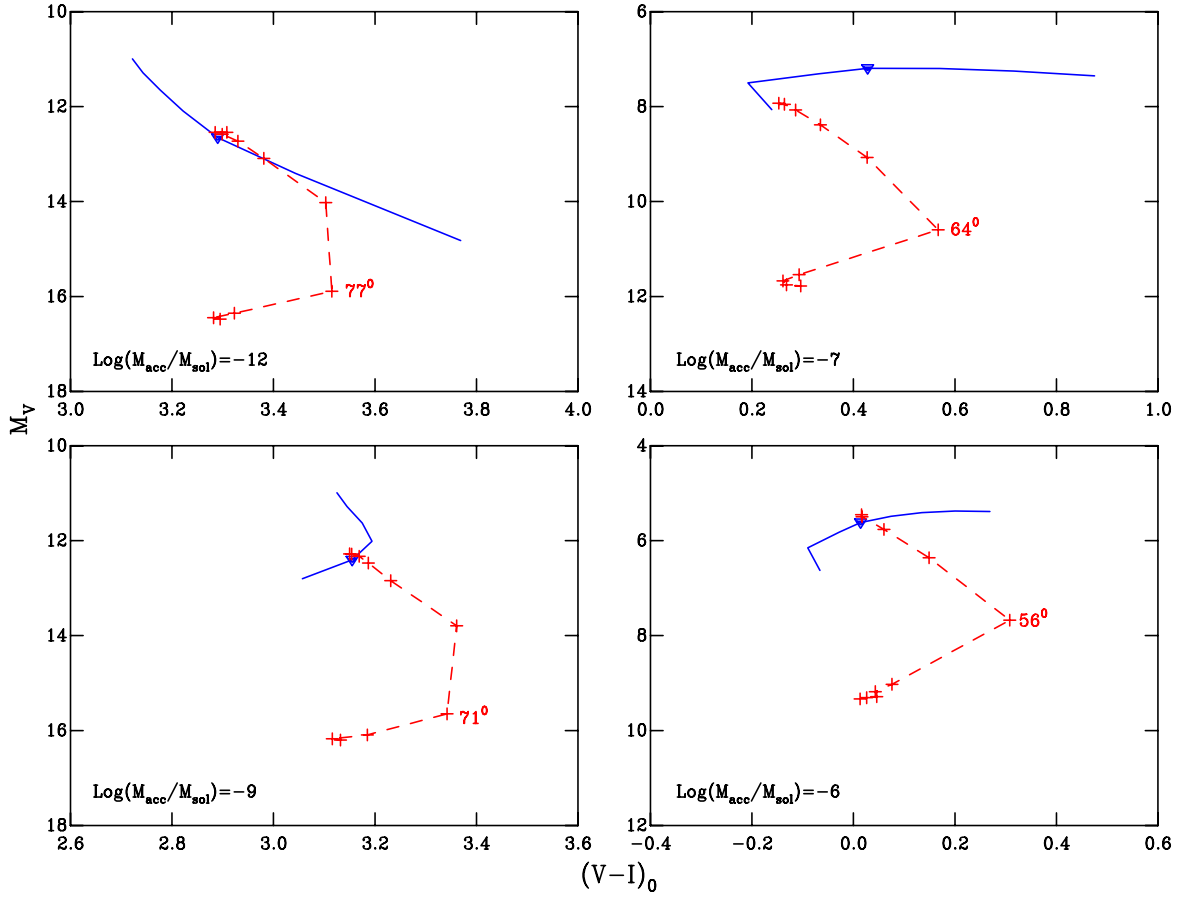
Figure 26. Figure showing the positions within a M_J, $(J-K)_0$ of the models in Figures 2 and 3 (Section 4.1) as the *left* and *right panels* respectively. The solid blue line are the 1Myr naked isochrones at the accretion rates of -12 and -7 $\log(\frac{\dot{M}}{M_\odot}yr^{-1})$ for the *left* and *right panels* respectively (with an areal coverage of 10% and a τ of 5 days). The dashed red line is the BDD system with $M_* = 0.04 M_\odot$ at all simulated inclinations. The triangles, in both panels are the $0.04 M_\odot$ stars on the naked isochrones and the crosses show this mass over the range of inclinations with an associated disc. Figure 15 predicts an occultation angle of 71 and 56° for the -12 and -7 $\log(\frac{\dot{M}}{M_\odot}yr^{-1})$ models respectively, and these are denoted by the text within the figure.

plot the data for our 1 Myr systems only and explore the resulting scatters caused by the disc presence and accretion luminosity.

Figures 29 and 30 shows four CMDs in M_V, $(V - I)_0$ for the typical and extreme accretors respectively. For the typical accretors, Figure 29, shows the isochrones constructed for naked systems at 1 Myr, for accretion rates of -12 and -9 $\log(\frac{\dot{M}}{M_\odot}yr^{-1})$, as the solid and dashed black lines. Whereas in Figure 30 the naked isochrones of -9 and -6 $\log(\frac{\dot{M}}{M_\odot}yr^{-1})$, as dashed and solid black lines respectively. The *top left panel*, in both Figures (29 and 30) shows a pre-MS isochrone at 1 Myr from Siess et al. (2000) adjusted to a distance of 250pc and an extinction of $A_V = 2$ mag, simulating a background population of CTTS stars. The dots in *each panel*, for both Figures (29 and 30) are the 1 Myr BDD systems for all inclinations, rotational periods, areal spot coverages and the individual accretion rates within the accretion type classes. The *panels* of the Figures 29 and 30 then separate the systems by the input variables. The *top left panel* shows either the accretion rates of -9, -10 and -11 & -12 or -6, -7 and -8 $\log(\frac{\dot{M}}{M_\odot}yr^{-1})$ in Figures 29 and 30 respectively.

These three classes are then shown as blue, black and red dots respectively. The *bottom left panels* then show those systems with areal coverages of 1 and 10% as blue and red dots respectively. The *top right panels* then shows systems with rotational periods of 0.5 and 5 days as blue and red dots respectively. Finally, the *bottom right panels* show the systems separated by inclination. These groups are $\theta \leqslant 48°$ as blue dots (classed as face-on systems), $\theta > 56$ & 64° (classed as the expected systems, as the expectation value of $cos(\theta) = 60°$) as black dots and $\theta \geqslant 71°$ (classed as edge-on systems) as red dots. Figure 31 also shows the same data as for Figure 29, but for M_R, $(R - I)_0$ CMDs.
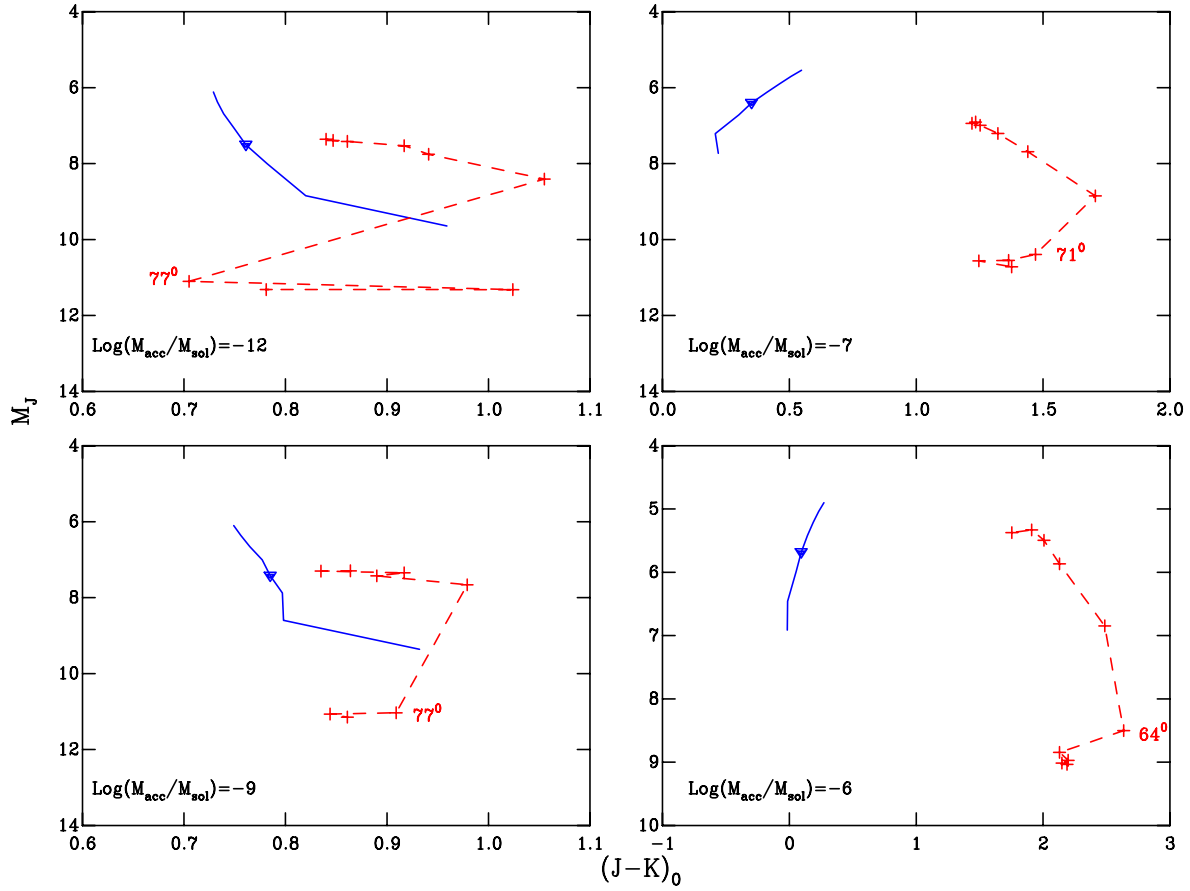
As can be seen in Figure 29 current accretion in a star and disc systems, for rates typical in the BD mass regime, creates a scatter in our simulated photometry indicative of a much larger isochronal age spread than 10 Myr. Indeed, for many BDD systems even at nominal accretion rates of -11 or -12 $\log(\frac{\dot{M}}{M_\odot}yr^{-1})$, for our simulations, the colours of these stars move significantly blueward of the expected BD locus in a M_V, $(V - I)_0$ CMD. As the dots in Figure 29 are the simulated photometry of BDD systems over a range of typ-

Figure 27. Figure showing the positions within a M_V, $(V - I)_0$ of the models in Figures 8, 9, 10 and 11 as the *top left, bottom left, top right* and *bottom right panels* respectively. As for Figure 25, the solid blue line is the naked isochrone at 1 Myr for the corresponding accretion rate (-12, -9, -7 or -6 $\log(\frac{\dot{M}}{M_\odot}yr^{-1})$). The dashed red line is the BDD isochrone at the same age and accretion rate. The inclination of each model at which obscuration is expected to occur, from Figures 16 and 17, is denoted in text.

ical input parameters (see Section 3), an observed coeval 1 Myr population could reasonably be expected to show a similar scatter. The naked isochrones show that this spread in simulated photometry, would lead to a spread in isochronal age greater than the ≈ 10 Myr spread claimed for higher mass stars in some star forming regions (for instance the ONC). Furthermore, for the higher accretion rates of -9 or -10 $\log(\frac{\dot{M}}{M_\odot}yr^{-1})$ the movement of the star within the CMD will effectively move the star into the contamination region expected for background CTTS or MS stars at a $(V - I)_0$ of $\leqslant 1.5$ and M_V 12-10, and as such the star would not be included in a photometrically selected BD sample. The solid green line, in the *top left panel*, showing the 1 Myr isochrone of Siess et al. (2000) at a distance of 250 pc and extinction of $A_V = 2$ mags shows that the BDD systems with higher accretion rates could easily be confused for a background CTTS or MS population (as MS stars are simply less luminous at a roughly constant V-I than the CTTS counterparts). Indeed miss classification of a BDD system as a CTTS system has already been revealed in White & Basri (2003). Furthermore, scatter, although somewhat reduced, can be observed in the simulated photometry of the negligibly accreting systems, for example in the *top left panel*

some red dots, accreting at -12 or -11 $\log(\frac{\dot{M}}{M_\odot}yr^{-1})$ (which will be negligible compared to the photospheric flux, see Figure 13), still scatter significantly. These objects may still be included in a 'wide' photometric selection. This scatter is a strong function of inclination, as shown in the *bottom right panel*, where, as the inclination is increased the objects are pushed lower in the CMD. Indeed, for the edge on cases some objects have magnitudes fainter than show in Figure 29 ($M_V \approx 20$). This is expected as the star becomes obscured by the flared disc, interestingly for these systems the *bottom right panel* shows that this occurs for inclinations above around 71° (as found in Figure 15) in most cases. However, even for the lower inclination angles some objects have very faint magnitudes, this is due to the disc flaring leading to a smaller opening angle and is discussed in Section 4.1. The *bottom left panel* shows that for naked systems accretion rates of -9 $\log(\frac{\dot{M}}{M_\odot}yr^{-1})$ lead to the stars being scattered into the region occupied by background CTTS and contamination (the lower accretion rates are all coincident with the -12 $\log(\frac{\dot{M}}{M_\odot}yr^{-1})$ for 1 Myr). Crucially, the *top left panel* shows that the scatter from the isochrone is, generally, correlated with accretion rate. Effectively, as the accretion rate increases the BDD system moves farther away

Figure 28. Figure showing the positions within a M_J, $(J-K)_0$ of the models in Figures 8, 9, 10 and 11 as the *top left*, *bottom left*, *top right* and *bottom right panels* respectively. As for Figure 25, the solid blue line is the naked isochrone at 1 Myr for the corresponding accretion rate (-12, -9, -7 or -6 $\log(\frac{\dot{M}}{M_\odot} yr^{-1})$). The dashed red line is the BDD isochrone at the same age and accretion rate. The inclination of each model at which obscuration is expected to occur, from Figures 16 and 17, is denoted in text.

from the isochrone and is therefore less likely to be classified as a BDD system and included in any target samples of such objects. The *top right panel* shows that the scatter, in M_V, in our simulated photometry from the isochrones is significant for both areal coverages. The *bottom left panel*, shows significant scatter in the simulated photometry for both adopted rotation periods. This panel also shows that scatter in this diagram is not obviously correlated with the rotation period and therefore inner edge position. Overall, as found in Walker et al. (2004), the dominant scattering effect for BD disc systems in an optical CMD appears to be caused by accretion rate and inclination, and therefore obscuration effects of the disc on the star. This suggests that for a given photometric survey of BDD systems accreting at typical accretion rates and with an expected range of inclinations (centred on around $60°$) one would expect to exclude a significant fraction of these objects from any isochrone based selection.
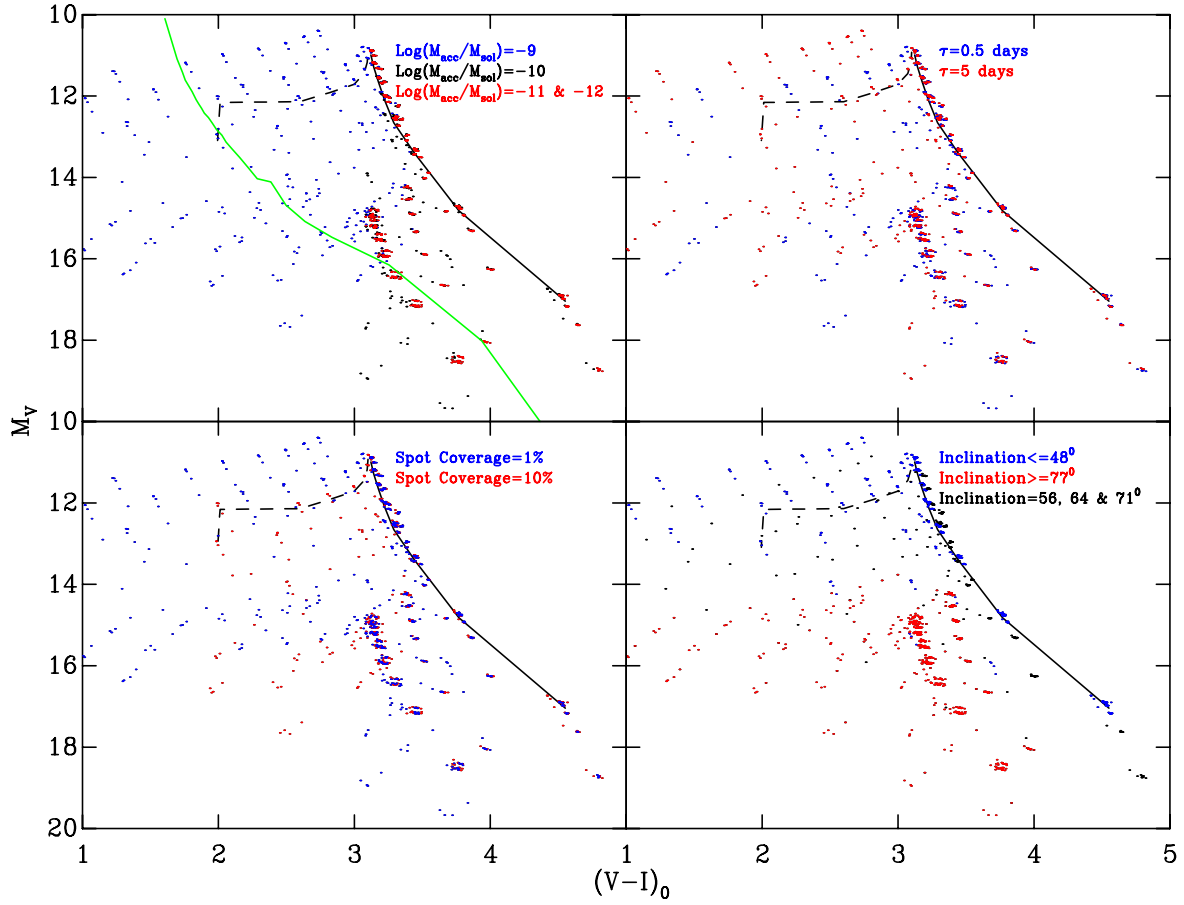
Figure 30 shows that for extreme accretion rates the BDD objects move significantly blueward and brighter than the naked isochrone (the naked isochrone at -9 $\log(\frac{\dot{M}}{M_\odot} yr^{-1})$ is shown for comparison). Comparison of the *four panels* again show that, in general, the scatter is chiefly correlated with accretion rate and inclination. Essentially, Figure 30

shows that for, admittedly extreme, accretion rates BDD systems will not be included in a photometrically (or indeed spectroscopically, from Section 4.2) selected sample.

Similar scattering, as observed in Figure 29, occurs when using CMDs constructed using M_R, $(R-I)_0$ (using the photometric system of Bessell et al. 1998), except that the 1 Myr pre-MS isochrone has been omitted. Figure 31 shows the M_R, $(R-I)_0$ CMD.

Similar consequences are apparent in CMDs best suited, and most used, for derivation of masses using isochrones. Figure 32 shows the same data as Figure 29 in the same format except in this case the pre-MS isochrone of Siess et al. (2000) has been smoothed, purely for aesthetics and to remove the sharper features. Again Figure 33 contains the same data in the same format as Figure 30 except that the naked star isochrone at an accretion rate of -6 $\log(\frac{\dot{M}}{M_\odot} yr^{-1})$ is not shown as it lies significantly blueward of the CMD.

Figure 32 shows that for typical accretion rates and expected ranges of the other input variables the spread in CMD positions is large. Indeed, the *top left panel* again shows that, as in the M_V $(V-I)_0$ case, some of the BDD objects will appear as redenned background CTTS objects. Scrutiny of the *individual panels* shows no clear correlation of CMD position with input variable except for the inclina-

Figure 29. Figure showing CMDs in M_V, $(V - I)_0$ for typical accretors $(\dot{M} \leqslant$ -9 $\log(\frac{\dot{M}}{M_\odot}yr^{-1}))$. The black solid and dashed lines in *all panels* are the naked star isochrones for accretion rates of -12 and -9 $\log(\frac{\dot{M}}{M_\odot}yr^{-1})$ respectively. The *top left* only shows the 1 Myr pre-MS isochrone of Siess et al. (2000) adjusted to a distance modulus of 7 and an extinction of $A_V = 2$, simulating a reddened background population. The dots are the data for typical accretors for models at 1 Myr. The data are then separated by input variables, in the *panels*. The *top left panel* shows three accretion classes, -9, -10 and -11 & -12 $\log(\frac{\dot{M}}{M_\odot}yr^{-1})$, as blue, black and red dots respectively (the lowest two accretion rates are grouped as they are coincident). The *top right panel* shows the rotational periods of 0.5 and 5 days as blue and red dots respectively. The *bottom left panel* shows the areal spot coverages of 1 and 10% as blue and red dots resepctively. The *bottom right panel* shows three groups of inclinations, $\theta \leqslant 48°$, $\theta \geqslant 77°$ and $\theta = 56, 64$ & $71°$, as blue, red and black dots respectively.
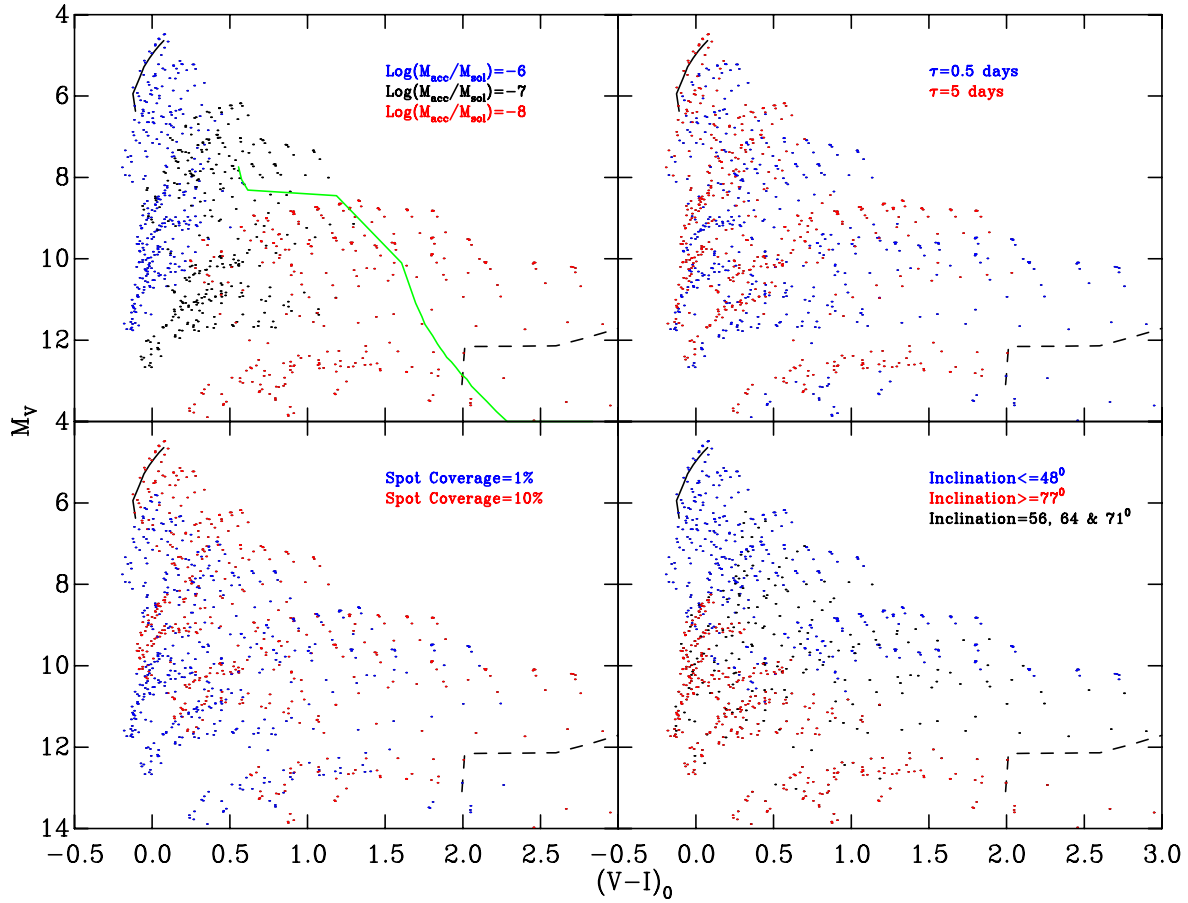
tion. As shown in the *bottom right panel* as the inclination increases the systems move to fainter magnitudes and redder colours, in general. The *top right panel* of Figure 32 shows that for typical accretion rates there does not appear to be a correlation of $(J - K)_0$ colour with rotation rate as expected from the modeling of flat disc by Meyer et al. (1997). It is clear that assigning masses to accreting BDD systems using isochrones, for our model grid, would result in the incorrect masses. In addition, photometric sample selection for BD systems will also exclude the majority of our higher accretion rate objects. Figure 33 shows that for extreme accretors the scatter is much larger, and again correlated only with inclination, and perhaps accretion rate to a lesser degree (*bottom right* and *top left panels* of Figure 33).

4.5.2 Summary

Therefore, if one adopts the range of input parameters we have used (see Section 3 for justification), our simulated pho-

tometry shows, qualitatively, that a coeval 1 Myr population of accreting BD stars and BDD systems, with typical accretion rates and range of inclinations, will exhibit a significant scatter in apparent isochronal age of (>10 Myr). Furthermore, objects with typical (and extreme) accretion rates are scattered sufficiently in CMD space to prohibit their identification as pre-MS BDs. Indeed, these objects would not be included in a photometrically selected sample of BDs, and as such are unlikely to be assigned the correct masses or ages. The scatter from the naked 1 Myr systems, generally, increases with increasing accretion rate. It is important to note at this point that these conclusions are qualitative, and obviously based on our assumptions. However, the repercussion for isochronal age derivation and sample selection in the BD regime could be profound. Indeed this study has only included the effects of current or ongoing accretion from a disc, it has neglected any effects of accretion, both past and present, on the evolution of the central star. This past accretion could also act to reduce the stars radius, accelerating

Figure 30. As Figure 29 except for extreme accretors, $\dot{M} \geqslant$ -8 $\log(\frac{\dot{M}}{M_\odot} yr^{-1})$. In this Figure the solid black line now shows naked systems with an accretion rate of -6 $\log(\frac{\dot{M}}{M_\odot} yr^{-1})$ (as opposed to -12 $\log(\frac{\dot{M}}{M_\odot} yr^{-1})$, as in Figure 29, the dashed black line is still for an accretion rate of -9 $\log(\frac{\dot{M}}{M_\odot} yr^{-1})$.

contraction (Tout et al. 1999; Siess et al. 1999) and introducing additional scatter in a coeval population proportional to the range in accretion rates (see Mayne & Naylor 2008, for full discussion). Our findings support those of Walker et al. (2004), showing that a significant scatter is caused by obscuration of the central source by the central disc. In addition we have shown that the typical accretion rates may scatter BDD systems into the region of a CMD occupied by the CTTS or background MS locus.

The fact that scatter in the CMD increases with increasing accretion rate casts doubt on the veracity of the mass to accretion rate relationship. For our model grid we have not assumed any such relation, therefore, as our data would also show a similar relation it suggests that the observed result may be caused by intrinsic scattering. The relation, $\dot{M} \propto M_*^2$ suggests that their is a dearth of lower mass stars accreting at higher rates. We have shown that for accretion rates in the range -12 to -9 $\log(\frac{\dot{M}}{M_\odot} yr^{-1})$ the BDD systems with higher accretion rates would be preferentially missed using photometric or isochronal selection.

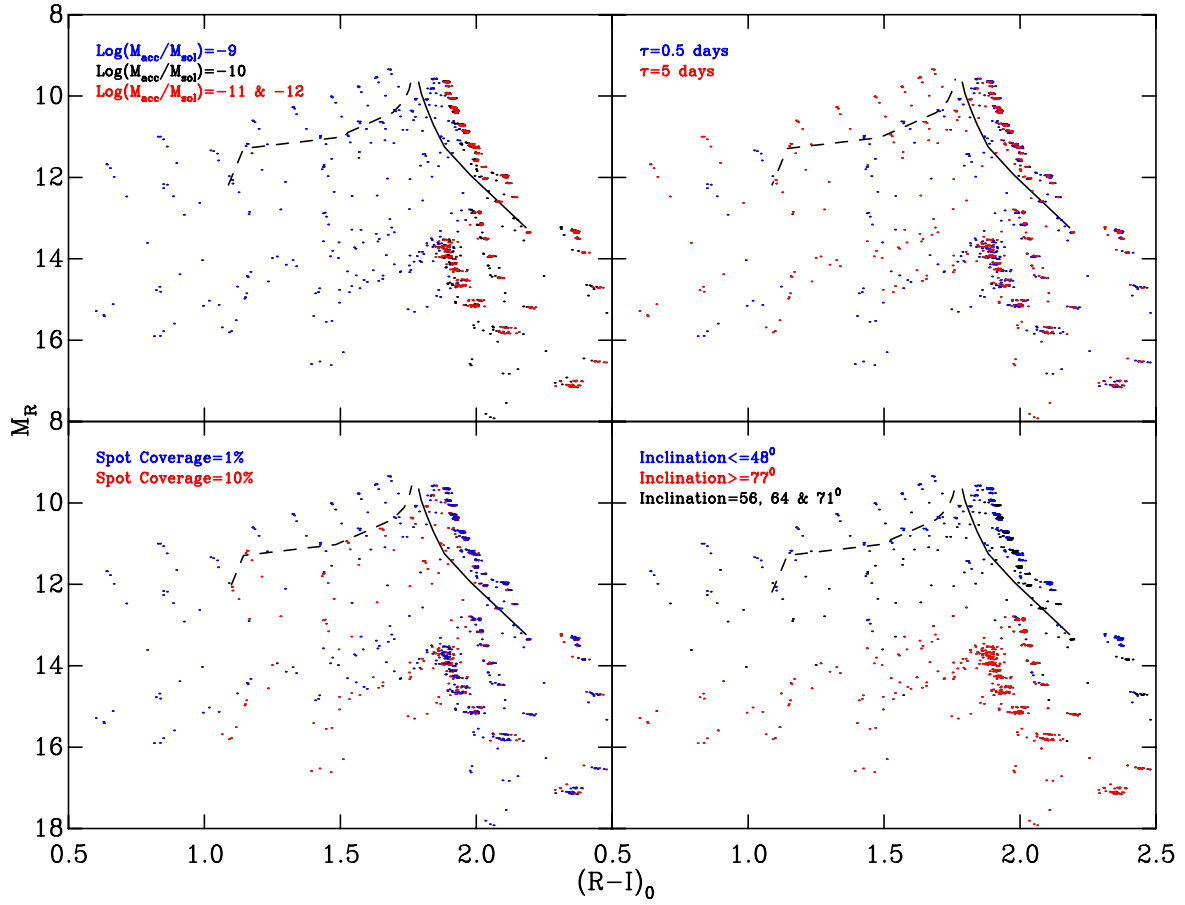Additionally, we have adopted the co-rotation radius as the initial location of our inner wall. This leads to an initial proportionality between the rotation rate and inner edge temperature. As discussed in Section 4.1 this correlation will be modified due to dust sublimation effects, weakening the correlation. The derived photometry however, at varying inclinations, does not show a strong correlation in IR, $(J - K)_0$, colour with rotational rate, as proposed by Meyer et al. (1997).

4.5.3   Disc fractions

Disc fractions have been derived using infrared excesses previously in *JHK*, however recent works pre-dominantly use *Spitzer* IRAC magnitudes. Furthermore, MIPS magnitudes are used to identify so-called debris discs, where IR excesses are not apparent at shorter wavelengths. Finally, disc fractions have also been derived using the α criteria, where $\alpha = \frac{dlog\lambda F\lambda}{dlogF\lambda}$ between two limiting wavelengths, originally used to distinguish amongst Class I, II or II sources, but now used to detect disc presence (Lada et al. 2006; Kennedy & Kenyon 2009). An $\alpha >$-2 is used as a selection criterion for disc presence for TTS stars. We have constructed the α values for our model grid by adopting the limiting wavelengths of Kennedy & Kenyon (2009), namely 3.6 to 8.0 μm.
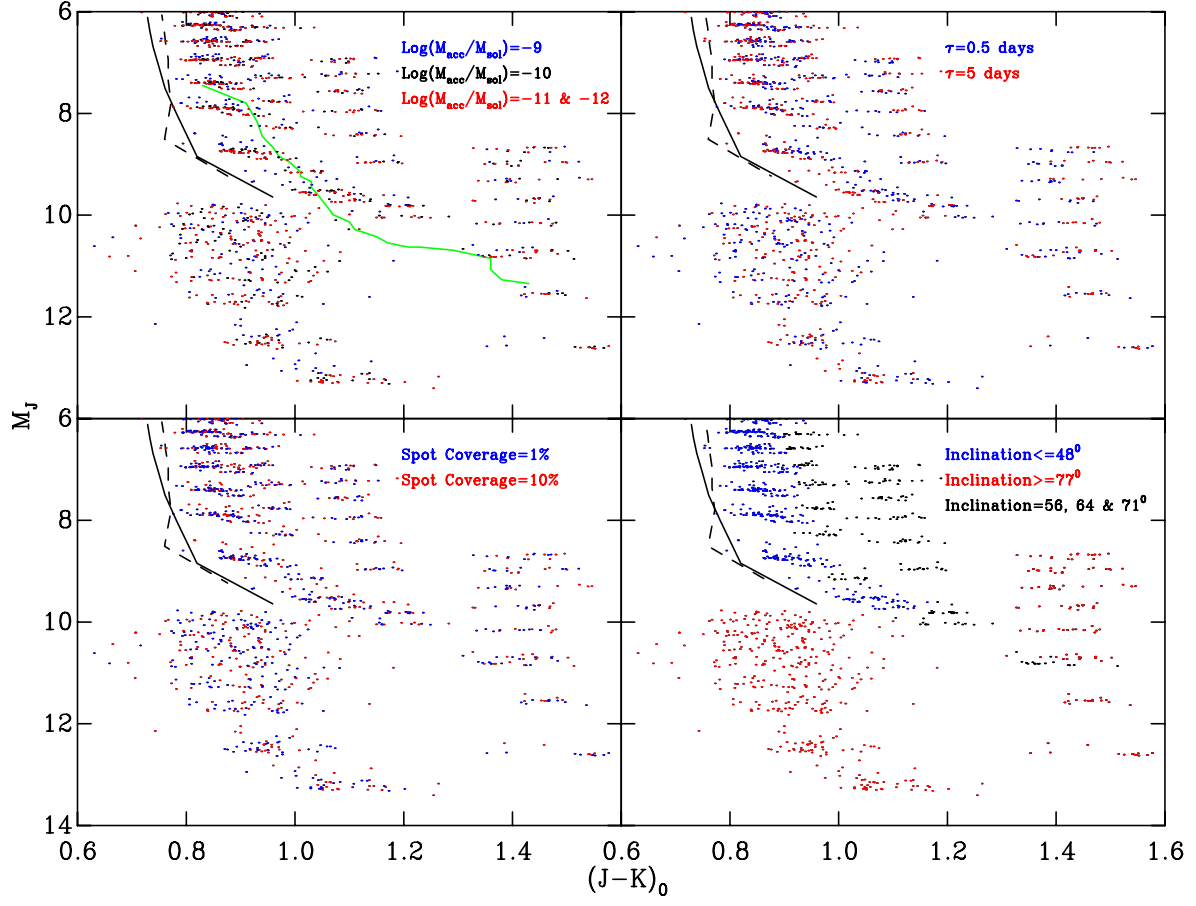
As shown in Figure 6, Section 4.1, the inner edge tem-

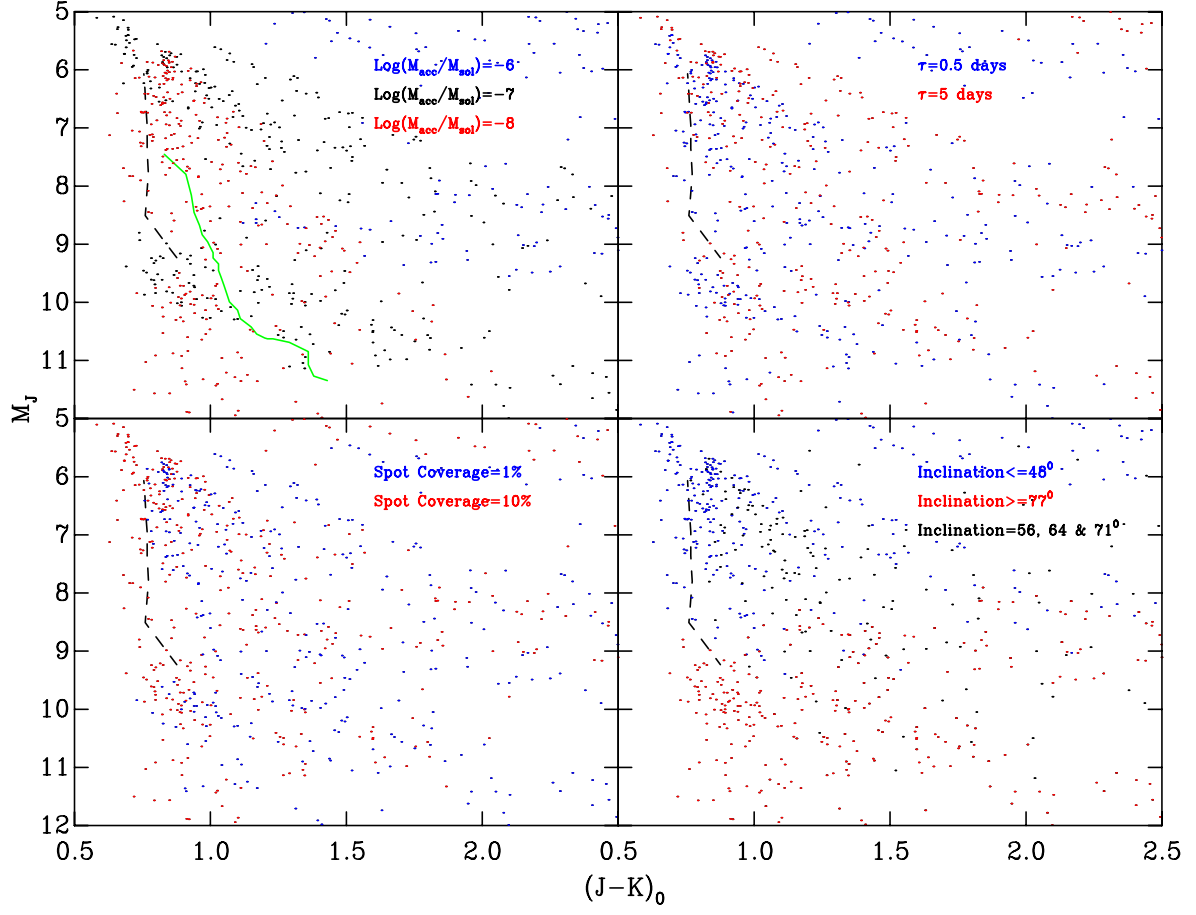**Figure 31.** As Figure 31, but in M_R, $(R − I)_0$, with the pre-MS isochrone omitted.

perature for typical accretors retains some correlation with rotation rate. In general the more slowly rotating objects having cooler inner edges. For the more extreme rotators the inner edge location is still weakly correlated with the inner edge temperature. In the extreme accretors case the correlation is caused by the radial fall in density, and therefore dust sublimation temperature as the inner edge is ablated. Therefore, for the extreme accretors the correlation between rotational period and inner edge temperature is lost. The inner edge temperature is in fact correlated with the flux and therefore accretion rate of the system. As shown in Figures 32 and 33 (in Section 4.5.1), there is no clear correlation in CMD position, and $(J − K)_0$ colour with rotation rate for either typical or extreme accretors. In fact any scatter in these Figures (32 and 33) appears to be most strongly correlated with accretion rate and inclination.

Figures 34 and 35 show the $(J−H)_0$, $(J−K)_0$ CoCoDs for typical and extreme accretors respectively. The dots are the simulate BDD systems for both ages (as position in these CoCoDs is not a strong function of age) and masses, and the black crosses the naked systems, again at both ages (and all masses), for the accretion rates matching the shown BDD data. The *panels* of these Figures then separate the BDD systems by accretion rate (*top left*), areal spot coverage (*bottom left*), rotational period (*top right*) and inclination (*bottom right*). The accretion rates of -9, -10 and -11 & -12 $\log(\frac{\dot{M}}{M_\odot}yr^{-1})$ are shown as blue, black and red dots respec-

tively in the *top left panel* of Figure 34. For Figure 35, the *top left panel* shows accretion rates of -6, -7 and -8 $\log(\frac{\dot{M}}{M_\odot}yr^{-1})$ are shown as blue, black and red dots respectively. The *bottom left panels* of both Figures 34 and 35 show the systems with areal spot coverages of 1 and 10% as blue and red dots respectively. The *top right panels* of both Figures 34 and 35 show the systems with rotational periods of 0.5 and 5 days as blue and red dots respectively. Finally, The *bottom right panels* of both Figures 34 and 35 show the systems with inclinations of $\theta \leqslant 48°$ as blue dots, $\theta > 56$ & $64°$ as black dots and $\theta \geqslant 71°$ as red dots.
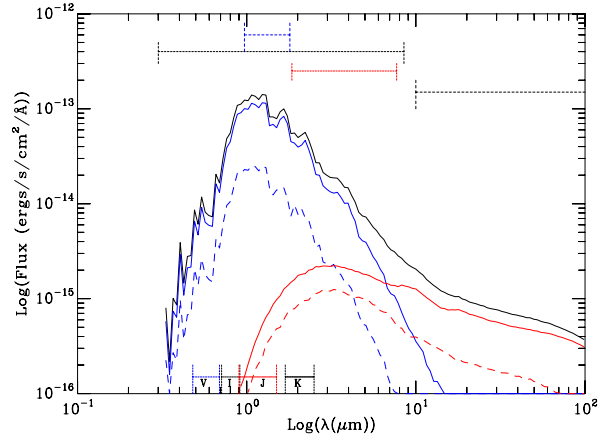
Figure 32. As Figure 29, in M_J, $(J - K)_0$, in this Figure the pre-MS isochrone of Siess et al. (2000), has been smoothed.

Figure 33. As for Figure 30, except that the -6 $\log(\frac{\dot{M}}{M_\odot}yr^{-1})$ isochrone is not shown (lies significantly blueward of locus of data), and the pre-MS isochrone has been smoothed.

Figures 34 and 35 show that for typical and extreme accretion rates there is no clear correlation of rotation rate, areal coverage or inclination with the position in the CoCoD. Significantly no clear correlation between IR colours and rotation rate can be observed for the typical accretors. This suggests that the weak correlation found between inner edge temperature and rotational period does not produce a matching correlation with IR colours. For the extreme accretors, however, a correlation between IR colours and accretion rate is clear. As the accretion rate increases the systems move to redder CoCoDs. This is caused, as discussed by the dust inner edge being sublimated and the resulting sublimation decreasing, with density, radially. Therefore, one can not extend the predictions of Meyer et al. (1997), after adoption of a co-rotation radius to suggest that IR excesses may be correlated with rotation rates, for typical or extreme accretors. As can be seen for all the panels of Figures 34 and 35 there is a slight overlap between the naked or disc less objects (crosses) and the BDD systems (dots). This overlap is small, only some of the lowest mass naked objects appear redward of the main population. Generally, a well placed cut should identify a large proportion of the disc candidates as is well known, if there is little complication from variable extinction and a well defined photometric system. However, the fact that an overlap exist at all will lead to some confusion as to the position of any disc excess cut. For real data a cut will be placed at a user identified paucity or gap in
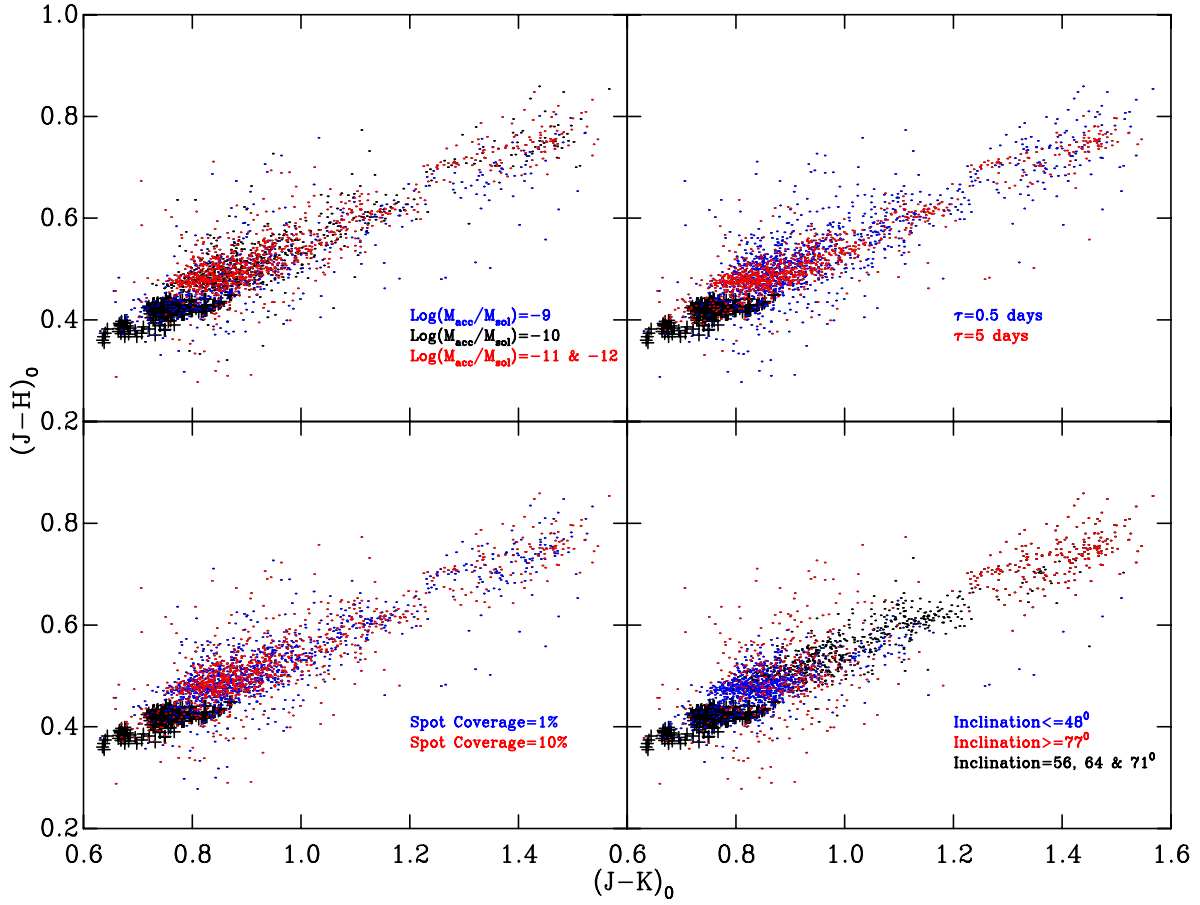

Figure 12. Figure showing the SED $\log(\lambda\mu m)$ against $\log(\text{flux})$, flux in $\text{ergs}/s/cm^2/\text{Å}$ for $M_* = 0.04 M_\odot$ at 1 Myr with an areal coverage of 10%, accretion rate of $\log \dot{M} = -10$ and rotation period of 0.5 days. The solid black line is the total simulated SED. The stellar components of the flux are shown in blue and the thermal in red, with direct emission appearing as solid lines and scattered photons as dashed lines. The vertical dotted bars linked by horizontal bars show the approximate (log) wavelength ranges of the luminosity components. With the blue lines denoting the accretion luminosity (L_{acc}) and the first (left to right) black lines showing the photospheric contribution (L_*). The final two sets of lines show the inner edge contribution (L_{wall}) in red and the outer disc (L_{disc}) in black. The vertical and horizontal dashed lines (in the *lower panels*) denote the approximate sensitivity ranges of our chosen V, I, J and K filters.

the CoCoD. Therefore, in practice, if any other region of the population appears equally, or more, sparse the cut is likely to be miss-placed. In practice these disc fractions are known to be lower limits of the true values, so ostensibly a miss placed cut, missing some disc candidates is not problematic.

The analysis in Section 4.5.1 and Figures 34 and 35, shows that accretion rate and inclination are the dominant variables controlling the photometric scatter, of the BDD systems. Therefore, for our subsequent analysis we will separate the systems using only these input variables.

Figures 36 and 37 show CoCoDs for colours constructed using simulated IRAC photometry, for the typical and extreme accreting systems respectively. These two Figures contain the same data as Figures 34 and 35, respectively. The naked systems are again shown as crosses and the BDD systems as dots. The *left panels* of these Figures show $([3.6]-[4.5])_0$, $([4.5]-[5.8])_0$ CoCoDs and the *right panels* $([3.6]-[4.5])_0$, $([5.8]-[8.0])_0$ CoCoDs. The *top panels* then show the accretion rates of -9, -10, -11 & -12 $\log(\frac{\dot{M}}{M_\odot}yr^{-1})$), for Figure 36, and -6, -7 and -8 $\log(\frac{\dot{M}}{M_\odot}yr^{-1})$), for Figure 37, as blue, black and red dots respectively. The *bottom panels* of both Figures show the systems with inclinations of $\theta \leqslant 48°$ as blue dots, $\theta > 56$ & $64°$ as black dots and $\theta \geqslant 71°$ as red dots.

Figure 36 and 37 show that the naked and BDD systems are well separated. Supporting the view that IRAC magnitudes are well suited for disc candidate identification. For the typical accretors there is a possible correlation between inclination and position in the $([3.6]-[4.5])_0$, $([5.8]-[8.0])_0$ CoCoD, (*bottom right panel* of Figure 36). The systems

Figure 34. Figure showing $(J-H)_0$, $(J-K)_0$ colour-colour diagram for typical accretors ($\dot{M} < leq$ -9 $\log(\frac{\dot{M}}{M_\odot}yr^{-1})$). The dots are then all models (at 1 and 10 Myrs) with discs and the black crosses are the naked systems, in *all panels*. The data are then separated by input variable in *each panel*. The *top left panel* shows accretion rates of -9, -10 and -11 & -12 $\log(\frac{\dot{M}}{M_\odot}yr^{-1})$ as blue, black and red dots respectively. The *top right panel* shows the systems with rotational periods of 0.5 and 5 days as blue and red dots respectively. The *bottom left panel* shows systems with areal spot coverages of 1 and 10% as blue and red dots respectively. Finally, the *bottom right panel* separates the systems into three groups inclination, $\theta \leqslant 48°$, $\theta \geqslant 77°$ and $\theta = 56, 64$ & $71°$, as blue, red and black dots respectively.
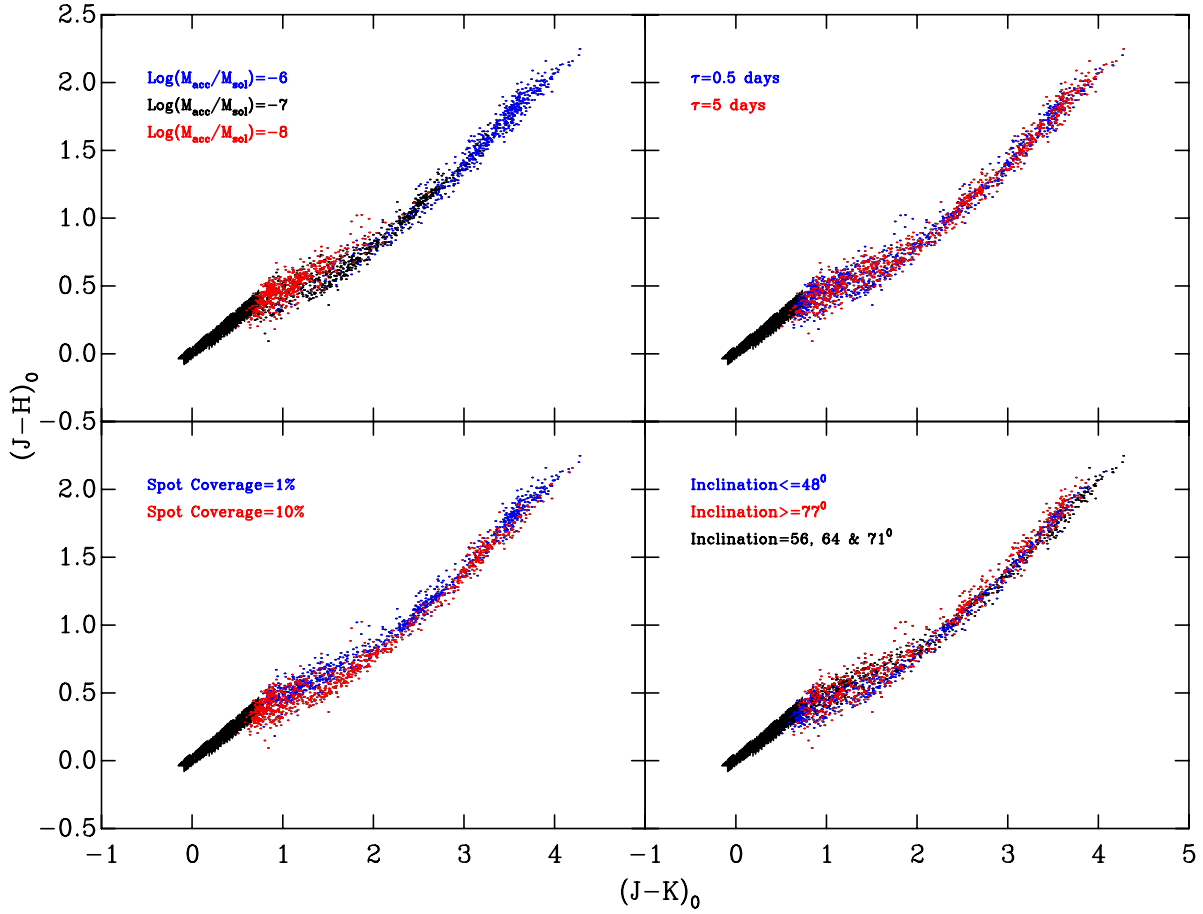
which are edge-on (i.e. $\theta \geqslant 77°$) appear closer in colour to the naked systems. In the case of extreme the accretors the separation between the naked and BDD systems is correlated with accretion rate for both CoCoDs (*top panels* of Figure 37). Effectively, as the accretion rate increases, in general the system moves to redder colours.

Figure 38 and 39, show the same data as Figure 36 and 37, in the same format and with the same notations. Figures 38 and 39 show CoCoDs of simulated photometry from IRAC and MIPS magnitudes. For both Figures the *left panels* show $([3.6]-[4.5])_0$, $([8.0]-24)_0$ and the *right panels* $([3.6]-[5.8])_0$, $([8.0]-24)_0$ CoCoD, where 24, is the $24\,\mu$m MIPS channel.

Figures 38 and 39 show that the BDD and naked systems are very well separated in CoCoDs utilising IRAC and longer wavelength MIPS data. For the systems with typical accretion rates, Figure 38, no correlation between CoCoD position and accretion rate is obvious (*top panels*). The *lower panels* of this Figure show that, in general, the locus of BDD stars is spread similarly for all but edge-on systems, which sometimes appear a little redder in $([8.0]-24)_0$. For the extreme accretors, Figure 39, however, correlations in CoCoD

position with both inclination and accretion rate are clear. The *top panels* of Figure 39 show that as the accretion rate increases, in general, the systems move to redders colours in $([3.6]-[4.5])_0$ or $([3.6]-[5.8])_0$ (*left* and *right panels* respectively). This is to be expected from our previous analysis of IRAC CoCoDs using this photometry. The *lower panels* of Figure 39 show a correlation of inclination angle with the colours in both axes. These two correlations essentially mean that we can roughly identify systems, with regard to inclination and accretion rate, by their position within this CoCoD. For instance, extreme accretors with lower accretion rates seen face-on will occupy the bottom left of the BDD locus, with edge-on systems with the maximum accretion rate appearing to the top right. Comparing the scales on Figures 38 and 39 shows that these systems slightly overlap, but in general the extreme accretors will lie redward of the typical accretor locus in both colours.

Figure 40 shows CoCoDs constructed solely from the longer wavelength MIPs photometry. Figure 40 shows the BDD data shown in previous Figures (such as Figure 36 and 37) in $(24-70)_0$, $(70-160)_0$ CoCoDs. The *left* and *right panels* show the typically and extreme accreting systems,

Figure 35. As for Figure 34 but for extreme accretors, $\dot{M} \geqslant$ -8 $\log(\frac{\dot{M}}{M_\odot} yr^{-1})$.
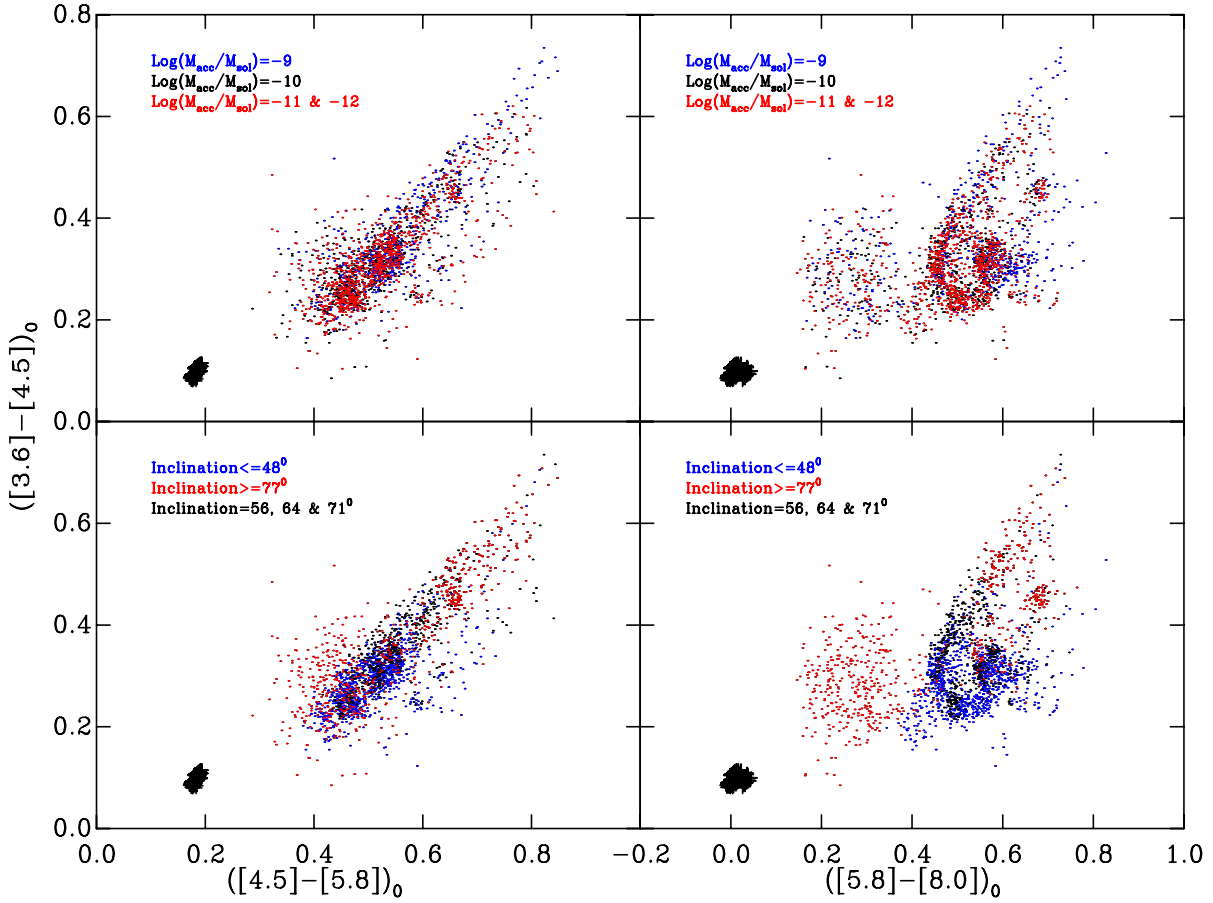
respectively. The *inset panels*, in *both top panels*, show larger areas to include the naked systems, as they are well removed from the BDD locus.

Figure 40 shows, in the *inset panels*, that BDD and naked systems are very well separated in CoCoDs constructed using MIPs photometry. For the typical accretors, *left panel*, the position within the CoCoD appears strongly correlated with inclination only, with the edge on systems moving away from the main BDD locus, as expected. For the extreme accretors, *right panel*, significantly more structure is apparent. In this case as the accretion rate increases the systems move redward in both colours. Additionally, as the inclination increases the systems move to redder $(24 - 70)_0$ colours. This suggests, as with Figure 39, for objects with extreme accretion rates, CoCoDs of this sort may help distinguish the characteristic inclination and accretion rate of the system. In practice, due to saturation and reddening effects and small sample sizes this may prove difficult. For our study this is interesting in that the fluxes for wavelengths longward of $24\,\mu m$ come from regions at temperatures of 120 K and below. This suggests that the outer disc flaring, as discussed in Section 4.1, leads to significantly structural changes in the outer, cooler disc, as a function of accretion rate. In addition, observing the separation of the naked and BDD systems within the CoCoDs it is clear that for sys-

tems within our grid, the best disc indicators are at longer wavelengths, as is well known from observations.

Disc fractions are also derived using the α value (Lada et al. 2006), essentially a slope of the SED between two wavelengths (at wavelengths longer than the stellar flux peak). Figure 41 shows the derived α values between 3.6 and 8.0 μm for our entire model grid (against an arbitrary model number), with dots showing BDD systems and crosses showing naked systems. The *left* and *right panels* of Figure 41 show the typical and extreme accreting systems respectively. For TTS $\alpha > -2$ distinguishes between systems with and without discs (Kennedy & Kenyon 2009). As can be seen in Figure 41 almost all the typical, and all of the extreme accreting BDD systems would be successfully identified using this criterion. Suggesting that the α value is a reliable disc indicator for BD systems. The *top panels* of Figure 41 show the alpha values separated by accretion rates, with -9, -10 and -11 & -12, or -6, -7 and -8 $\log(\frac{\dot{M}}{M_\odot} yr^{-1})$ shown as blue, black and red dots respectively. The *bottom panels* differentiate systems seen at different inclinations with $\theta \leqslant 48°$ as blue dots, $\theta > 56$ & $64°$ as black dots and $\theta \geqslant 71°$ as red dots.

Figure 41 shows that except for a few systems ($\frac{1}{50}$), all of which are typical accretors at edge-on inclinations, a cut of $\alpha > -2$ would identify all of our BDD systems. Furthermore, the *top left* panel shows that for typically accreting systems there would be no significant bias in selection with accretion

Figure 36. Figure showing typically accreting systems ($\dot{M} \leqslant -9 \log(\frac{\dot{M}}{M_\odot} yr^{-1})$), in irac photometric bands. The *left panels* show the $([3.6] - [4.5])_0$ against $([4.5] - [5.8])_0$ CoCoD, and the *right panels* show the $([3.6] - [4.5])_0$ against $([5.8] - [8.0])_0$ CoCoD. In *all panels* the dots are disc systems and crosses naked systems. The *top panels* then separate the systems by accretion rate with, -9, -10 and -11 & -12 $\log(\frac{\dot{M}}{M_\odot} yr^{-1})$ as blue, black and red dots respectively. The *bottom panels* separate the systems by inclination with $\theta \leqslant 48°$, $\theta \geqslant 77°$ and $\theta = 56, 64$ & $71°$, as blue, red and black dots respectively.

rate. The *bottom left panel* shows that the lowest α values are only apparent for the edge-on systems. The *right panels* of Figure 41, show that for extreme accretors the systems are well above the disc discriminator line, and move to greater α values with increasing accretion rate.

In summary, for our model grid, the best disc discriminators are MIPs CoCoDs and the α values. With, in general, correlations in position within the CoCoDs or the α values seen with accretion rate only for the extreme accretors.
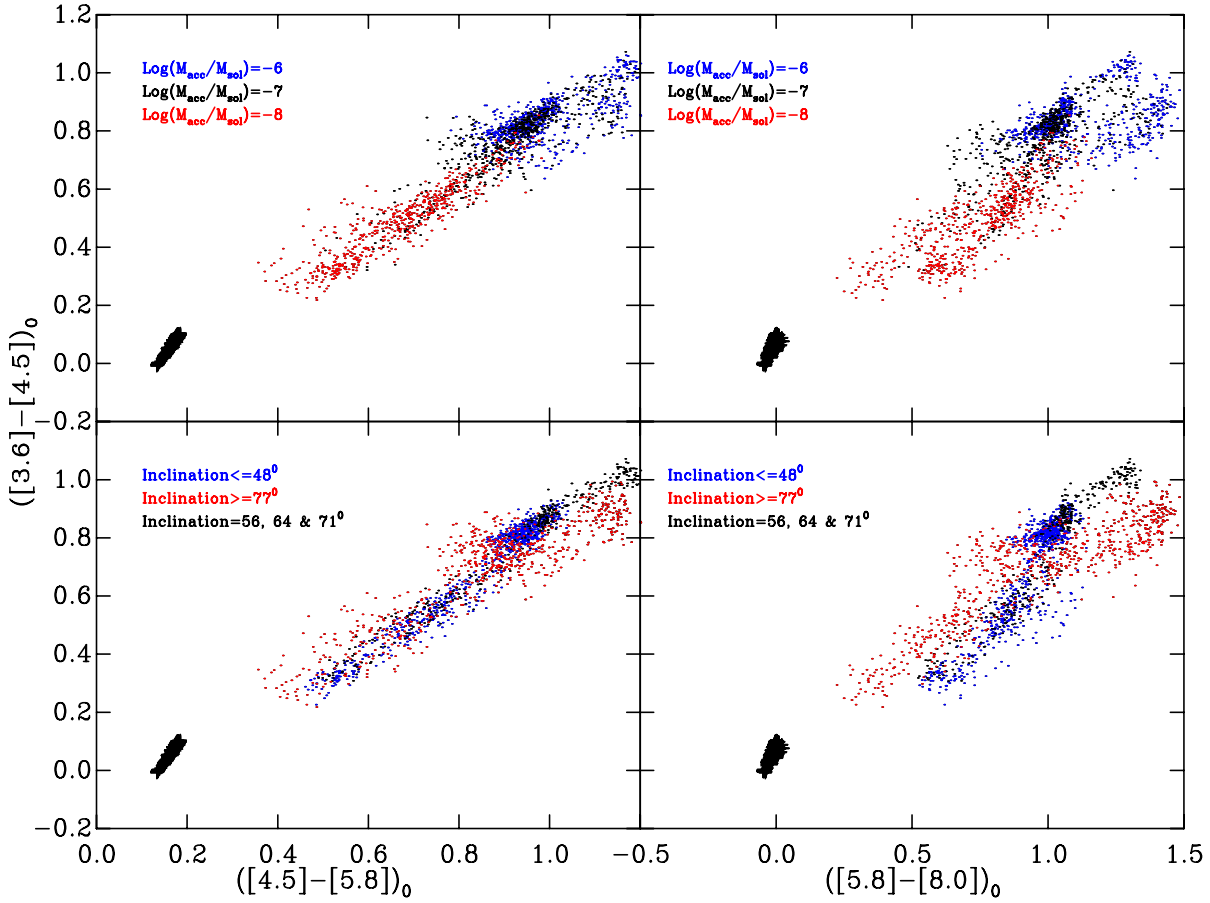
4.5.4 Practical Observations

Some recent studies of disc fractions for BD populations have used data from the *Spitzer* IRAC camera. Figures 42, 43 and 44 show the simulated photometry for our complete model grid. Naked BDs are shown as crosses and BDD systems as dots, with 1 and 10 Myrs data shown as blue and red dots respectively. The dashed lines are cuts used in three recent publications, Figure 42 is from Luhman et al. (2005) a study of IC348, Figure 43 from Luhman et al. (2008) a study of σ Orionis and Figure 44 a study of the Taurus region from Gutermuth et al. (2008). In these cases the effects

of extinction are either negligible in the plotted colours, with values of $E([3.6] - [4.5]) < 0.04$ and $E([4.5] - [5.8]) < 0.02$ for IC348 and $A_V \leqslant 4$ mag (which will be negligible in the IRAC CoCoD, Allen et al. 2004), or the cuts have been placed in intrinsic colour space as for σ Orionis.

As can be seen from Figures 42, 43 and 44 almost all of the disc systems from our simulated photometry would be correctly identified using these cuts. It is important to note that our conclusions so far have been drawn from differential photometric arguments, in this case we are using intrinsic colours and these values are extremely sensitive to changes in zero point and photometric calibration. Figure 42 shows that other than a few typically accreting systems the observational cut of Luhman et al. (2005) would select all of the BDD systems in our grid. Figure 43 shows that the cut of Luhman et al. (2008) would miss some typical and a very small number of extreme accreting BDD systems. Figure 44 shows only very few BDD systems will be missed. The number of BDD systems not identified for Figure 43 and 44 is larger than that of 42, but these Figures show that there is no preferential selection based on age. A comparison between Figure 43 and the *bottom right panel* of Figure 36, shows that all of the missed BDD systems are edge-on sys-

Figure 37. As for Figure 36 but for extreme accretors, $\dot{M} \geqslant$ -8 $\log(\frac{\dot{M}}{M_\odot} yr^{-1})$.

tems. Given, that extreme reddening may move naked stars into the BDD region selected, in general, dis fractions are usually quoted as lower limits. Therefore, a small number of miss-identified BDD system is a small effect. This allows us to conclude, that ubiquitously used BDD cuts used in IRAC CoCoDs are reliable when applied to our simulated dataset.

In a future publication we will release a fitting tool to be used in conjunction with the online database of naked and BDD systems (for both photometry and SED fitting). Therefore, we will be performing fits to observed systems using our grid. In this work we simply pick an example star and highlight its position in CMD and CoCoD space, compared to models covering the expected range of parameters. Natta et al. (2004) derive an accretion rate of -9 $\log(\frac{\dot{M}}{M_\odot} yr^{-1})$ for ρ Ophiucus 102. For this object Natta et al. (2002) find a spectral type of M6, T_{eff} of 2700 K, an extinction of A_V=3.0, a mass of M_* 0.04-0.08$M_\odot$ and a distance of 150pc. Photometry for ρ Ophiucus 102 is also published in Natta et al. (2006), in J, H and K. Additionally, R and I photometry has been published for this object in Wilking et al. (2005). We have adjusted our model spectra in the range M_*=0.04-0.08$M_\odot$, with accretion rates of -9 $\log(\frac{\dot{M}}{M_\odot} yr^{-1})$ (for all remaining input parameters) to the correct distance and reddening. Figure 45 shows, as dots, our BDD systems with the parameters in the range quoted, with ρ Ophiucus 102 is shown as a black star. The *panels* of Figure 45 then show
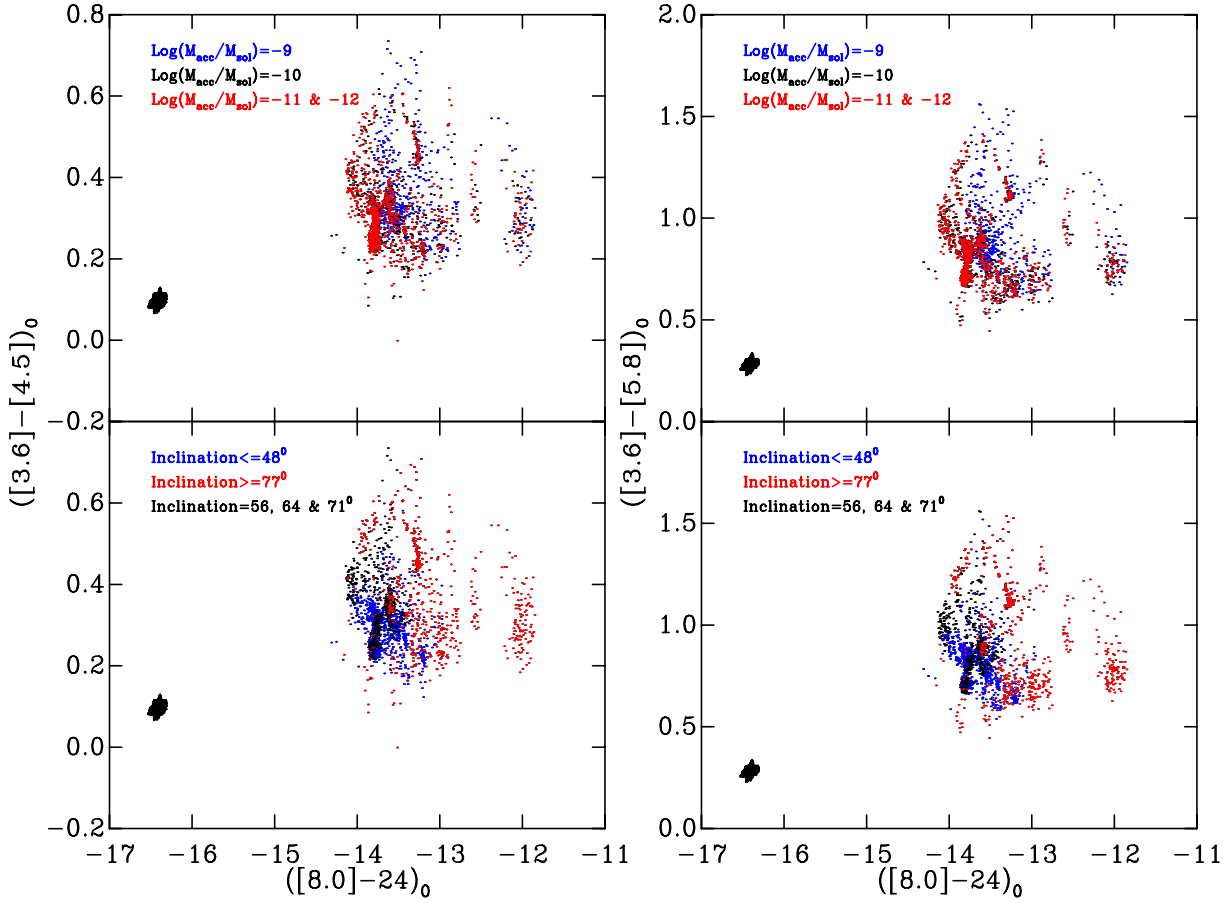
example CMDs and CoCoDs. The *top left panel* shows a J, $J - H$ CMD, the *bottom left panel* a R, $R - I$ CMD, the *top right panel* a J, $J - K$ CMD and finally, the *bottom right panel* a $J - K$, $J - H$ CoCoD.

We have not performed a formal fitting of the object ρ Ophiucus 102. However, qualitatively, Figure 45 shows that for ρ Ophiucus 102 the colours are well matched by our grid, yet the magnitude is somewhat brighter. This could be an indication of uncertainties in the distance to the object, reddening or magnitudes. A full investigation is beyond the scope of this paper, but, as stated in a future publication we will release an online fitting tool to be used in conjunction with our grid.

5   CONCLUSIONS

We have constructed a model grid of SEDs, and subsequently photometric magnitudes and colours, for actively accreting BDs with or without an associated accretion disc. We have modeled the photospheric flux from these BDs by adopting (and interpolating) the interior 'DUSTY00' models of Chabrier et al. (2000) combined with the 'AMES-Dusty', atmospheric models of Chabrier et al. (2000). We have then assumed that accretion occurs from an inner edge of a magnetically truncated accretion disc (truncated at the co-rotation radius). The accretion flux is calculated using a

Figure 38. Figure showing the ([3.6] − [4.5]), ([8.0] − 24) CMDs as the *left panels* and ([3.6] − [5.8]), ([8.0] − 24) CMDs as the *right panels*, combining IRAC and MIPS photometric channels. The systems are again separated by accretion rate and inclination angle in the *top* and *bottom* panels as in figure 36.
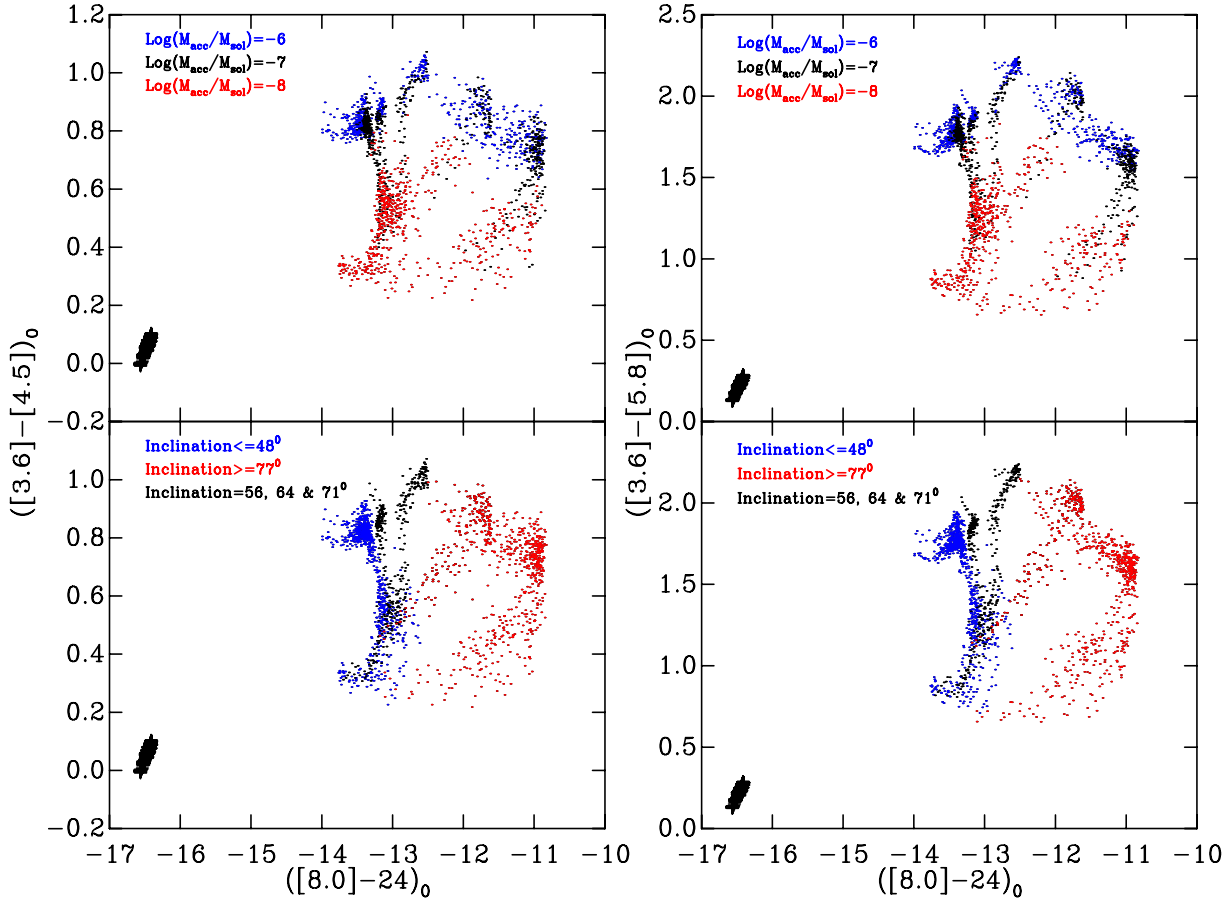
simple blackbody emission, given the derivation of a characteristic spot effective temperature. SEDs were then produced for both naked BDs and BDD systems. For the BDD systems we have modeled the disc using the TORUS radiative transfer code using the Lucy radiative transfer algorithm and incorporating dust sublimation and including a treatment of vertical hydrostatic equilibrium (see Section 2 for a discussion of the code). To produce a 'grid' of simulated systems we have varied several input parameters namely: stellar mass, stellar age, stellar rotation rate, accretion rate, the areal coverage of the accretion stream and the system inclination (the disc mass was fixed). The ranges of these variables were selected to represent and bound typical pre-MS BD systems, justification is provided using evidence from observational studies in Section 3 and a final list of the values of these variables can be found in Table 1.

Accepting our assumptions, parameter ranges and radiative transfer code our resulting simulated dataset has allowed us to qualitatively explore the effects of *active* (current not past accretion) accretion on disc structure. Furthermore through the simulation of observations we have explored the effects of accretion, and disc presence, on both the SEDs, and photometric colours and magnitudes of these systems.

As discussed in Section 4.1 vertical hydrostatic equilibrium, when applied to BDs, leads to increased flaring, when

compared to CTTS. This has previously been explored by Walker et al. (2004). However, in our study we have included a simple treatment of accretion. This leads to increased flaring as more flux reaches the outer disc, and subsequently lower opening angles for BDD systems with higher accretion rates. Furthermore, the addition of dust sublimation has shown that for BDD systems the inner disc location, temperature and vertical size & shape also varies with accretion rate. The inner edge position is correlated with temperature for the lower accreting models as suggested by Meyer et al. (1997). For the systems with higher accretion rates the inner edge temperature is weakly correlated with temperature, mainly due to the radial fall in density and therefore dust sublimation temperature. The inner disc edge, initially prescribed as a vertical wall, then becomes concave and finally convex as dust sublimation is increased (with increasing flux from higher rates of accretion).

Subsequently, the SEDs of BD systems with typical accretion rates and associated discs, are changed significantly from the assumed underlying photospheric model flux, and therefore become difficult to classify. In Section 4.2 we have shown that the BD photosphere becomes 'swamped' or overwhelmed by the accretion flux for rates of $\dot{M}$ >-9 $\log(\frac{\dot{M}}{M_\odot}yr^{-1})$. The outer disc flaring observed in the BDD systems was shown to cause occultation and a subsequent,

Figure 39. As for Figure 38 but for extreme accretors ($\dot{M} \geqslant$ -8 log($\frac{\dot{M}}{M_\odot} yr^{-1}$)).

sharp, fall in flux at an inclination which decreases for more systems with higher accretion rates. The thermal direct flux emanating from the disc inner edge was found to fall less dramatically with inclination for the systems with a curved inner boundary, as expected from the work of Tannirkulam et al. (2007).
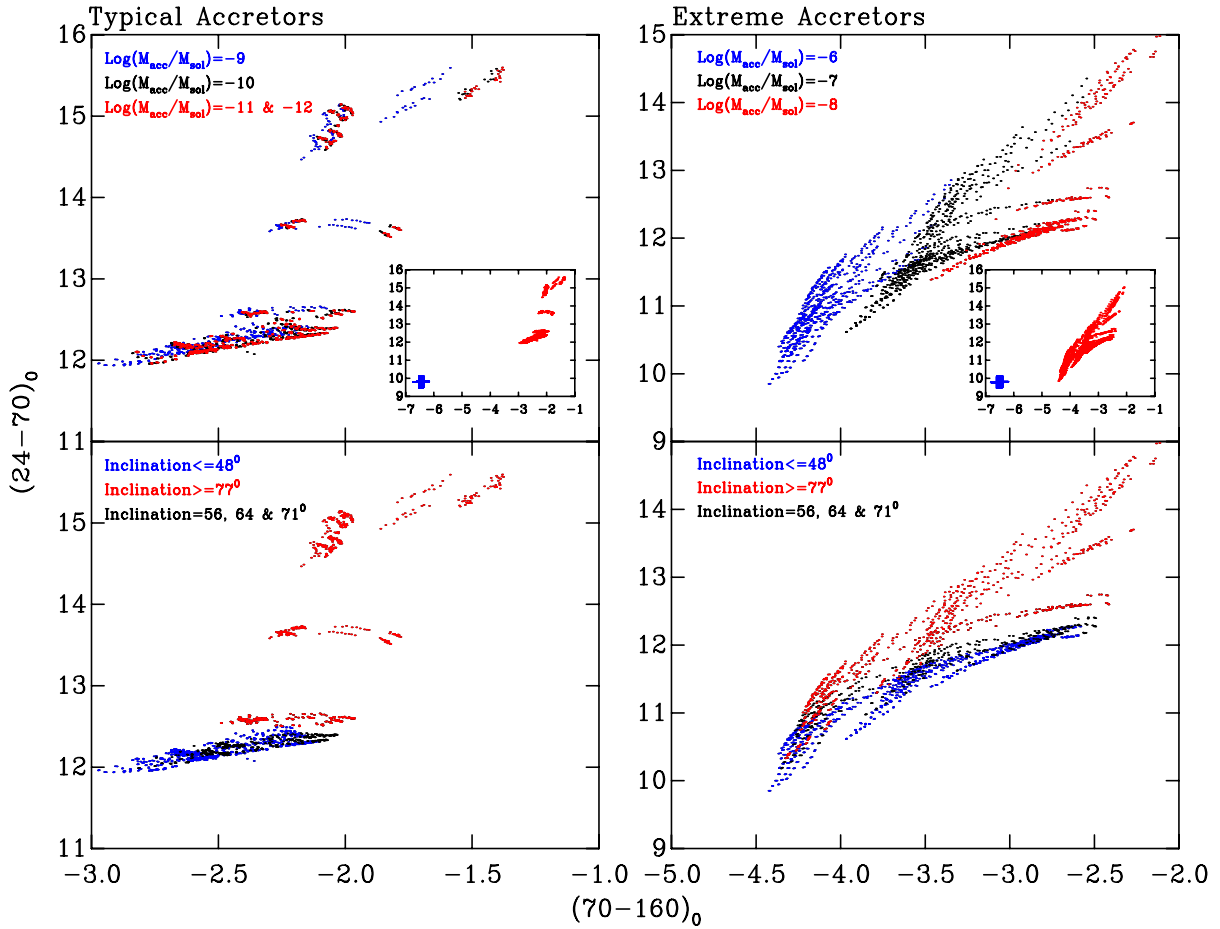
Subsequent derivation of photomertric magnitudes has allowed us to demonstrate that, as expected, increased accretion without disc presence, moves our naked systems to bluer and brighter magnitudes. Once a disc is added the increase in accretion flux interacts with the disc and does not necessarily lead to a simple motion toward brighter magnitudes and bluer colours. The increased flaring and obscuration present in BDD systems, over CTTS, leads to rapid falls in magnitude with inclination as an accretion (or flaring) dependent inclination. Furthermore, the disc inner edge leads to a shift redwards with increasing accretion rate as more flux is intercepted by the inner edge and the inner edge becomes convex and 'puffed up'. For more typically accreting BDD systems with vertical inner edges, the motion in a CMD, with inclination, is more disjointed.

In practice, however, most parameters for BDD systems are derived for populations. We have shown, in Section 4.3 that derivation of an *isochronal* (or photometric) age from our simulated photometry of a coeval BD sample, with typical accretion rates and associated circumstellar discs, would

be inaccurate and exceedingly difficult. Indeed, the resulting photometric colours and magnitudes could be indicative of a more distant redenned CTTS population. For more extreme accretion rates the scatter, in CMD space, is significantly far from the pre-MS locus and as such these stars have little chance of being selected as BDs. As discussed in Section 4 this does not include any effects due to past accretion on the evolution of the central star, which acts to accelerate the gravitational contraction and make the star appear older (Tout et al. 1999; Siess et al. 1999), further scattering the apparent age of a coeval population.

Concordantly, *isochronal* derivations of mass and therefore IMFs, for our simulated photometry, of a coeval population of accreting BDs with associated discs, would be inaccurate and problematic. Again caused by the changes in the SEDs as a result of the accretion flux and increased occultation by the larger degree of flaring seen in BD discs (for the latter, as found by Walker et al. 2004)

We have also qualitatively explored the effects of accretion and disc presence in our simulated dataset on disc fraction estimates. As is currently well known, longer wavelength bandpasses are much more reliable and suitable for disc identification. As shown in Section 4 the naked and BDD disc loci were much more clearly separated in the CoCoD constructed using *Spitzer* IRAC magnitudes than the shorter wavelength CIT *JHK* passbands. In addition,
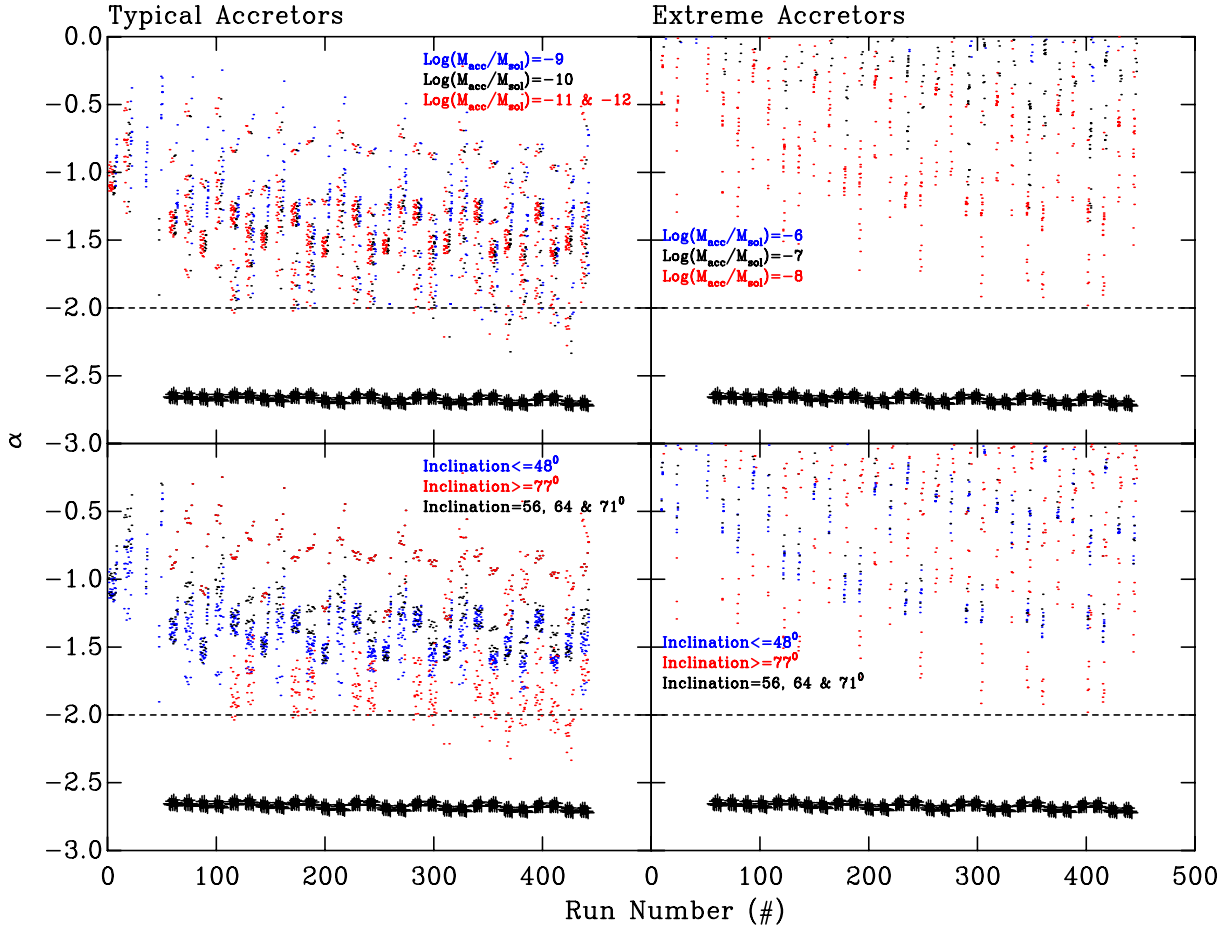
Figure 40. Figure showing CMDs of mips photometry for the typical ($\dot{M} \leqslant$ -9 $\log(\frac{\dot{M}}{M_\odot}yr^{-1})$) and extreme ($\dot{M} \geqslant$ -8 $\log(\frac{\dot{M}}{M_\odot}yr^{-1})$) accretors, as the *left panels* and *right panels* respectively. The *top panels* separate the systems by accretion rate in the way described in Figures 36 and 37 in the *left* and *right panels* respectively. The *bottom panels* then separate the systems by inclination as described in Figure 36. The *inset panels* in the *top panels* then show a larger region with the BDD systems as red dots and the naked systems as blue crosses.

we that the slope of the SED from 3.6 to 8.0 μm, or α value, is an effective disc indicator. We have also tentatively shown that current observational cuts, when applied to our simulated photometry (with its associated photometric system), results in the reliable detection of disc candidates, for IRAC and MIPS colours and α values, and therefore a robust lower limit disc fraction.

A further, derivative area this study impacts on, and perhaps most significantly, is the recent evidence for a stellar mass to accretion rate correlation, of the form: $M_{acc} \propto M_*^2$ (Muzerolle et al. 2003; Natta et al. 2004, 2006). This relationship has been extended into the BD mass regime in Natta et al. (2006). However, arguments based on selection and detection thresholds have already cast this relation into doubt (Clarke & Pringle 2006). As we have shown in Section 4 a relationship of this kind is self-reinforcing as lower mass objects with higher accretion rates have little chance of being correctly identified as such due to both the accretion flux and flared associated disc. Essentially, at present it is unclear how many BD stars are not included in this relationship due to misidentification. As explained in Walker et al. (2004), BD systems with a disc, without including accretion effects, can have the characteristics of higher mass

CTTS stars, due to increased disc flaring from a reduced surface gravity in the disc. The effects of accretion at typical or larger rates further exacerbate the situation both spectroscopically, as the photospheric flux essentially becomes swamped or completely veiled, and photometrically as the resulting colours and magnitudes are significantly shifted. Therefore, for our simulated dataset a relationship of this sort may well be derived, if typical methods are used to identify BD objects with discs and derive masses, ages and accretion rates, even though it is not present.

Finally, although inner edge locations are correlated with their temperature we do not find a resulting correlation with IR excess. As our initial inner edge locations are placed at the co-rotation radius one might expect a correlation between rotation rate and IR excess. This in turn might suggest that studies of disc presence correlation with slower rotation rates, exploring disc-locking, may have intrinsic biases. However, for our systems with dust sublimation, vertical flaring, accretion and view over a range of inclinations any correlation is not apparent. The study of Meyer et al. (1997) used analytical prescribed flat discs. Whether, any correlation is apparent for such systems using our models is studied in an upcoming paper where we introduce a fitting

Figure 41. Figure showing α value (Lada et al. 2006) (against an arbitrary model number) used Kennedy & Kenyon (2009), $\alpha = \frac{dlog(\lambda F_\lambda)}{dlog(\lambda)}|_{8.0}^{3.6}$ (λ in μm). Crosses show the simulated objects without discs and dots are those with circumstellar disc, the horizontal line is the $\alpha > -2$ cut used to identify disc candidates for solar type stars in Kennedy & Kenyon (2009). Note, that stars of $M_* < 0.01 M_\odot$ are not included due to unreliable flux estimates, in the atmosphere models, for longer wavelengths ($\lambda > 4\,\mu$m). The *left panels* show typical ($\dot{M} \leqslant -9 \log(\frac{\dot{M}}{M_\odot} yr^{-1})$) accretors and the *right panels* the extreme ($\dot{M} \geqslant -8 \log(\frac{\dot{M}}{M_\odot} yr^{-1})$) accretors. The *top panels* separate the systems by accretion rate in the way described in Figures 36 and 37 in the *left* and *right panels* respectively. The *bottom panels* then separate the systems by inclination as described in Figure 36.

tool to be used with the model grid and release a further set of models with analytic disc structures, and an increased parameter space.

5.1 Summary

In summary, our simulated dataset shows that for typical parameter ranges for BD stars and BDD systems, disc presence and accretion flux lead to:

Difficulty deriving the following stellar parameters for a coeval population:

- Isochronal ages
- Isochronal masses
- IMFs

And we have shown:

- *Spitzer* IRAC magnitudes are required for reliable disc identification
- An expected correlation in inner disc edge with IR excess does not occur for systems with dust sublimation and
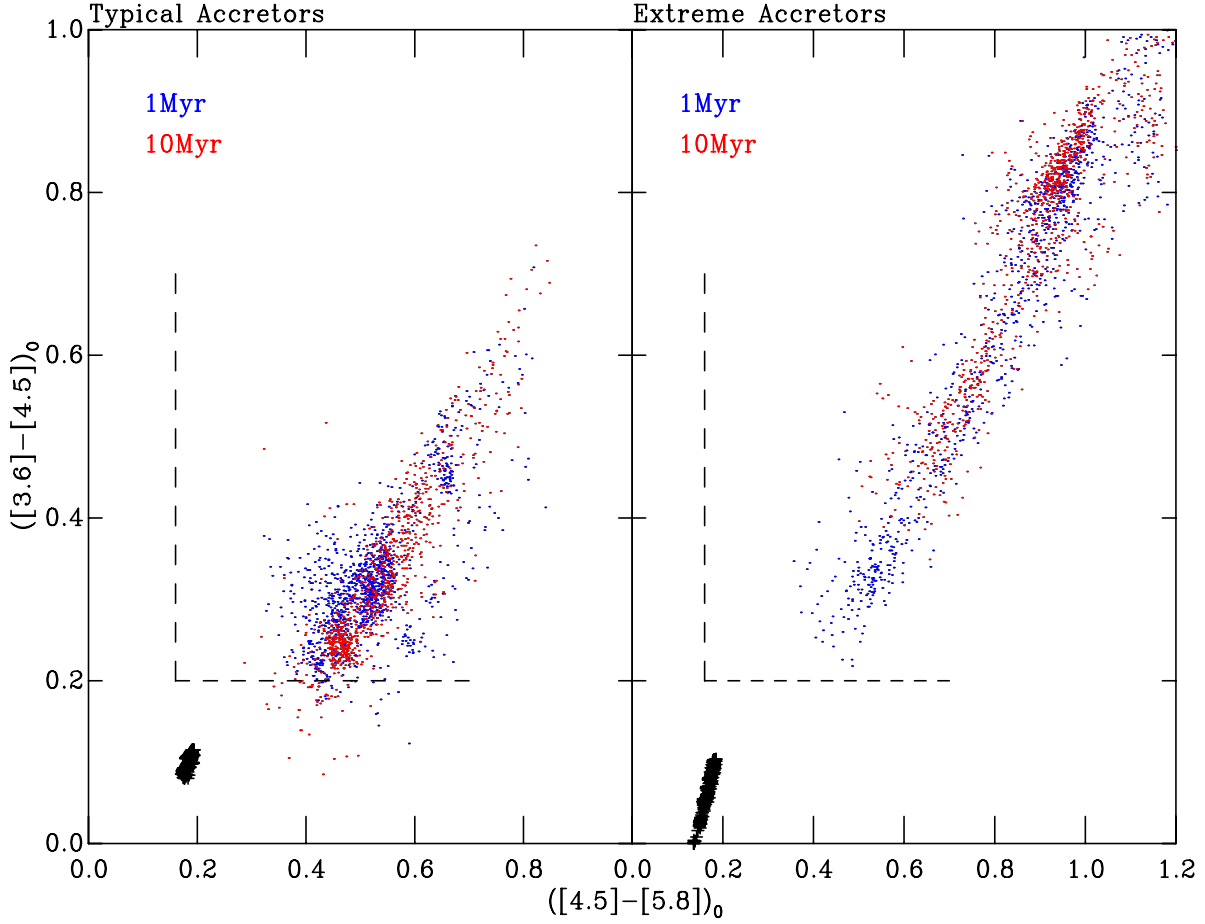
vertical hydrostatic equilibrium view over a range of inclinations.

- Low mass, high accretion rate systems are likely to be misidentified and therefore not included in any study relating $M_* \propto \dot{M}$
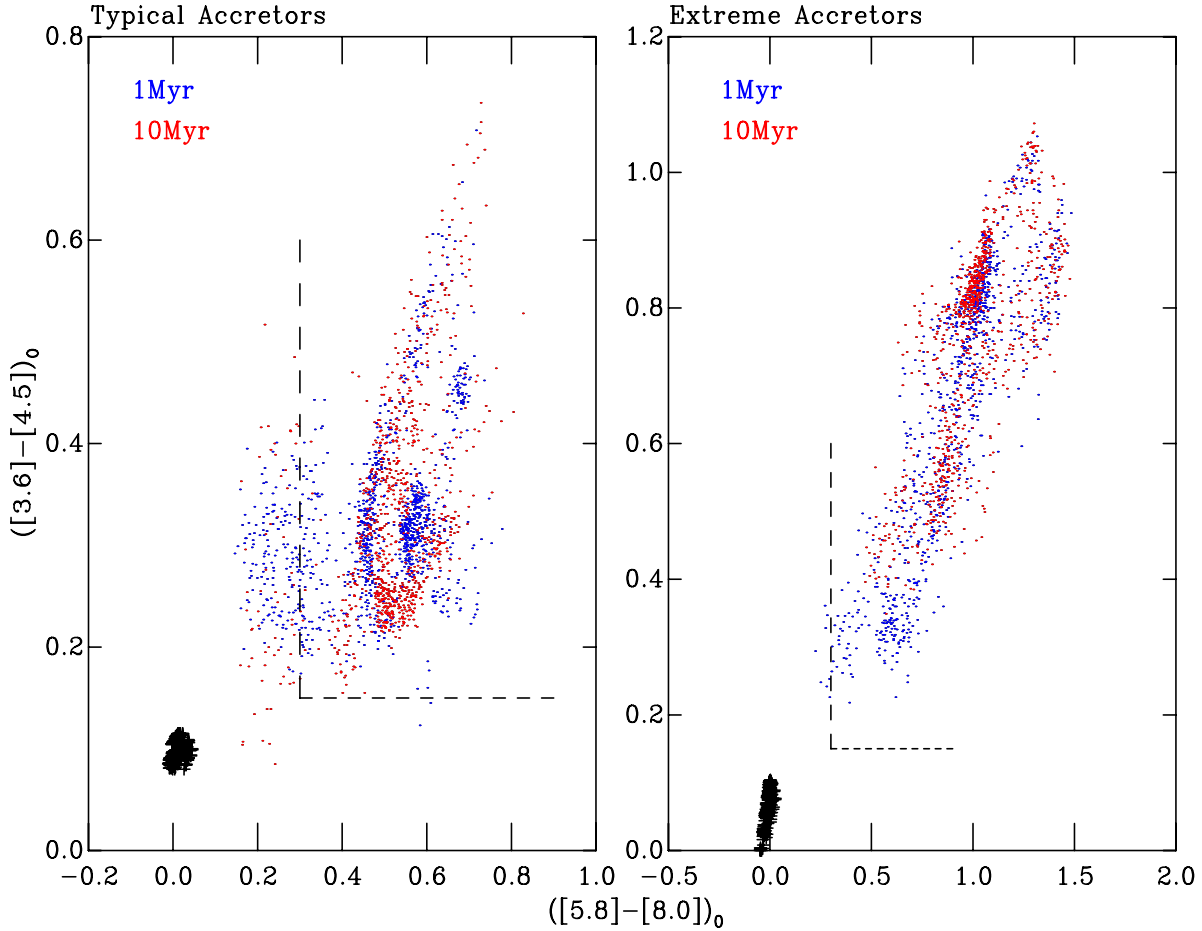
REFERENCES

Allen L. E., Calvet N., D'Alessio P., Merin B., Hartmann L., Megeath S. T., Gutermuth R. A., Muzerolle J., Pipher J. L., Myers P. C., Fazio G. G., 2004, ApJS, 154, 363

Allers K. N., Kessler-Silacci J. E., Cieza L. A., Jaffe D. T., 2006, ApJ, 644, 364

Anders E., Grevesse N., 1989, Geochim. Cosmochim. Acta, 53, 197

Asplund M., Grevesse N., Sauval A. J., 2006, Communications in Asteroseismology, 147, 76

Bertout C., Harder S., Malbet F., Mennessier C., Regev O., 1996, AJ, 112, 2159

Figure 42. Figure showing all simulated photometry for the entire studied parameter range at ages 1Myr and 10Myr as dots (blue and red respectively), and the naked photometry as crosses. The dashed lines are a recent BD disc excess cuts used in Luhman et al. (2005) for IC348 at a nominal age of 3-4Myr Mayne & Naylor (2008). It must be noted that the naked stars of $M = 0.01 M_\odot$ are not included in this figure as their SEDs do not extend far enough into the IRAC passbands to derive reliable colours. The *left panel* shows the typical ($\dot{M} \leqslant$ -9 $\log(\frac{\dot{M}}{M_\odot} yr^{-1})$) accretors and the *right panel* the extreme ($\dot{M} \geqslant$ -8 $\log(\frac{\dot{M}}{M_\odot} yr^{-1})$) accretors.

Bessell M. S., 2000, PASP, 112, 961

Bessell M. S., 2005, ARA&A, 43, 293

Bessell M. S., Brett J. M., 1988, PASP, 100, 1134

Bessell M. S., Castelli F., Plez B., 1998, A&A, 333, 231

Bouvier J., Alencar S. H. P., Harries T. J., Johns-Krull C. M., Romanova M. M., 2007, in Reipurth B., Jewitt D., Keil K., eds, Protostars and Planets V Magnetospheric Accretion in Classical T Tauri Stars. pp 479–494

Bouvier J., Covino E., Kovo O., Martin E. L., Matthews J. M., Terranegra L., Beck S. C., 1995, A&A, 299, 89

Bouy H., Huélamo N., Pinte C., co authors. ., 2008, A&A, 486, 877

Camenzind M., 1990, in Klare G., ed., Reviews in Modern Astronomy Vol. 3 of Reviews in Modern Astronomy, Magnetized Disk-Winds and the Origin of Bipolar Outflows.. pp 234–265

Chabrier G., Baraffe I., Allard F., Hauschildt P., 2000, ApJ, 542, 464

Clarke C. J., Pringle J. E., 2006, MNRAS, 370, L10

Cohen M., Walker R. G., Barlow M. J., Deacon J. R., Witteborn F. C., Carbon D., Augason G., 1993, in Kwok S., ed., Astronomical Infrared Spectroscopy: Future Observational Directions Vol. 41 of Astronomical Society of the

Pacific Conference Series, Absolute Spectrally Continuous Stellar Irradiance Calibration in the Infrared. pp 55–+

Cohen M., Wheaton W. A., Megeath S. T., 2003, AJ, 126, 1090

Dahm S. E., Carpenter J. M., 2009, ArXiv e-prints

Dullemond C. P., Dominik C., Natta A., 2001, ApJ, 560, 957

Eisner J. A., Hillenbrand L. A., White R. J., Akeson R. L., Sargent A. I., 2005, ApJ, 623, 952

Elias J. H., Frogel J. A., Matthews K., Neugebauer G., 1982, AJ, 87, 1029

Ercolano B., Clarke C. J., Robitaille T. P., 2009, ArXiv e-prints

Fukugita M., Ichikawa T., Gunn J. E., Doi M., Shimasaku K., Schneider D. P., 1996, AJ, 111, 1748

Gullbring E., Hartmann L., Briceno C., Calvet N., Muzerolle J., 1998, in Donahue R. A., Bookbinder J. A., eds, Cool Stars, Stellar Systems, and the Sun Vol. 154 of Astronomical Society of the Pacific Conference Series, Color Anomalies of Weak Lined T Tauri stars. pp 1709–+

Gutermuth R. A., Myers P. C., Megeath S. T., Allen L. E., Pipher J. L., Muzerolle J., Porras A., Winston E., Fazio G., 2008, ApJ, 674, 336
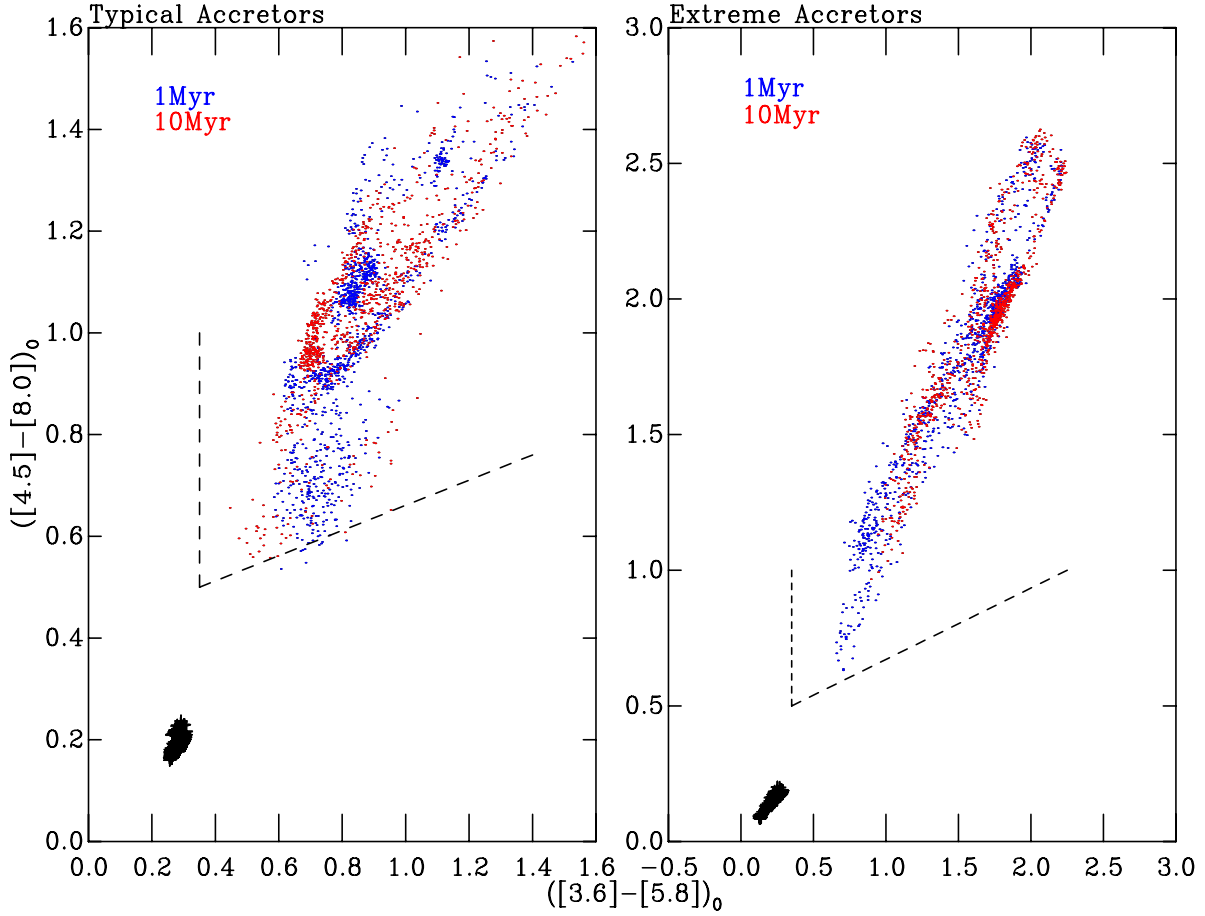
Figure 43. Figure showing an observational cut used in Luhman et al. (2008) for data of the σ Orionis cluster. It must be noted that the naked stars of $M = 0.01 M_\odot$ are not included in this figure as their SEDs do not extend far enough into the IRAC passbands to derive reliable colours. The systems are separated by age as described in Figure 42. The *left* and *right panels* again show the typical ($\dot{M} \leqslant$ -9 $\log(\frac{\dot{M}}{M_\odot} yr^{-1})$) and extreme ($\dot{M} \geqslant$ -8 $\log(\frac{\dot{M}}{M_\odot} yr^{-1})$) accretors respectively as in Figure 42.

Haisch Jr. K. E., Lada E. A., Lada C. J., 2001, ApJL, 553, L153

Harries T. J., 2000, MNRAS, 315, 722

Harries T. J., Monnier J. D., Symington N. H., Kurosawa R., 2004, MNRAS, 350, 565

Hartmann L., 1998, Accretion Processes in Star Formation. Accretion processes in star formation / Lee Hartmann. Cambridge, UK ; New York : Cambridge University Press, 1998. (Cambridge astrophysics series ; 32) ISBN 0521435072.

Hawarden T. G., Leggett S. K., Letawsky M. B., Ballantyne D. R., Casali M. M., 2001, MNRAS, 325, 563

Herbst W., Eislöffel J., Mundt R., Scholz A., 2007, in Reipurth B., Jewitt D., Keil K., eds, Protostars and Planets V The Rotation of Young Low-Mass Stars and Brown Dwarfs. pp 297–311

Herczeg G. J., Cruz K. L., Hillenbrand L. A., 2009, ArXiv e-prints

Holland W. S., Robson E. I., Gear W. K., Cunningham C. R., Lightfoot J. F., Jenness T., Ivison R. J., Stevens J. A., Ade P. A. R., Griffin M. J., Duncan W. D., Murphy J. A., Naylor D. A., 1999, MNRAS, 303, 659

Isella A., Natta A., 2005, A&A, 438, 899

Jayawardhana R., Ardila D. R., Stelzer B., Haisch Jr. K. E.,

2003, AJ, 126, 1515

Joergens V., Fernández M., Carpenter J. M., Neuhäuser R., 2003, ApJ, 594, 971

Johnson H. L., 1966, ARA&A, 4, 193

Kennedy G. M., Kenyon S. J., 2009, ArXiv e-prints

Koenigl A., 1991, ApJL, 370, L39

Lada C. J., Muench A. A., Luhman K. L., Allen L., Hartmann L., Megeath T., Myers P., Fazio G., Wood K., Muzerolle J., Rieke G., Siegler N., Young E., 2006, AJ, 131, 1574

Leggett S. K., 1992, ApJS, 82, 351

Lucy L. B., 1999, A&A, 344, 282

Luhman K. L., Hernández J., Downes J. J., Hartmann L., Briceño C., 2008, ApJ, 688, 362

Luhman K. L., Lada C. J., Hartmann L., Muench A. A., Megeath S. T., Allen L. E., Myers P. C., Muzerolle J., Young E., Fazio G. G., 2005, ApJL, 631, L69

Mayne N. J., Naylor T., 2008, MNRAS, 386, 261

Mayne N. J., Naylor T., Littlefair S. P., Saunders E. S., Jeffries R. D., 2007, MNRAS, 375, 1220

Meyer M. R., Calvet N., Hillenbrand L. A., 1997, AJ, 114, 288

Mohanty S., Jayawardhana R., Natta A., Fujiyoshi T., Tamura M., Barrado y Navascués D., 2004, ApJL, 609,
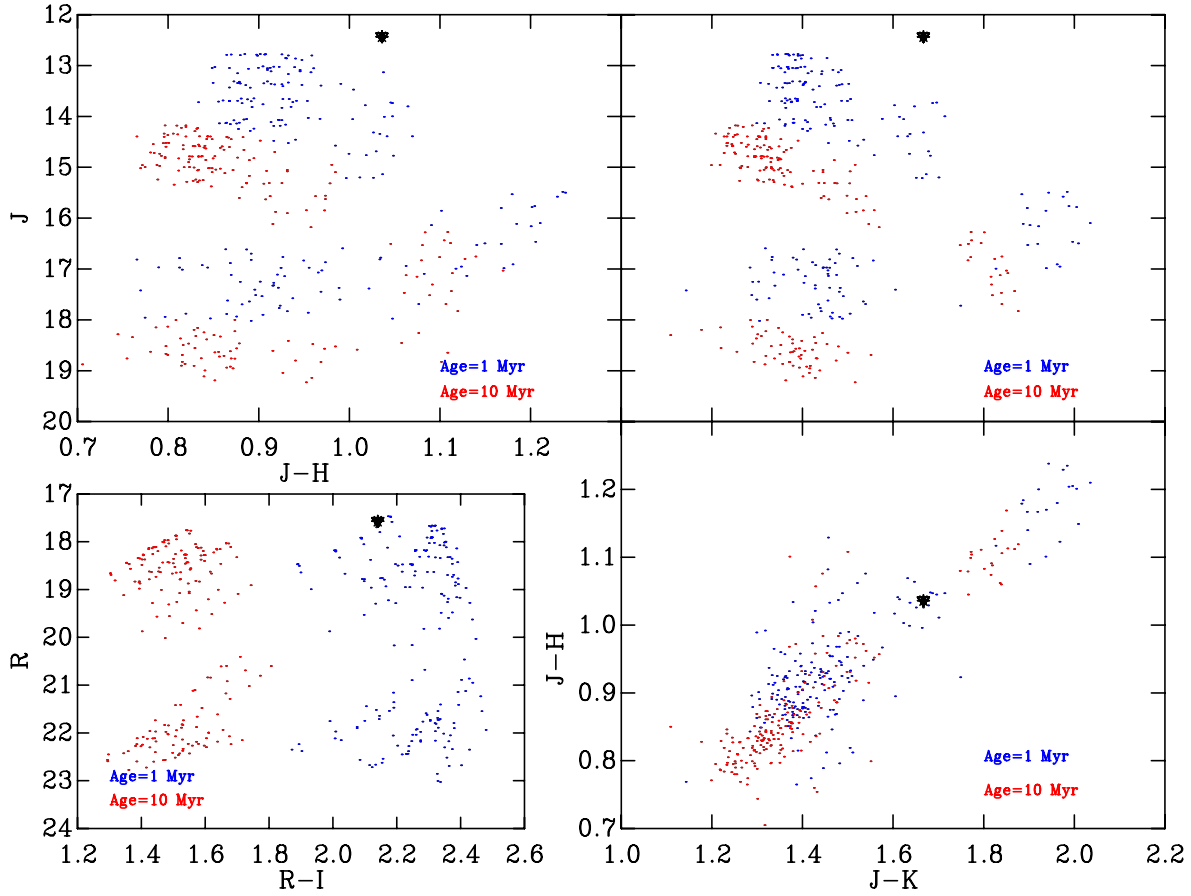
Figure 44. Figure showing an observational cut used in Monin et al. (2010) for data of the Taurus cloud. The criteria applied for BDD system selection are that of Gutermuth et al. (2008). It must be noted that the naked stars of $M = 0.01 M_\odot$ are not included in this figure as their SEDs do not extend far enough into the IRAC passbands to derive reliable colours. The systems are separated by age as described in Figure 42. The *left* and *right panels* again show the typical ($\dot{M} \leqslant$ -9 $\log(\frac{\dot{M}}{M_\odot} yr^{-1})$) and extreme ($\dot{M} \geqslant$ -8 $\log(\frac{\dot{M}}{M_\odot} yr^{-1})$) accretors respectively as in Figure 42.

L33

Mohanty S., Shu F. H., 2008, ApJ, 687, 1323

Monin J., Guieu S., Pinte C., Rebull L., Goldsmith P., Fukagawa M., Ménard F., Padgett D., Stappelfeld K., Mc-Cabe C., Carey S., Noriega-Crespo A., Brooke T., Huard T., Terebey S., Hillenbrand L., Guedel M., 2010, ArXiv e-prints

Morrow A. L., Luhman K. L., Espaillat C., D'Alessio P., Adame L., Calvet N., Forrest W. J., Sargent B., Hartmann L., Watson D. M., Bohac C. J., 2008, ApJL, 676, L143

Muzerolle J., Hillenbrand L., Calvet N., Briceño C., Hartmann L., 2003, ApJ, 592, 266

Muzerolle J., Luhman K. L., Briceño C., Hartmann L., Calvet N., 2005, ApJ, 625, 906

Najita J. R., Strom S. E., Muzerolle J., 2007, MNRAS, 378, 369

Natta A., Testi L., Comerón F., Oliva E., D'Antona F., Baffa C., Comoretto G., Gennari S., 2002, A&A, 393, 597

Natta A., Testi L., Muzerolle J., Randich S., Comerón F., Persi P., 2004, A&A, 424, 603

Natta A., Testi L., Randich S., 2006, A&A, 452, 245

Neugebauer G., Habing H. J., van Duinen R., co authors ., 1984, ApJL, 278, L1

Noels A., Grevesse N., 1993, in Weiss W. W., Baglin A., eds, IAU Colloq. 137: Inside the Stars Vol. 40 of Astronomical Society of the Pacific Conference Series, Small and intermediate mass stellar evolution - Main sequence and close to it. pp 410–425

Pascucci I., Apai D., Luhman K., Henning T., Bouwman J., Meyer M., Lahuis F., Natta A., 2008, ArXiv e-prints

Pollack J. B., Hollenbach D., Beckwith S., Simonelli D. P., Roush T., Fong W., 1994, ApJ, 421, 615

Rice W. K. M., Wood K., Armitage P. J., Whitney B. A., Bjorkman J. E., 2003, MNRAS, 342, 79

Robitaille T. P., Whitney B. A., Indebetouw R., Wood K., Denzmore P., 2006, ApJS, 167, 256

Scholz A., Eislöffel J., 2004, A&A, 419, 249

Scholz A., Eislöffel J., 2005, A&A, 429, 1007

Shakura N. I., Syunyaev R. A., 1973, A&A, 24, 337

Shu F., Najita J., Ostriker E., Wilkin F., Ruden S., Lizano S., 1994, ApJ, 429, 781

Siess L., Dufour E., Forestini M., 2000, A&A, 358, 593

Siess L., Forestini M., Bertout C., 1999, A&A, 342, 480

Simons D. A., Tokunaga A., 2002, PASP, 114, 169

Skrutskie M. F., Cutri R. M., Stiening R., co authors ., 2006, AJ, 131, 1163

Figure 45. Figure showing CMDs and CoCoDs of systems with matching parameters to ρ Ophiucus 102 from Natta et al. (2002). The object ρ Ophiucus 102 is shown in *all panels* as a black star, the BDD systems are the separated by age, with the 1 and 10 Myr systems appearing as blue and red dots respectively. The *top left panel* shows a J, $J - H$ CMD, the *top right panel* a J, $J - K$ CMD, the *bottom left panel* a R, $R - I$ CMD and the *bottom right panel* shows a $J - H$, $J - K$ CoCoD.

Stephens D. C., Leggett S. K., 2004, PASP, 116, 9

Tannirkulam A., Harries T. J., Monnier J. D., 2007, ApJ, 661, 374

Tannirkulam A., Monnier J. D., Harries T. J., Millan-Gabet R., Zhu Z., Pedretti E., Ireland M., Tuthill P., ten Brummelaar T., McAlister H., Farrington C., Goldfinger P. J., Sturmann J., Sturmann L., Turner N., 2008, ApJ, 689, 513

Tokunaga A. T., Simons D. A., Vacca W. D., 2002, PASP, 114, 180

Tout C. A., Livio M., Bonnell I. A., 1999, MNRAS, 310, 360

Walker C., Wood K., Lada C. J., Robitaille T., Bjorkman J. E., Whitney B., 2004, MNRAS, 351, 607

White R. J., Basri G., 2003, ApJ, 582, 1109

Wilking B. A., Meyer M. R., Robinson J. G., Greene T. P., 2005, AJ, 130, 1733

Wood K., Wolff M. J., Bjorkman J. E., Whitney B., 2002, ApJ, 564, 887

Zapatero Osorio M. R., Béjar V. J. S., Pavlenko Y., Rebolo R., Allende Prieto C., Martín E. L., García López R. J., 2002, A&A, 384, 937

APPENDIX A: CONSISTENCY CHECKS AND PROBLEMS

Firstly, a check was made on the photospheric input flux and the resulting stellar direct flux (tagged by TORUS) after the radiative transfer simulation. The resulting flux distributions should match most closely for face-on configurations, and then match in shape only, with the stellar direct flux level dropping towards higher inclinations, as more photons are scattered and absorbed by the disc.

We also directly compared the magnitudes and colours of our naked BD systems with the lowest accretion rate (-12 $\log(\frac{\dot{M}}{M_\odot}yr^{-1})$) to those published in Chabrier et al. (2000), in the same photometric system (CIT). We found significant colour differences ($\delta(J-K) \leqslant 0.1$), between our derived values and those of Chabrier et al. (2000). As a further check we derived the magnitudes in the Bessell et al. (1998) system (by both adopting the published zero points, and by using a Vega reference spectrum), and applied conversions of Leggett (1992)[6], to the CIT system. For each method we failed to match the magnitudes and colours published in

---

[6] We have also included the wavelength shift mention in Stephens & Leggett (2004)

Chabrier et al. (2000). As a final test we passed the downloaded, unaltered, atmospheric spectra directly through the filter response program, without interpolation, for the closest matches in log(g) and $T_{\rm eff}$ from the interior models published in Chabrier et al. (2000). These magnitudes and colours also failed to match. Therefore, we must conclude that the most likely cause of the mismatch is due to improvements in the model atmospheres available online [7] (this is likely as the models available online, have a later time stamp, $\approx$ 2005 compared to 2000). For the final published magnitudes, for the naked systems, we have used a similar wavelength resolution as in our BDD systems, i.e. 200 logarithmically spaced points. This means that magnitudes derived from these spectra will differ slightly from those derived from the full spectra, but this effect is negligible, and increased resolution for only some of our model grid (i.e naked stars) will hamper comparison between the models.

The final test of the derived colours and magnitudes was a comparison of the naked systems with the results for the almost face-on BDD systems. The results for the optical passbands should be similar and an appraisal of the component SED, i.e. showing the stellar direct flux, as can be seen in Figure 12.

We have adopted zeropoints derived using a Vega reference spectrum for the optical and near-IR passbands. As a test we have compared our derived zeropoints using the filter response of Bessell et al. (1998) and the Vega reference spectrum against those published in Bessell et al. (1998). For our photometric systems we integrate the summed number of photons counted by the simulated telescope systems, however to test the zeropoints and match the system of Bessell et al. (1998) we must integrate the summed energy. The zeropoints we derived (with the values of Bessell et al. 1998, in parenthesis) were: U =20.977(20.94), B =20.499(20.498), V =21.116(21.10), R =21.676(21.655), I =22.376(22.371), J =23.735(23.755), H =24.989(24.860), K =25.884(26.006) and L =27.809(27.875). Our derived zeropoints and those of Bessell et al. (1998) match to within 0.05 mags (and usually much closer) for all bands except the H,K and L bands. This is probably due to the previously noted IR excess (although detected at longer wavelengths) of the observed Vega spectrum. Bessell et al. (1998) use a combined model spectrum of Vega and Sirius as their reference spectrum. As a further test we also used the synthetic A0V stellar spectrum of Cohen et al. (1993) to derive zeropoints but were still unable to improve the match to the Bessell et al. (1998) photometric system for the JHK colours. However, for these colours we have adopted the CIT system, but were unable to find published zeropoints, and therefore used the Vega reference spectrum. Essentially this may mean there is a small offset in our JHK photometry, however as most of our results are based on differential photometry this will not affect our conclusions.

A further complication with our adopted photometric systems is the range of zeropoints available for the *Spitzer* IRAC photometry. For this study, as stated, we have adopted zeropoints calculated using the zero magnitude flux from the IRAC handbook [8]. The resulting zeropoints

were: Channel 1[3.6]=19.541, channel 2[4.5]=19.089, channel 3[5.8]=17.395 and channel 4[8.0]=17.966. The corresponding zeropoints derived for the MIPS passbands where: channel 1[24]=2.139, channel 2[70]=-0.2726 and channel 3[160]=-1.990.

In summary, several careful consistency checks were performed to confirm that the resulting SEDs and photometric magnitudes behaved as expected and matched any available published results. A failure to match the published zeropoints in the near-IR bands of the Bessell et al. (1998) using a Vega reference spectrum was probably due to an IR excess in our observed Vega spectrum. However as in general most of the conclusions or implications of this study are based on differential photometry, this should not affect them adversely. Furthermore, a failure to match the published magnitudes (and colours) for the atmospheric models in Chabrier et al. (2000), even using published zeropoints for the excellently defined system of Bessell et al. (1998), and subsequent conversions to the required CIT system (Leggett 1992), was prescribed to an update in the model atmospheres available online.

APPENDIX B: WEBSITE

THIS SECTION NEEDS TO BE SORTED

As stated throughout this paper the data presented are available from a web page [9]. In this Appendix we briefly discuss the data included, and the different ways of accessing or visualising these data on the website.

B1   Available Data

The magnitudes and colours presented in this paper are avaiable both as individual magnitudes and as isochrones or mass tracks. Photometric magnitudes have also been derived for several other systems and are available online. These are Johnson, Cousins *UBVRI(JHK)* (Johnson 1966; Bessell 2005), *Tycho* V_t and B_t (Bessell 2000), Bessell *UBVRIJHKL* (Bessell & Brett 1988; Bessell et al. 1998), SDSS *UGRIZ* (Fukugita et al. 1996), 2MASS JHK_s (Cohen et al. 2003; Skrutskie et al. 2006), MKO *JHK* (Simons & Tokunaga 2002; Tokunaga et al. 2002), UKIRT *ZYJHK* (Hawarden et al. 2001), IRAS 12, 25, 60 and 100 μm (Neugebauer et al. 1984) and SCUBA *450WB* and *850WB* (Holland et al. 1999). For further information on these magnitudes, such as the filter responses used and the adopted zeropoints please refer to the website.

Monochromatic fluxes

In addition to the magnitudes derived for each of these bands monochromatic fluxes have also been derived for all bands listed above. These have been derived following closely the methods of Robitaille et al. (2006), extended to further passbands. For details of the assumed SED shape, central wavelengths and bandpasses adopted please refer to the website. The derivations of these monochromatic fluxes will be detailed in a coming paper, which details a fitting tool associated with these data.

---

[7] http://perso.ens-lyon.fr/france.allard/
[8] http://ssc.spitzer.caltech.edu/documents/som/som8.0.irac.pdf

[9] http://www.astro.ex.ac.uk/research/bd_disc

B2   Navigation

The main page contains links to download the entire dataset in several formats alongside files describing the format.

(i) All SEDs (Åand ergs s^{-1} cm^{-2}Å^{-1})

(ii) All SEDs (μm and mJy)

(iii) All Photometric Magnitudes for all BDD systems.

(iv) All Photometric Magnitudes for all Naked systems.

(v) All Monochromatic Fluxes for all Naked systems (μm and ergs s^{-1} cm^{-2}Å^{-1})

(vi) All Monochromatic Fluxes for all Naked systems (μm and mJy)

(vii) All Monochromatic Fluxes for all BDD systems (μm and ergs s^{-1} cm^{-2}Å^{-1})

(viii) All Monochromatic Fluxes for all BDD systems (μm and mJy)

Also included is a link to the calibration information listing all the filter response sources, adopted zero points, central wavelengths, bandwidths and assumed SED shapes (for monochromatic flux derivation). A brief scientific overview is also available explaining, in general terms, the dataset and model.

B3   Browsing Tools

For users who wish to investigate the dataset in a more specific or interactive fashion two browsing tools are included.

The isochrones, mass tracks and individual stars magnitudes and colours generated and presented in the work can be queried using the "Isochrone and Mass Track Tool". This allows the user to select the parameters of the model required and retrieve the specific data.

Secondly, an interactive tool is included allowing a user to select a given set of parameters and download the "SEDs, monochromatic fluxes or magnitudes". In addition this tool plots the SEDs for the Naked system or the three inclinations, in the case of BDD systems and allows users to select filters sets, whose monochromatic flux values will be overlaid on the displayed SEDs.